J/ψ Production in Au-Au Collisions at

$\sqrt{s_{NN}} = 200$ GeV

A Dissertation

Presented for the

Doctor of Philosophy Degree

The University of Tennessee, Knoxville

Robert Jason Newby

December 2003

Abstract

This thesis presents the first J/ψ production analysis of Au+Au reactions at forward rapidity at $\sqrt{s_{NN}} = 200$ GeV. In the second year of RHIC running, design energy was achieved in the collisions of both Au+Au ions and proton+proton reactions. The production of the J/ψ is measured by the PHENIX experiment in Au+Au collisions as well as in proton-proton collisions. The scientific goal is to investigate the nature of hot, dense nuclear matter capitalizing on the unique properties of the J/ψ as a probe of this matter. Recent experimental results by the NA50 collaboration at CERN strongly deviate from the conventional picture that successfully describes data at lower energies. The importance of such a measurement is demonstrated by the wide spectrum of theoretical explanations concerning the existing data. The merits of these models will be explored in a systematic and comprehensive study of the J/ψ and open charm in collisions of a variety of species and energy. A survey of the theoretical models is presented and the relevant open charm and J/ψ PHENIX measurements are compared.

Contents

x

List of Tables

List of Figures

xix

Chapter 1

Introduction

An important role of science has been to shape our ideas of the matter which makes up our universe and the forces that govern them. Over the past century our understanding of the fundamental constituents of matter has evolved as atoms were divided into electrons and nuclei, nuclei into protons and neutrons. In the 1950's as hyperons and pions were discovered and their particle production and decays demanded additional degrees of freedom, Quantum Chromodynamics (QCD) and the Standard Model were formulated in the early 1970's to explain decades of experimental data. The Standard Model has since endured as its predictions have been experimentally tested. Recent theoretical calculations have predicted that highly excited and dense hadronic matter will undergo a phase transition. This predicted new state of matter is called the Quark Gluon Plasma (QGP) [23].

1.1 High-Energy Nuclear Physics

The primary goal of high-energy nuclear physics is the confirmation and study of Quantum Chromodynamics (QCD) in a macroscopic system. Quarks are the elementary particles that make up all hadronic matter. These quarks are normally bound to other quarks in groups of two and three by the strong force in a hadronic particle. QCD predicts that at high energy densities a new type of matter will be created. As hadrons are packed closer and closer together, the boundary of one hadron overlaps with another and the constituent quarks are no longer bound to the other quarks of the original hadron. This quark gluon plasma would have been present in the earliest stages of the formation of the universe and may exist at present in some stars. These are not conditions easily created in the laboratory. Nevertheless, high-energy heavy-ion collisions are currently being employed for this purpose primarily for their characteristic deposition of a large amount of energy in a very small volume. The energy density predicted to be required to form the QGP is 1-2 $\mathrm{GeV}/\mathrm{fm}^3$[24] and two existing experimental facilities have achieved these energy densities. The Super Proton Synchrotron (SPS) at CERN has achieved energy densities of 3.7 $\mathrm{GeV}/\mathrm{fm}^3$ and the Relativistic Heavy Ion Collider (RHIC) at Brookhaven National Lab has achieved energy densities of 7.6 $\mathrm{GeV}/\mathrm{fm}^3$.

1.2 Recent Experimental Results

The J/ψ is an extremely tightly bound state of a charm and anti-charm quark. The large binding energy has made it very useful as a probe of nuclear matter, and now it is considered one of the more promising probes of the quark gluon plasma. Until recently, the production of the

J/ψ in nuclear systems had been well understood within a single picture proposed by Gerschel and Hüfner in 1988 [25]. Prior experiments had indicated that J/ψ production did not scale with the number of nucleons in the target nucleus of proton-nucleus collisions nor the number of nucleon-nucleon collisions in nucleus-nucleus collisions as näively expected. Gerschel and Hüfner explained this with an effective absorption of the J/ψ onto the nucleus itself after its creation within the nucleus. By January of 2000 the NA50 collaboration at CERN had completed a systematic study of J/ψ production in Pb-Pb collisions at a beam energy of 158 GeV per nucleon extending the previous study of the NA38 for p+A, S+U reactions. In the collisions with the greatest energy densities, an "anomolous" suppression of J/ψ production was observed that did not follow the conventional picture[2]. In Figure 1.1 the ratio of measured J/ψ production to that expected from the conventional picture is plotted as a function of the energy density achieved in the collision. If the absorption of the J/ψ were only due to the "normal" nuclear absorption, the data would follow the dashed line. However, the data clearly deviate from this expectation at energy densities above 2.5 $\mathrm{GeV/fm}^3$. Furthermore, the onset of this deviation is relatively abrupt and the structure in the deviation is consistent with a multistage mechanism of this additional suppression. On February 10, 2000, CERN made a press release declaring that a new state of matter had been created in the SPS collisions. The J/ψ measurements were only a part of the evidence for this conclusion, but it is an essential piece and thus merits further consideration.
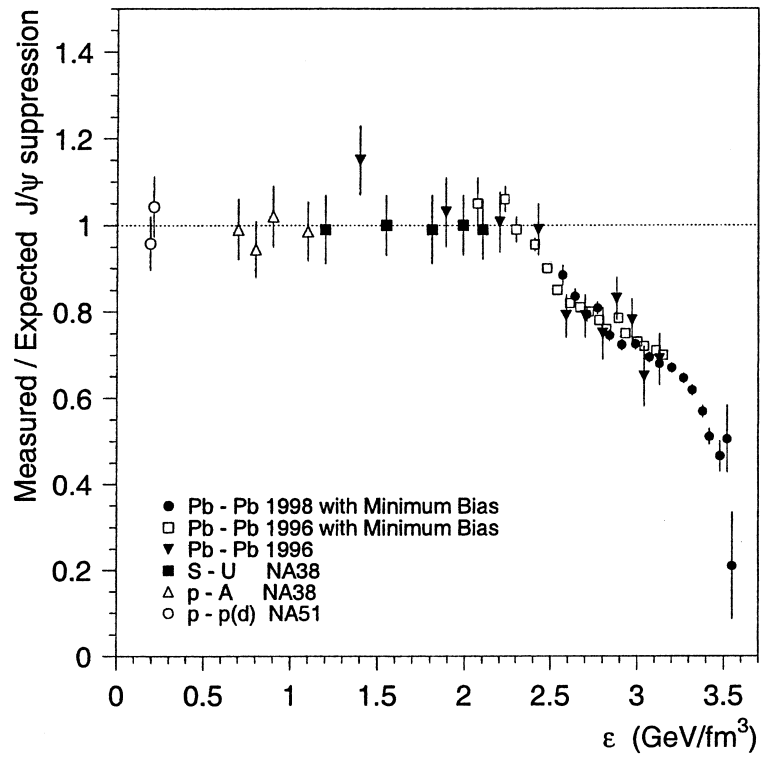
Figure 1.1: The ratio of measured J/ψ production to the conventional expectation as a function of the energy density produced in the collision is measured by the NA50 Experiment at CERN [2].

1.3 Motivations for this Measurement

The observation of the quark gluon plasma is an important verification of quantum chromo-dynamics and the standard model. The suppression of the J/ψ has been considered one of the more promising signatures of QGP formation and has often been advertised as a "smoking gun". The observations from NA50 provided somewhat less than a "smoking gun" and have given rise to very differing and controversial conclusions. The experimental methods and analytical techniques have been subjected to intense scrutiny to match the significance of the claim. The creation of a quark gluon plasm is certainly one conclusion that might explain the data. However, the quark-gluon plasma is not really well understood theoretically in ideal, infinite systems; application of theory to the in-homogeneous, finite-size nucleus-nucleus collision is even less rigorous. There are some components of the conventional non-QGP physics that are only marginally relevant at lower energies that could become important factors at RHIC such as nuclear shadowing and comover absorption. The impact of these non-QGP effects on J/ψ production must be assessed and given unbiased consideration. It is imperative that additional measurements be made to disentangle these many factors and provide independent confirmation of the NA50 results.

1.4 Organization of Thesis

The forward spectrometers of the PHENIX detector are designed to measure the J/ψ and ψ' among other vector mesons in p+p, p+A, and A+A collisions reaching center-of-mass energies of 500 GeV for protons and $\sqrt{s_{NN}} = 200$ GeV for nuclear systems. The PHENIX collabora-

tion has already published J/ψ measurements in proton-proton reactions for mid and forward rapidity and in Au+Au reactions for mid-rapidity [17][1]. An analysis of J/ψ production at forward rapidity in Au+Au reactions will be presented.

In Chapter 2, the theoretical and experimental landscape of J/ψ production will be presented. The unique properties of the J/ψ make it a useful probe, but there are many competing processes in both production and suppression of the J/ψ that must be evaluated. The significance of each must be assessed over the range of energy and systems for which data are available. In Chapter 3, an overview of the RHIC program and experiments will be provided. The PHENIX Forward Spectrometer and Vertex Detectors will be described in detail. In Chapter 4, the procedure for processing the raw detector data into a measurement of the J/ψ is provided including a description of the reconstruction and simulation software. In Chapter 5, the results of this analysis as well as the J/ψ and open-charm measurements of previous PHENIX publications will be discussed.

Chapter 2

Charmonium Production Overview

The hot, dense nuclear matter present in high-energy heavy-ion collisions provides a rich environment to study QCD and the standard model. The discovery of the J/ψ and its interpretation was an important step in the development of the Standard Model and has proved to be a valuable probe of the nucleon and the nucleus. It has been studied in great detail over a wide range of production conditions. We will review the history of the J/ψ relevant to the proposed use of its production as a QGP signature. While QGP formation is not proposed for proton-proton or even proton-nucleus collisions, it is critical that we understand the many factors of production in these systems.

2.1 Discovery

In November 1974 a resonance of mass 3.1 GeV/c^2 was observed simultaneously and independently in two different experiments at Brookhaven Nation Laboratory(BNL) [3] and Stanford

Linear Accelerator Center [4]. The AGS at Brookhaven accelerated protons to 28 GeV onto a beryllium target and measured e^+e^- pairs in two forward spectrometers. One strength of this experiment is in the search for new particles since all masses are simultaneously explored. The BNL data shown in the left panel of Figure 2.1 reveal a narrow resonance. A limitation of this experiment, however, was in precisely measuring the width of such a resonance. The e^+e^- collider, SPEAR, operating at SLAC was designed to search for new particles using a different method. The beam energy was precisely adjusted to match the mass of a hypothetical particle. A measurement of particle production was made; the beam energy was then incremented in 200 MeV steps. As long as the width of the particle was broader than 200 MeV, any particle within the explored energy range would have been observed. At these intervals, the very narrow resonance observed at the AGS could have easily been overlooked. Nevertheless, the new resonance was measured in hadronic, e^+e^-, and $\mu^+\mu^-$ decay channels revealing the same narrow resonance with a width less than 1.3 MeV/c^2. Both groups received credit for the discovery. The group from the West Coast dubbed the new particle the ψ and the East Coast group called it the J particle. Even at the time of the original publications it was suggested that this resonance might contain the previously predicted charm quark.

2.2 Theoretical Description

Since its discovery in 1974 the J/ψ and other charmonium states have been well understood theoretically. Charmonium is the bound state of a charm and anti-charm quark. For the purpose of this discussion it will be considered as a simple two body system. Since the relative velocities

8
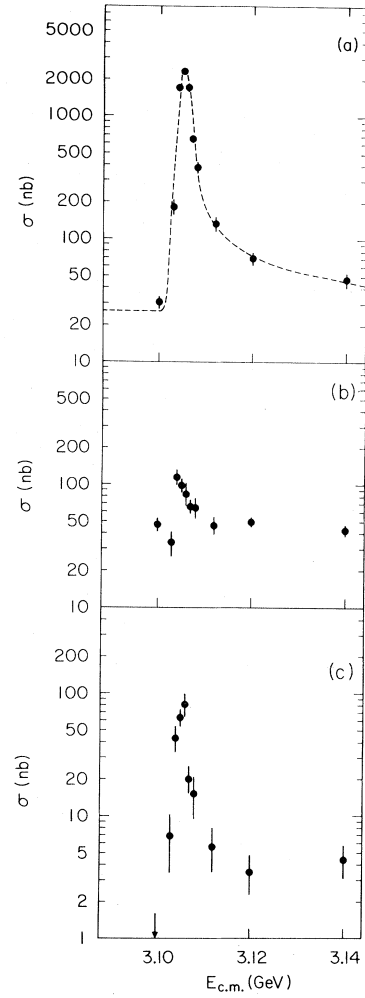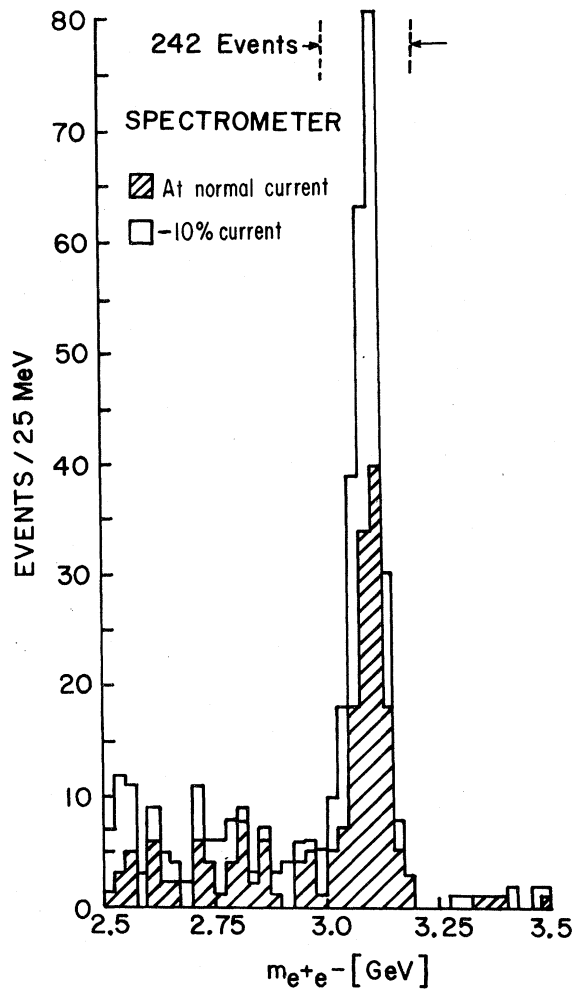
Figure 2.1: The first experimental observations of the J/ψ were made independently by experiments at BNL (left)[3] and SLAC(right)[4].

are rather small $\beta \approx 0.5$ compared to systems of lighter quarks $\beta \approx 0.8$, the $c\bar{c}$ pair may be treated non-relativistically. The charm quark having a coulombic charge of 2/3 that of the electron and the anti-charm -2/3 that of electron are thus attracted by the electrostatic potential.

$$V_{Electric}(r) = -\frac{q^2}{4\pi r} \tag{2.1}$$

Since quarks also carry a color charge, the pair experiences an attractive force from the strong confining linear potential

$$V_{Color}(r) = \kappa r, \tag{2.2}$$

where κ is the string tension coefficient. The resulting Hamiltonian of combining these potentials is therefore

$$H = \frac{p^2}{2\mu} - \frac{q^2}{4\pi r} + \kappa r. \tag{2.3}$$

By solving a Schrödinger equation that incorporates this asymptotic behavior of QCD, the spectrum of states can be derived [5]. The relevant quantum numbers are then the same as that for positroniun, and spectroscopic notation for the various states is then $n^{2S-1}L_J^{PC}$. Since the charm quarks are fermions with spin $1/2$ they can have their spins anti-aligned to form the spin singlet state (S=0) or aligned to form a spin triplet (S=1). N is the principle quantum number associated with radial excitations. J is the total angular momentum $L + S_z$. Furthermore, the charmonium states are eigenstates of parity (P), $P = -(-1)^L$, and charge conjugation (C), $C = (-1)^{L+S}$. By 1981 a rich spectrum of charmonium states, $\eta_c(1^1S_0)$, $J/\psi(1^3S_1)$, $\chi_{c0}(2^3P_0)$,

10

$\chi_{c1}(2^3P_1)$, $\chi_{c2}(2^3P_2)$, and $\psi'(2_3S_1)$, had been observed primarily in e^+e^- experiments as shown in Figure 2.2.

A limitation of the previous exploration in e^+e^- colliders is that the annihilation can only readily form the charmonium states with the same quantum numbers as the photon, namely the J/ψ and $\psi'(2S)$. The study of other states was limited by the resolution of the detection equipment since they are produced mainly as radiative decays of the ψ'. Intense antiproton beams with a small momentum spread were made available with the development of stochastic cooling; charmonium could then be studied in hadronic production [26]. The precise knowledge of the beam energy effectively allows the measurement of the initial state energy rather than reconstruction of the energy of the final state. The first such study was made at the CERN ISR and later by the E760 Collaboration using the Fermilab Antiproton Accumulator. Systematic studies of decay branching ratios, and feed down contributions such as $\psi' \rightarrow J/\psi + \gamma$, are critical to the use of charmonium as a probe of nuclear matter.

2.3   Direct Production Mechanisms

The production of charmonium has been studied under a variety of conditions. Our primary interest here is that of the interaction of a nucleon constituent with another nucleon constituent. At RHIC energies the predominant charmonium production process is gluon fusion. Nevertheless, deep inelastic scattering (DIS) measurements have provided important insight into the process of charmonium production and valuable tests of competing models. There are currently three models used to describe J/ψ production, listed in historical order, the Color Evapora-

11

(a) $c\bar{c}$ Spectroscopy   (b)   W(GeV)

5S

4S

4D

3S(+1001)   3P

3D

2S(+589)+589±6 ψ' (+704)+674±2 ψ''

91±5 η_c' 2P

+457±4 X_2
+411 ±4 X_1 } c.g.426(+419)
-316 ±5 X_0

1S   3097±2 J/ψ

111±5 η_c

^{3}S:1^{--} 2^{++} 3^{--}
       ^{3}P:1^{++} ^{3}D:2^{--}
^{1}S:0^{-+} ^{1}P:1^{+-} 0$^+$ ^{1}D:2^{-+} 1^{--}

4.41   4.5   4S

4.16   2D
      3S $\overline{F^*}F^*$
4.04   4.0 $\overline{F}F^*$
           $\overline{D^*}D^*$ $\overline{F}F$

ψ'' 1D $\overline{D}D^*$
ψ' 2S $\overline{D}D$
   3.5 $(c\bar{q},\bar{c}q)$

J/ψ 1S
   3.0 $c\bar{c}$
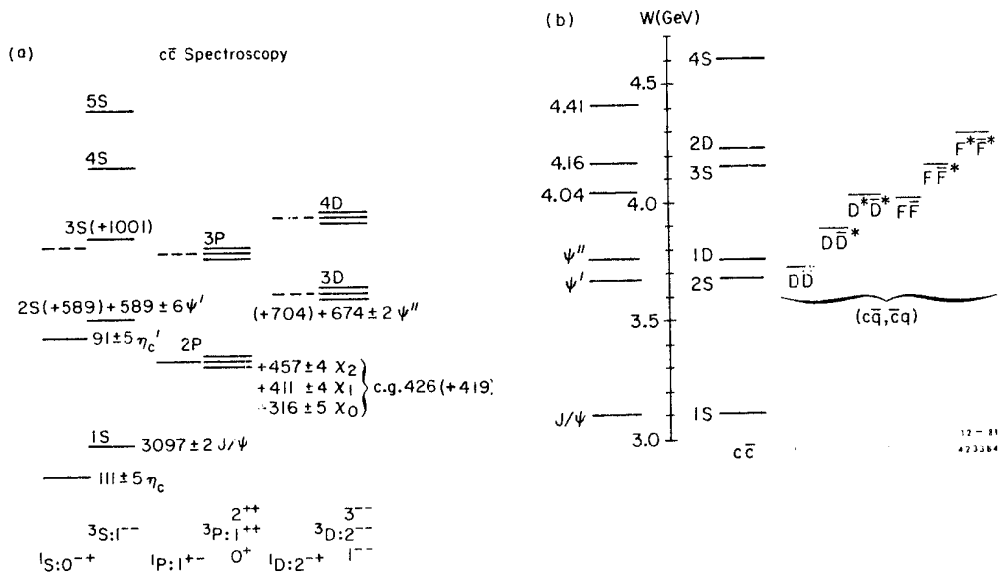
Figure 2.2: Charmonium spectrum with theoretical predictions of J. R. Richardson in parenthesis(left). The lowest lying charmed meson channels and the measured position of vector mesons(right). [5]

tion Model, the Color Singlet Model, and the Color Octet Model. Each of these models must address both the perturbative, short-range process of the quark anti-quark production, and the non-perturbative, long-range evolution of the pair into a physical state. All observed matter is color neutral. However, there are two possible classes of states in which an arbitrary $c\bar{c}$ might be initially formed, a color singlet or a color octet. The color singlet state is already color neutral. However, a color octet state has color that must be neutralized (by radiating a colored gluon) before it can be observed. Models that include formation of colored states must account for this required neutralization in the long-range evolution of the pair. Furthermore, each model must match measured absolute production cross-sections, production ratios of heavy quarkonium species (i.e. $\sigma_{\psi'}/\sigma_{J/\psi}$), production transverse momentum dependence, and the transverse momentum dependent polarization. The heavy-quark formation process occurs on distance scales of $1/m_Q$ while the transition to the physical quarkonia occurs on scales of $1/m_Q\nu$ where m_Q is the mass of the quark and ν is the relative velocity between the quark pair.

Common to all models is a required description of the partonic content of both hadronic projectiles and hadronic targets. At high energies, the valence quarks carry a small fraction of the total momentum; they primarily act as sources for gluons and other partonic degrees of freedom. The Parton Distribution Function (PDF) quantifies the probability of finding a parton carrying a fraction (x) of the total hadron momentum. The Feynman x ($x_F = p_z/p_{zmax}$) of a particle is an experimental observable given by the ratio of the longitudinal momentum to the maximum possible longitudinal momentum. By measuring the x_F of produced particles directly resulting from the initial hadron-hadron collisions, one can determine the parton dis-

tribution functions using the following relationship where x_1 and x_2 are the partonic fractional momentum of the target and projectile.

$$x_{1,2} = \frac{1}{2}(\pm x_F + \sqrt{x_F^2 + 4m^2/s}) \tag{2.4}$$

Systematic measurements of particle production from a variety of experiments are then used simultaneously in a single analysis to constrain these distributions as in [27].

2.3.1 Color Evaporation Model

The Color Evaporation Model (CEM) was developed in 1977 by Harold Fritzsch to apply QCD to charmonium production in hadronic collisions [28]. Early successes were achieved in applying the model to J/ψ production in $\pi^{+/-} + \mathrm{Cu}$ collisions measured by CERN-Omega [29].

The CEM allows both color singlet and color octet states to evolve non-perturbatively into a J/ψ [7]. Essentially, any $c\bar{c}$ pair with invariant mass between twice the charm mass and twice the D meson mass is considered independent of its spin and color state. The presumption is that any color can be later radiated by a soft-gluon in an interaction with the collision-induced color field. The charm and anti-charm quarks may then combine with lighter quarks to produce charmed mesons or the pair could evolve into one of the charmonium states. The production cross section of a charmonium state H is thus given by:

$$d\sigma^{CEM}(H + X) = f_H \int_{2m_c}^{2M_D} dM_{c\bar{c}} \frac{d\sigma(c\bar{c} + X)}{dM_{c\bar{c}}} \tag{2.5}$$

A phenomenological parameter, f_H, is used to designate the constant fraction of this mass-

region which evolves to a particular $c\bar{c}$ bound state [30]. Therefore, this model is unable to make any predictions about varied production of different $c\bar{c}$ states; the predicted production ratio's of different states are necessarily energy-independent. This is consistent with hadroproduction data at Fermilab [31]. The model is also consistent with the longitudinal momentum distribution over a range of energies and a variety of projectile-target systems although the normalization must be determined from the data itself. The model has no predictive power of the p_T distribution at low p_T; there is no way to separate the contributions of intrinsic transverse momentum of the initial partons and momentum fluctuations in the neutralizing color field. Furthermore, the same soft processes that "white-wash" the color from the color-octet state would also wash out any polarization. Therefore, the CEM predicts no polarization in the J/ψ production.

2.3.2 Color Singlet Model

In the color singlet model (CSM) the charmonium is formed as a non-relativistic bound state of charm and anti-charm [6] . This model assumes that the $q\bar{q}$ pair is initially produced in the color singlet state with appropriate spin (S) and orbital angular momentum quantum number (L) to evolve to a bound state $^{2S+1}L_J$ with total angular momentum quantum number (J). The color of the $c\bar{c}$ pair is removed via the radiation of a hard gluon as shown in Figure 2.3. The relative momentum of the $q\bar{q}$ pair inside the quarkonium is assumed to be small compared to the mass m_Q of the heavy quark so that the $q\bar{q}$ pair will not dissociate to form heavy mesons.

The CSM assumes that the color neutralization process of gluon emission occurs on the perturbative scale. This assumption is only valid if all of the momentum scales are sufficiently
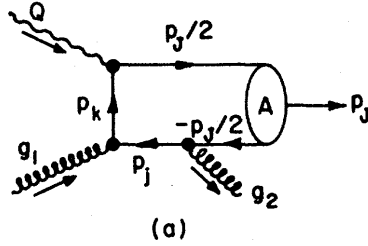
Figure 2.3: The color singlet process used in the Color Singlet Model [6].

large. However, for the J/ψ and ψ' to neutralize its color a gluon must be emitted. The model

is then limited to a low p_T of the J/ψ, so then the p_T-integrated yield includes a region of phase

space where this emitted gluon is "soft". While quarkonium production had traditionally been

calculated with this model at low collision energies; however, hadroproduction of charmonium

is not well described even at center-of-mass energies of 50 GeV [32]. Direct production of the

J/ψ relative to contributions from feed down from excited states is underpredicted by a factor

of 5 and the essentially unpolarized J/ψ and ψ' has not been reproduced.

2.3.3 Color Octet Model

The Color Octet Model (COM) utilizes an effective field theory, non-relativistic QCD (NRQCD)

developed by Caswell and Lepage in 1986 [33]. This model incorporates the contributions of

both color-singlet and color-octet production mechanisms. Some of those that are relevant for

hadroproduction are diagramed in Figure 2.4 along with the corresponding p_T scaling. Contrary

to its name, relativistic effects that are neglected in the CSM model are considered within the

COM by incorporating relativistic corrections.

16

(a) leading-order colour-singlet: $g + g \to c\bar{c}[^3S_1^{(1)}] + g$

J/ψ

g c

$\bar{c}$

g g

$+ \ldots$ $\sim \alpha_s^3 \dfrac{(2m_c)^4}{p_t^8}$
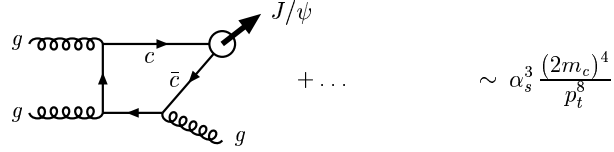
(b) colour-singlet fragmentation: $g + g \to [c\bar{c}[^3S_1^{(1)}] + gg] + g$

$+ \ldots$ $\sim \alpha_s^5 \dfrac{1}{p_t^4}$
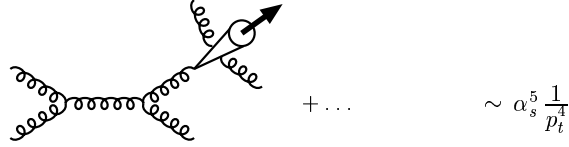
(c) colour-octet fragmentation: $g + g \to c\bar{c}[^3S_1^{(8)}] + g$

$+ \ldots$ $\sim \alpha_s^3 \dfrac{1}{p_t^4} v^4$
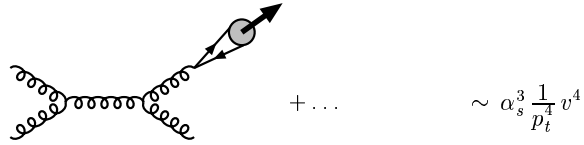
(d) colour-octet t-channel gluon exchange: $g + g \to c\bar{c}[^1S_0^{(8)}, {}^3P_J^{(8)}] + g$

$+ \ldots$ $\sim \alpha_s^3 \dfrac{(2m_c)^2}{p_t^6} v^4$
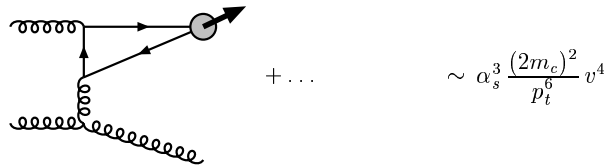
Figure 2.4: Production diagrams for J/ψ and ψ' and there corresponding p_T dependence [7].

In the NRQCD factorization there are several scales that relate to specific dynamics in mesons containing a heavy quark. The heavy-quark mass, m_Q, sets the overall scale of the rest energy. The typical relative momentum of the quarks $m_Q\nu$ determines the physical size of the meson where ν is the relative velocity of the heavy quark pair. The kinetic energy, $m_Q\nu^2$, sets the scale of the splittings of radial excitations and orbital angular momentum. Finally, the spin splittings are of the scale $m_q\nu^4$ [34]. The NRQCD factorization is valid as long as these scales are well separated. As the quark mass increases the relative velocity decreases. The typical relative velocity squared is about 0.3 for charmonium. Therefore the assumption that $(m_q\nu^2)^2 \ll (m_q\nu^2) \ll (m_q^2)$ is reasonably good for charmonium; this would not be valid for lighter quarks [18].

Figure 2.5 demonstrates the success of this model to reproduce direct J/ψ production at high p_T in $p\bar{p}$ collisions at the Tevatron. However, as noted by Nayak [18] the COM model at low transverse momentum is sensitive to the intrinsic motion of the initial parton inside the colliding nucleon. This results in the corruption of both color singlet and color octet production predictions. Therefore, J/ψ production calculations at RHIC energies are only calculated at $p_T > 2\,\mathrm{GeV}/c$.

2.4   Production and Suppression in Nuclear Targets

2.4.1   Normal Nuclear Absorption

Nuclear absorption of the J/ψ was first studied by C. Gerschel and J. Hüfner in 1988 [25] based on J/ψ measurements from the NA38 experiment. At that time J/ψ production had
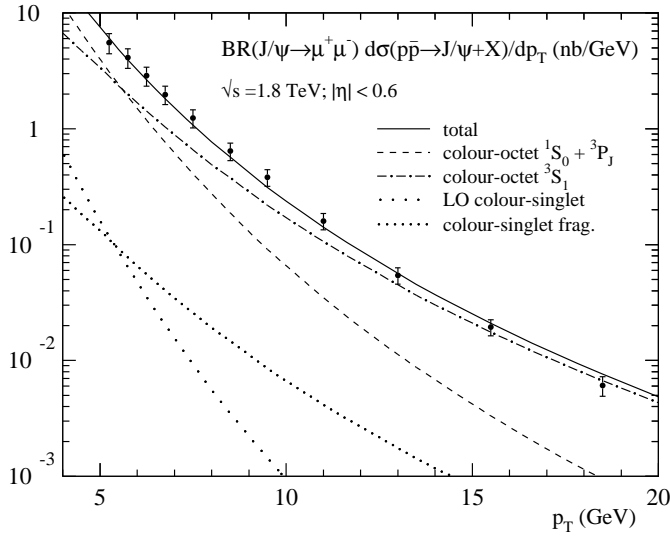
Figure 2.5: Color Octet Model contributions to J/ψ production at hight p_T [7].

been measured in a variety of projectile and target systems including projectiles of protons, antiprotons, pions, photons, and nuclei. However, a uniform quantitative comparison of these data were not in hand. In this publication they explored a common data analysis procedure. In the case of a nuclear target, any $c\bar{c}$ pair created by an initial collision that might later evolve into a J/ψ could be dissociated by an interaction with nuclear matter. The more nuclear matter that a charm pair must traverse for a given system the more likely the $c\bar{c}$ is to be dissociated. Gerschel and Hüfner calculated this mean path length, L, through the nuclei for the variety of systems. In their 1992 publication the production of J/ψ in p-A collisions was described by the following equation.

$$\sigma_{pA} = A\sigma_{pN}\exp[-\rho_0 \sigma_{abs}^{\psi N} L] \tag{2.6}$$

19

The cross section of production for $p + A \rightarrow J/\psi + X$ is σ_{pA} where A is the number of nucleons in the target nucleus, σ_{pN} is the J/ψ production cross section of a proton on an individual nucleon, ρ_0 is the nuclear density, and $\sigma_{abs}^{\psi N}$ is the absorption cross section of a J/ψ on a nucleon. The coefficient of the exponential characterizes the initial production while the exponential factor characterizes the dissociation of the charm pair.

In 1992 Gerschel and Hüfner demonstrated universal scaling of J/ψ cross sections with the variable L. Figure 2.6 demonstrates the success of this interpretation to describe the experimental data. The extracted cross section for a J/ψ to dissociate by colliding with a nucleon was $\sigma_{abs}^{\psi N} = 6.2 \pm 0.3mb$ [35]. This cross section was independent of projectile, p, $\bar{p}$, π, and γ and energy. For nucleus-nucleus collisions a consistent absorption cross section was found $\sigma_{abs}^{\psi N} = 5.8 \pm 1.8mb$. This did not agree with the J/ψ nucleon cross section extracted from photoproduction experiments[36], $\sigma_{abs}^{\psi N} = 3.5 \pm 0.8 \pm 0.5mb$.

Another convention for describing the scaling of particle production, such as J/ψ production, relative to the size of the target is the following expression, $\sigma_A = \sigma_N \times A^\alpha$. The cross section of the J/ψ production on a nucleon is σ_N and A is the number of nucleons in the target. By making measurements of σ_A for several values of A, α can be experimentally extracted. If the process scales precisely with the number of binary nucleon-nucleon collisions, $\alpha = 1$. Any enhancement over binary scaling will result in $\alpha > 1$, and $\alpha < 1$ indicates the process scales less than the number of binary collisions. The E866 Experiment has recently measured the A scaling in J/ψ and ψ' production over a range of x_F [9]. The data show in Figure 2.7 that at small x_F the ψ' has a smaller scaling than the J/ψ while at larger x_F they have very similar

20
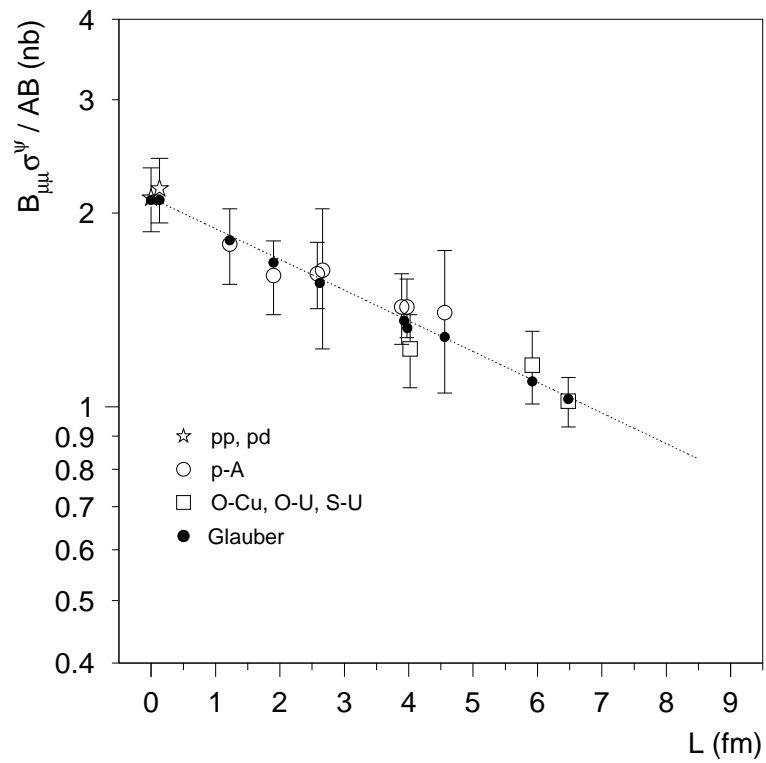
Figure 2.6: Normal nuclear absorption observed to scale with the mean path of the J/ψ out of the nuclear medium[8].
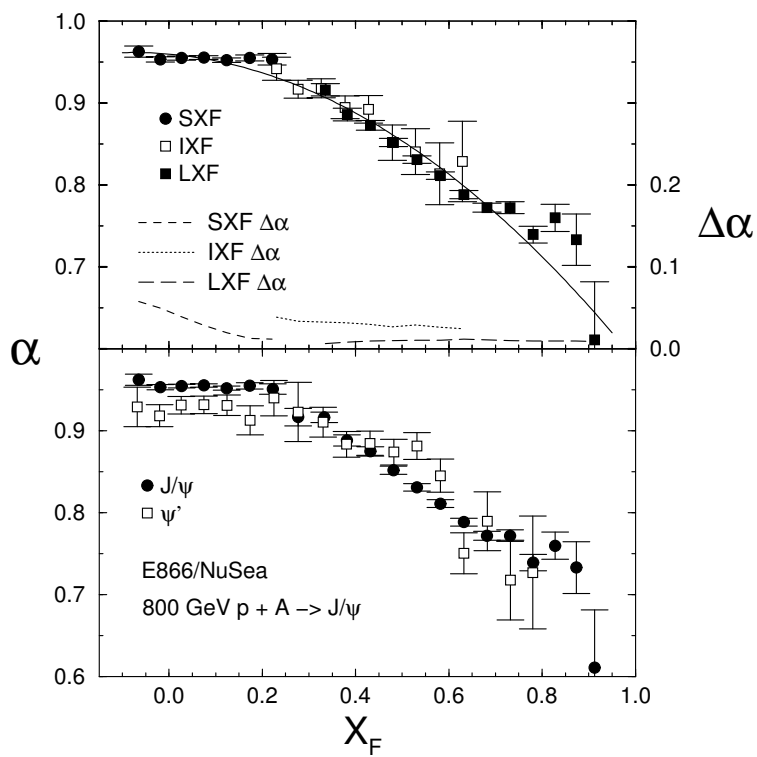
Figure 2.7: The x_F dependent scaling of J/ψ and ψ' production measured by the E866 experiment [9]

scaling. Two possible contributions to this behavior are initial energy loss and pre-resonant absorption. Firstly, inelastic collisions of the projectile on the target nucleon prior to the creation of any $c\bar{c}$ resonance would have the effect of shifting down the parton distributions to a lower fractional momentum suppressing the production at the most forward x_F. Secondly, the convergence of the ψ' and the J/ψ at high x_F may indicate absorption of a common pre-resonant state discussed later in section 2.4.3.1.

2.4.2 The Medium of Heavy-Ion Collisions

In a heavy-ion collision, a large amount of energy is deposited in a very small volume. At the Relativistic Heavy Ion Collider at Brookhaven National Lab, the collider accelerates gold nuclei to energies such that each nucleon has an energy of 100 GeV. Since there are 197 nucleons in a Au nucleus, the total energy is 19.7 TeV for the nucleus. For the collider, the lab frame is the same as the center-of-mass frame; a total of 39.5 TeV of energy is for a short time in a very small volume. For the proposed Large Hadron Collider at CERN there will be a center-of-mass energy of 3 TeV per nucleon, 1262 TeV in Pb+Pb collisions. The volume over which this energy is distributed is determined by the nuclear radius; the nuclear radius of gold is about 7 fm. However, the initial volume is much less than that of colliding spheres, since in the lab frame the highly relativistic nuclei experience a Lorentz contraction. How is this energy distributed? What are the particles that carry this energy? How do they interact with one another? We will now discuss dynamics of a heavy-ion collision from several plausible perspectives.

Since each nucleus is comprised of individual nucleons, we will first look at what happens

23

when two nucleons collide. The inelastic cross section of nucleon-nucleon collisions, σ_{NNin}, is a significant fraction of the total cross section, $\sigma_{NNtotal}$. If this were not the case, a nuclear collision would merely break up the nucleus and scatter the constituent protons and neutrons. In fact, the inelastic cross section is about 75% of the total cross section. In a nucleon-nucleon collision the net number of baryons is two. Since the net baryon number must be conserved, there must be two baryons in the final state. Typically, the collision results in each nucleon having lost about half its initial energy; this energy is primarily dissipated in the production of particles. The volume of the collision can be divided into two regions in the longitudinal direction. The kinematic variable, rapidity is given by $y = \tanh^{-1}(p_z/E)$ where p_z is the longitudinal momentum of a particle and E is the energy of the particle. This observable is convenient to study the longitudinal dependence of particle production. Since baryon number must be conserved and the colliding nucleons typically retain some fraction of their initial energy, there is a high probability that in the regions at the largest rapidity there will be particles that resemble the incident particles. These forward regions are called the fragmentation region; the particles that resemble the incident particles within the fragmentation region are called leading particles. The intermediate region is made up of the produced particles. The study of this intermediate region offers a unique opportunity to explore the properties of hot, dense hadronic matter macroscopically.

2.4.2.1 Hot, Dense Hadronic Gas

At RHIC energies the nuclei have passed through one another after only 0.1 fm/c or $3 \times 10 - 25$ s. In the wake of the collision are primarily pions which make up 80-90% of the produced

particles; they are the lightest of the mesons with a mass of $140\mathrm{MeV}/c^2$ and therefore most readily created. Also present, in what may be significant numbers, is the ρ meson. As the volume expands and the system cools, reactions among particles are no longer sufficiently energetic to alter the chemical content of the system resulting in chemical freeze-out. The population of various particle species at this point in the collision will largely determine the particle production ratios observed in the laboratory. As the expansion of the volume continues the density of particles is sufficiently small such that particles no longer collide elastically resulting in kinetic freeze-out. Assuming sufficient time for thermal equilibrium, the temperature at which the kinetic freeze-out occurs will be preserved in the p_T spectra of particles. Production of these particles at mid-rapidity scales primarily with the number of participant nucleons (rather than the number of nucleon-nucleon collisions) indicating that they are primarily produced through "soft", non-perturbative processes. There are several scenarios utilized to describe this medium: measured particle momenta and spectra indicate a thermalized medium and azimuthal anisotropy measurements suggest hydrodynamic flow.

2.4.2.2 The Quark Gluon Plasma

Another possible scenario may be relevant if the density of these particles in collisions at CERN and RHIC is great enough that it would no longer make sense to consider these as color-confined hadrons. In the standard model, the fundamental particles of the universe are leptons, quarks, and the bosons that mediate their interactions. There are six quarks arranged into three family of doublets, the down(d) and up(u), the strange(s) and charm(c), and the bottom(b) and top(t). These quarks carry electric charges that are fractions of the electron charge, the first of each

doublet -1/3 and the latter 2/3. In addition, each quark carries a color charge. The theory of the interactions of these color charges is quantum chromodynamics. It is a quantum field theory analogous to quantum electrodynamics (QED).

The nucleons of normal nuclear matter are comprised of three quarks of the first family, the proton (uud) and the neutron (udd). Thus QCD is also the theory that describes the strong interactions of the nucleus. Quarks are point-like and confined to one or more other quarks in a hadron by a binding potential which increases linearly with their distance of separation. Therefore, it would take an infinite amount of energy to separate a quark from its partner. A hadron consisting of a quark and its anti-quark is called a meson while a hadron of three quarks is called a baryon. Each quark carries baryon number of 1/3 so that a baryon has baryon number of 1 and a meson has baryon number of 0. While quarks are point-like, hadrons and specifically nucleons have an associated finite spacial extent over which the quarks are distributed. If nucleons were both elementary and incompressible, a high density limit of matter would exist when in a state of close packing. However, a composite nucleon will instead begin to overlap other nucleons as they are they are packed more densely. In this state, it no longer makes sense for a quark to be bound to the other constituents of the nucleon. This does not mean the quark can now be isolated nor individually detected, but rather the quark is no longer bound to the nucleon and now free to move about within the larger system. If that color-deconfined system is also in thermal equilibrium, a Quark Gluon Plasma is formed.

In a nuclear collision where energy densities may reach ten times that of normal nuclear matter, it is predicted that a QGP will be formed. Attempts have been made to study this matter

26

theoretically within QCD lattice calculations. These studies predict a critical temperature, a melting point for hadronic matter, of $T_C \approx 150 - 200\text{MeV}$ depending on model assumptions [24]. One of the most critical characteristics is the nature of the transition itself: Is the melting a first order transition? Can a mixed phase of color-confined and color-deconfined matter exist? For the most realistic case of two light quark flavors and one heavy flavor quark, the order of the transition depends on the specific estimates of the quark masses. With ambiguity of the calculation in this simplified system, rigorous application of QCD to the inhomogeneous un-equilibrated medium of very complex heavy-ion collision poses a challenge beyond the ability of current frameworks.

2.4.2.3 Melting Color-Glass Condensate

At the large energies of modern colliders the nuclei involved in collisions are highly relativistic and therefore a new paradigm has been introduced to consider the resulting modifications to the initial state [37]. The color charges within the hadron are propagating at nearly the speed of light and therefore the internal dynamics which are typical with in the hadron rest frame are frozen by Lorentz time dilation in the collision center-of-mass frame. Applications of perturbative QCD have been made to a variety of high-energy physics processes. In order for a QCD processes to be calculated perturbatively, the process must be hard; the momentum transfer must be larger than the QCD scale, $Q^2 \gg \Lambda^2_{QCD}$. In high-energy collisions the center of mass energy, $\sqrt{s}$, is very large such that the fraction of momentum carried by the relevant partons is $x \simeq Q^2/s \ll 1$. However, the QCD linear evolution equations predict such a rapid growth in the parton densities at low x that it violates unitary constraints. Furthermore, the low x gluons that have transverse

27

momentum below the non-perturbative validity region. This represents the "small-x" problem of QCD. At low x the probability that a gluon of the hadron will interact with another gluon of the same hadron becomes relevant. This is neglected in the standard BFKL evolution equation, and the momentum at which this becomes relevant is called the saturation momentum.

With sufficiently large nuclei or sufficiently high energy, the saturation momentum is large enough to be above the hard scale and perturbative QCD is applicable. The paradigm used to describe this system is the Colored Glass Condensate (CGC).

- **Color** characterizes the partons which carry color charge.

- **Glass** makes the analogy to systems of frozen disorder.

- **Condensate** characterizes the large occupation numbers of gluon modes at the saturation momentum. In fact, they are at the maximum value allowed by repulsive gluon interactions, a Bose condensate.

The CGC then is an classical effective field theory which provides the initial conditions of the colliding nuclei. It is a relatively new model, but has already successfully described hadron yields in nucleus-nucleus collisions at RHIC. The initial conditions provided by this description will certainly affect the initial production of particles as described in section 5.2.1.

2.4.3 Charmonium Interaction with the Medium

An understanding of the production of J/ψ within nucleus-nucleus collisions at CERN and RHIC will require that we consider how charmonium interacts with the media previously described. We have previously looked at the dissociation of charmonium through interactions

with the nuclear matter, primordial nucleons of the original target. However, once these primordial nucleons pass they leave behind the expanding media of produced particles. We will now consider the effect of this medium on the life of a J/ψ .

2.4.3.1   Formation Time

Since the J/ψ is created in the initial hard collisions, not only will the matter in which the J/ψ finds itself change with time as the system evolves, but the J/ψ itself must evolve over some time into a physical state. If this time is significant relative to the time the J/ψ spends inside the medium then this must also be considered. Several different approaches have been made to calculate this effect.

The formation time can be estimated in a simple model. Assuming the $c\bar{c}$ originate at the same space point the virial theorem can be used to estimate the relative velocity of the quarks as they move away from each other. The time it takes the quarks to separate the distance characteristic to a particular charmonium state can then be calculated. The cross section of the charmonium on a nucleus is then proportional to its time dependent radial separation. This effect was first calculated by Farrar *et al.* [38].

The uncertainty principle offers another perspective on formation. When a $c\bar{c}$ pair is created it takes some time for it to realize which mass state it occupies. This time is related to the splitting of the mass states so that this formation time is $t_f = E_{J/\psi}/(M_{\psi'}^2 - M_{J/\psi}^2)$ [39]. The NA50 Experiment has measured $E_{J/\psi} \approx 50\mathrm{GeV}$. The derived formation time of $\sim 25\mathrm{fm}/c$ in the lab frame suggests the possible relevance of this effect. A more rigorous quantum mechanical calculation was performed by Kopeliovich *et al* [40]. The $c\bar{c}$ was treated as a harmonic oscillator

evolving in the medium. This result of this calculation predicted enhancement of the ψ' as the $c\bar{c}$ pair evolves within the nucleus.

The effect of this formation time might explain the scaling of the J/ψ and ψ' production observed the E866 experiment. At small x_F the $c\bar{c}$ fully hadronizes within the nuclear medium; therefore, there is a different absorption for the ψ' and the more tightly bound J/ψ. At large x_F the charmonium hadronizes outside the nuclear medium. Only the pre-resonant $c\bar{c}$ nucleon cross section is sampled along the path of the evolving charmonium.

2.4.3.2   Color Screening

In 1986 Matsui and Satz predicted that the color screening of a $c\bar{c}$ would be a signature of quark gluon plasma formation [41]. While others hinted at similar effects [42], this publication was the first quantitative study. They proposed that if a QGP is formed in a nucleus-nucleus collision, then any $c\bar{c}$ pair that would have normally evolved into bound charmonium would be color screened from one another. Instead of a final state of bound charm, the c and $\bar{c}$ would instead pair up with the more abundant lighter quarks to form charmed mesons at the hadronization.

In a QGP where other quarks and gluons are in close proximity to the $c\bar{c}$ pair, their color charge will screen one charm quark from"seeing" the anti-charm quark. This type of screening is called Debye screening analogous to the electric charge screening in Quantum Electrodynamics. Thus the potential of Equation 2.3 is modified in two ways within the QGP. The string tension κ is weakened with the increase in temperature. Normal matter is color confined when the string tension does not vanish. Matter is deconfined when there is some distance for which the string tension does vanish. The result is a Yukawa type potential of the form

$$V(r) = \frac{\alpha_{eff} e^{-r/\lambda_D}}{r} \tag{2.7}$$

where λ_D is the Debye screening length. The Debye screening length is determined by the temperature of the system. For a quark gluon plasma with three flavors of quarks evaluated from the lowest order perturbative QCD, the screening length is given by

$$\lambda_D = \sqrt{\frac{2}{3g^2}} \frac{1}{T} \tag{2.8}$$

If the screening length is less than the $c\bar{c}$ Bohr radius a given charmonium state by a ratio of 1.19 then no bound charmonium of that state can exist in the quark gluon plasma.

The J/ψ is an interesting probe then because it is very tightly bound and therefore its suppression by a QGP will be as dramatic as the onset of the QGP itself. The onset of the transition has been evaluated in a parton percolation model [10]. The medium of the collision is modeled as color flux tubes connecting the receding primordial nucleons subsequent to their passage through one another. In the transverse plane, these color flux tubes are then discs of some characteristic size. The overlap of such discs represents a communication of the tubes in the percolation sense as shown in Figure 2.8; a set of discs that overlap then form a cluster. When the density of these tubes is low, there is very little overlap and the average cluster size is small; when the density is very large there is one cluster that spans the entire system. The interesting aspect of percolation is that the progression between these two extremes is not gradual; the average cluster size instead exhibits a rapid increase at a critical density of clusters as shown in the
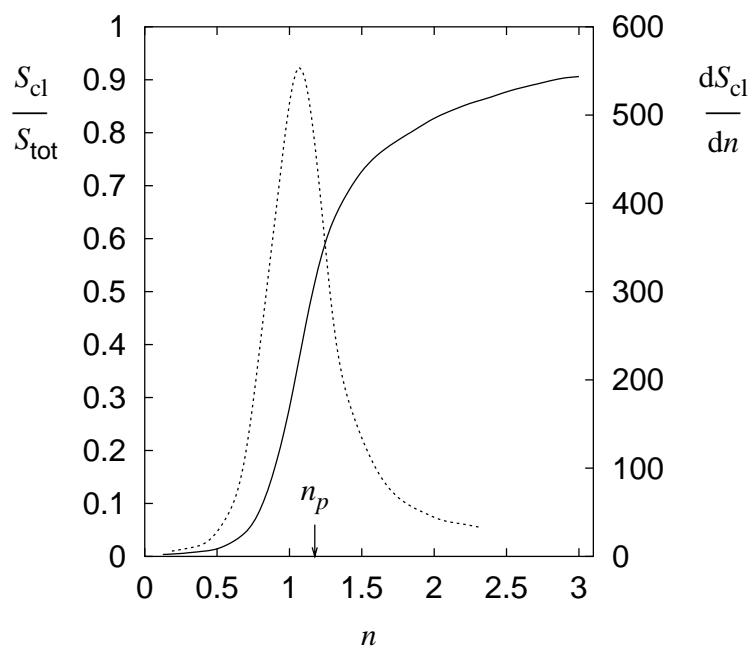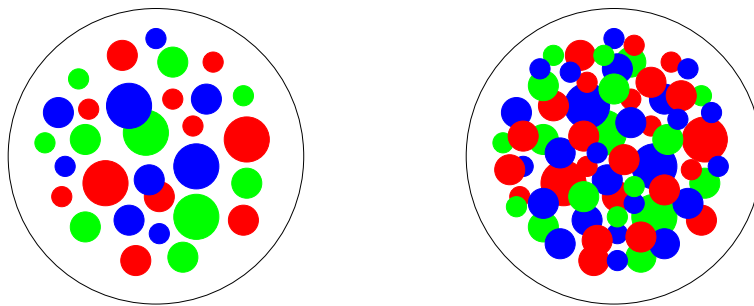
Figure 2.8: The overlap of colored clusters in low density (upper left) and in high density (upper right). The average cluster size (solid) and its derivative (dotted) as a function of the cluster density.[10]

lower panel of Figure 2.8. The implication then is if there truly is a phase transition to a QGP,

it should display this critical onset. Any probe sensitive to the transition like J/ψ suppression

should demonstrate this abrupt behavior.

This has driven one interpretation of the NA50 "anomalous" suppression data shown in

Figure 2.9. The first inflection in the data at an $E_T \approx 40 \text{GeV}$ may be associated with the onset

of the QGP and the melting of χ_c which would have transitioned to the J/ψ had it not been

dissolved in the QGP. These are dissolved as soon as the critical density for deconfinement is

reached. However, the J/ψ is more tightly bound and therefore does not dissociate until the

density is 60% larger; this may be interpreted as the source of the second inflection in the data.

2.4.3.3   Spontaneous Dissociation

Normally, the J/ψ is bound by the electric and color potential discussed earlier. However, lat-

tice QCD calculations demonstrate that the potential depends on the temperature of the medium

in which the $c\bar{c}$ finds itself [11].

$$V(r, T) = -\frac{4}{3} \frac{\alpha_s e^{-\mu(T)r}}{r} - \frac{b(T)}{\mu(T)} e^{-\mu(T)r} \qquad (2.9)$$

where $b(T)$ is the effective string tension and $\mu(T)$ is the effective color screening. This simi-

larly effects the other bound states of $c\bar{c}$. Thus, the binding energy of charmonium states is a

function of the temperature as shown in Figure 2.10.

As the temperature rises the charmonium states will eventually no longer be bound. Above

this temperature the $c\bar{c}$ could dissociate spontaneously as soon as an available transition sat-

33
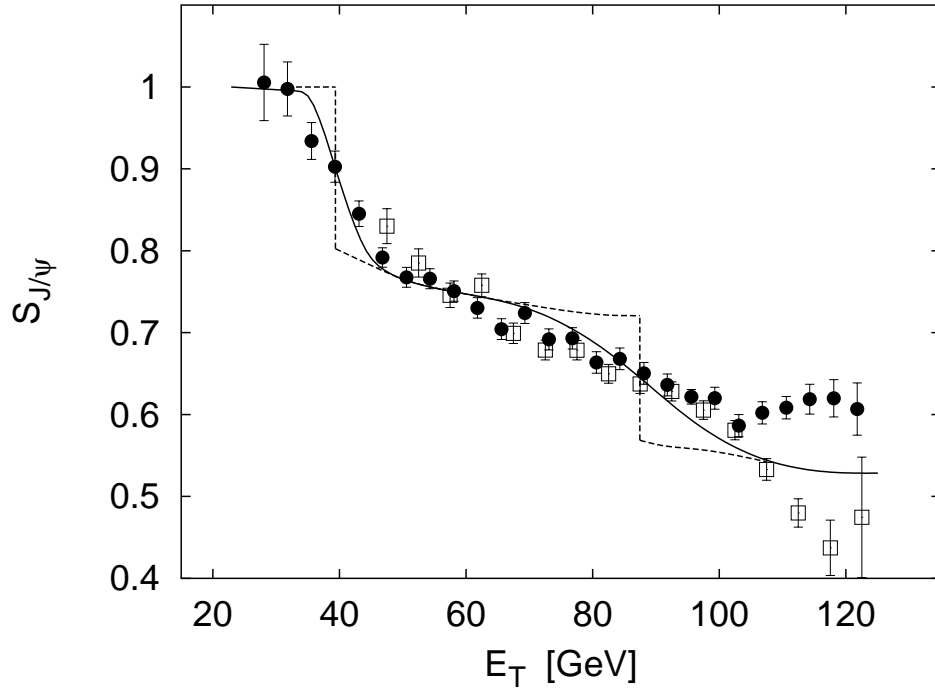
Figure 2.9: A percolation analysis of the J/ψ survivability in Pb+Pb collisions at SPS. The dashed-line is the likelihood the J/ψ will escape the collision medium as a function of the measured transverse energy indicating centrality of the collision. The solid line includes the fluctuations in the correlation of a transverse energy measurement with the nuclear impact parameter. The filled circles are the 1997 data and the open squares are the 1998 data taken from [10].
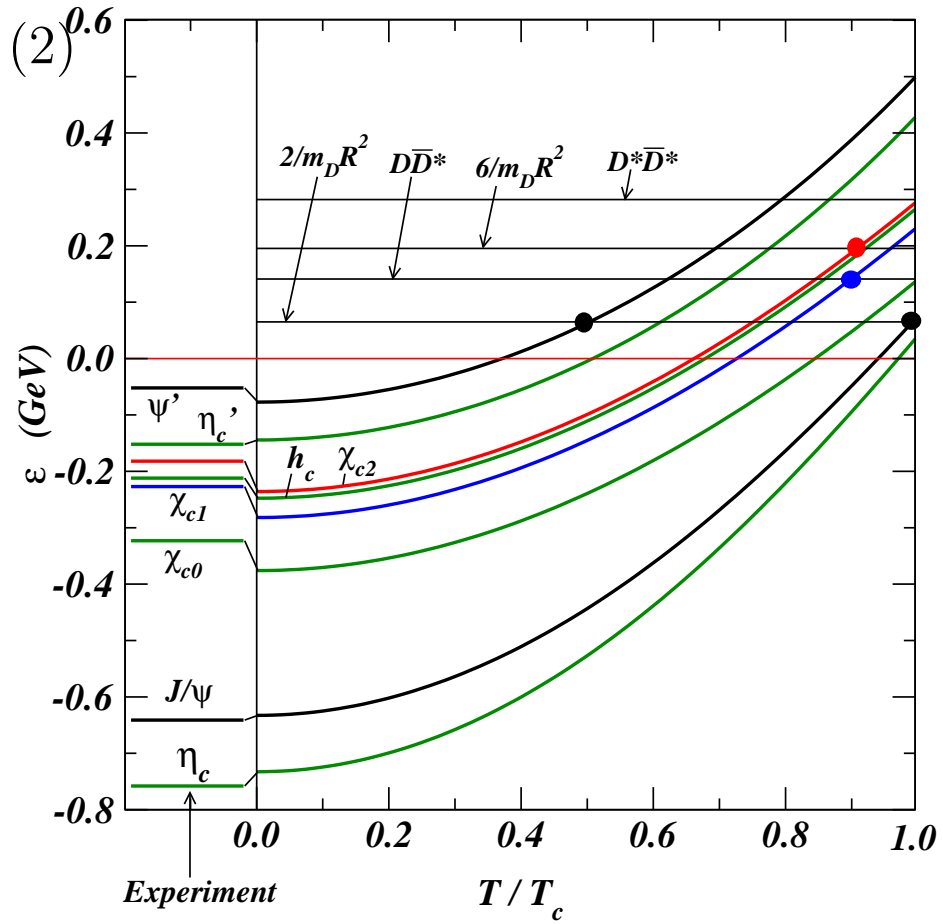
Figure 2.10: The binding energy of charmonium depends on the medium temperature[11].

isfies the selection rules for the decay. Note that all the charmonium states listed reach their corresponding temperature below the critical temperature of color deconfinement.

2.4.3.4 Thermalization

The charmonium produced in the initial hard scatterings are not in thermal equilibrium with the medium. As a charmonium state collides inelastically with the hadrons of the medium there is an excitation or de-excitation of the charm state. Once the charmonium in the system reaches thermal equilibrium, the occupation of the charmonium states should follow a Bose-Einstein distribution,

$$n_i = \frac{1}{\exp[(\epsilon_i - \mu)/T] - 1} \tag{2.10}$$

To illustrate the effect, consider a J/ψ produced in a system well below the temperature required for its spontaneous dissociation discussed in the previous section. Once the J/ψ thermalizes there is a probability that it will find itself in an excited state whose dissociation temperature is below the temperature of the system. This bound charm may then dissociate into a charmed meson pair. The determination of the importance of this process would require evaluating the decay rates of the various charmonium states as a function of temperature. This would then provide the decay rate of the charmonium in the system,

$$\frac{dn}{dt} = -\sum_i \lambda_i (2J_i + 1) n_i \mid_{\epsilon_i \geq \epsilon_{ith}} \tag{2.11}$$

where λ_i is the decay rate of the dissociating excited quarkonium state i. The effect of this

thermalization on the final J/ψ yield has been explored by Kharzeev, McLerran and Satz [43] and they found no significant contribution to the J/ψ absorption. However, this calculation assumed a temperature-independent charmonium binding energy in contradiction to the more recent calculation by Wong *et al.* [11]. While the latter calculation has not been carried through to a quantitative estimate of J/ψ yields, Figure 2.11 demonstrates the potential of this process to be an important component of suppression.

2.4.3.5 Hadronic Comover

While some of the collisions of the charmonium with the medium result in thermalization of the charmonium, some collisions with medium hadrons may be violent enough to break up the $c\bar{c}$. This source of J/ψ suppression was first suggested by S. Gavin *et al.*[44] and R. Vogt *et al.* [45]. One attractive feature of this explanation is the allowance of a smaller nuclear absorption cross section, σ_{abs}, since the measured σ_{abs} in photoproduction is roughly half that of hadroproduction. If comovers were really contributing to an effective σ_{abs}, this would bring the actual σ_{abs} into closer agreement with that of photoproduction.

The significance of this effect to the absorption of charmonium is driven by particle densities of the medium, the temperature of the medium, and dissociation cross sections. The first of these criteria is satisfied by pions since they comprise 80-90% of the produced particles. The dissociation cross sections may be calculated using the quark-exchange model of Barnes and Swanson [46] as shown in the upper panel of Figure 2.12. Assuming a Bose-Einstein distribution for the pions, the cross section can be estimated as a function of temperature shown in the lower panel of Figure 2.12.
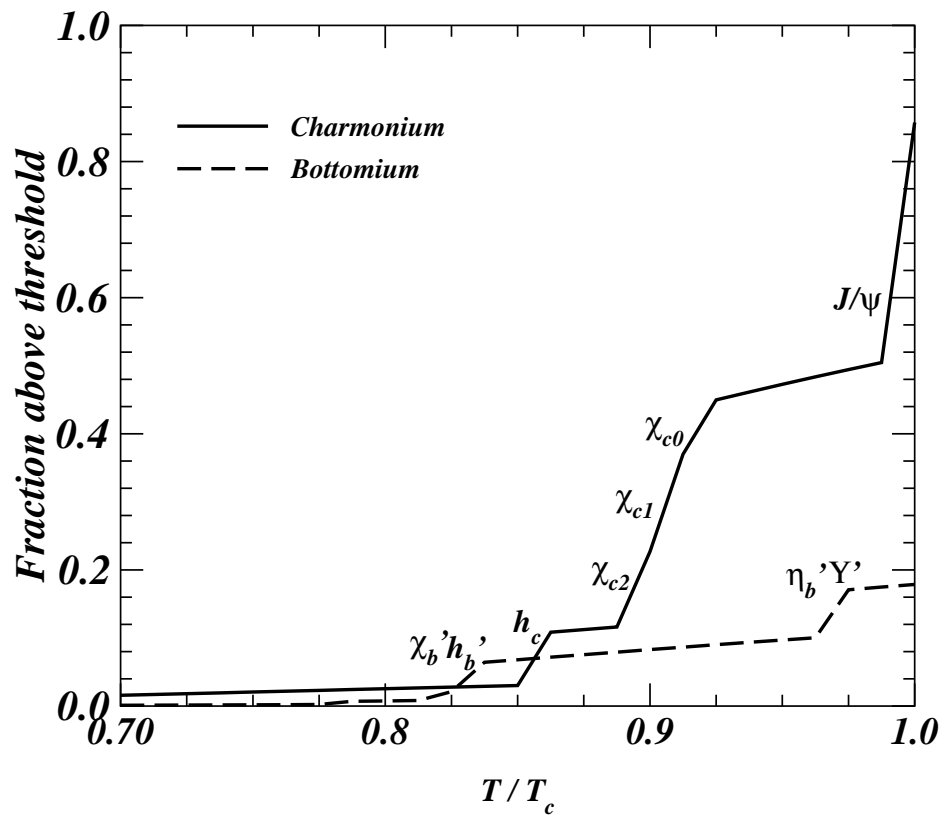
Figure 2.11: The fraction of total charmonium above corresponding dissociation temperature from [12].
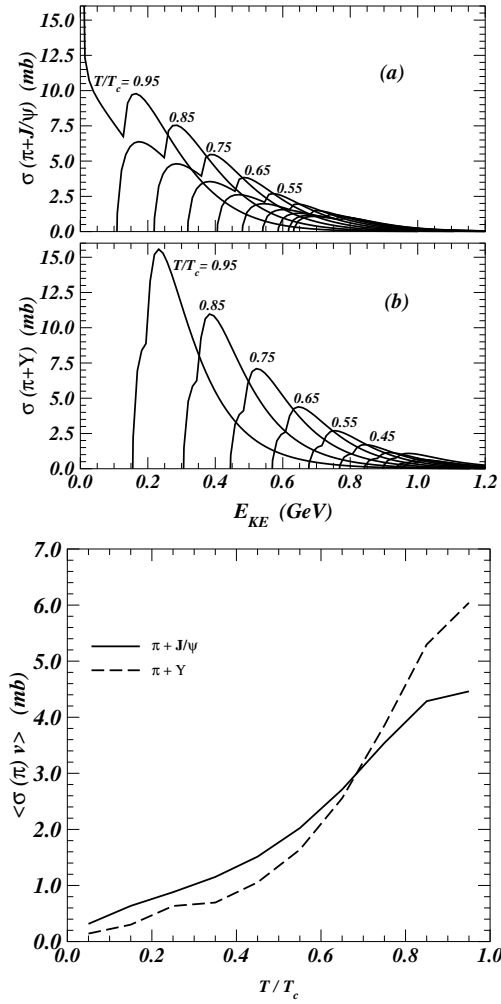
Figure 2.12: The dissociation cross section with a π as a function the kinetic energy [12]. The upper left panel shows this cross section for the J/ψ for several temperatures. The lower panel is the average π cross section as a function of temperatures for the J/ψ and Υ.

These cross sections may then be used to estimate the survival probability of the J/ψ. The medium is treated as a pion gas undergoing Bjorken type expansion with the initial conditions relevant for both CERN and RHIC. A survival probability of 0.34 is estimated for the most central Pb-Pb collision at $158A \cdot GeV$. For a central Au+Au collision at $\sqrt{s_{NN}} = 200\text{GeV}$ the survival probability is only 0.04.

Similar calculations have also been made using the meson-exchange model with similar results [47]. A quantitative comparison has been made of the CERN J/ψ production centrality dependence of NA38 and NA50 with a model including nuclear absorption and comover absorption [48]. The nuclear absorption is calculated utilizing the standard Glauber model nucleon distribution and assuming a constant J/ψ nucleon cross section. The density of comovers is determined from the Dual Parton Model [49] and a constant comover absoption of $1mb$ is used. Figure 2.13 demonstrates the good agreement of this model, solid line, and the CERN data except at the highest transverse energy. However, there is a possibility that the second inflection at high E_T is an artifact of the analysis.

2.4.3.6 Coalescence

The previous discussion of J/ψ production and suppression has been limited to that of directly produced charmonium. More recent models have predicted that at RHIC energies the increased total charm production will allow the binding of uncorrelated $c\bar{c}$ pairs. These models are motivated by the production estimates of 10 $c\bar{c}$ pairs at RHIC energies in a central Au+Au collision. Only a small fraction of these charm pairs would evolve into a J/ψ while most will dissociate. At lower energies if a $c\bar{c}$ pair is created, it is very unlikely that they would every find each other

40
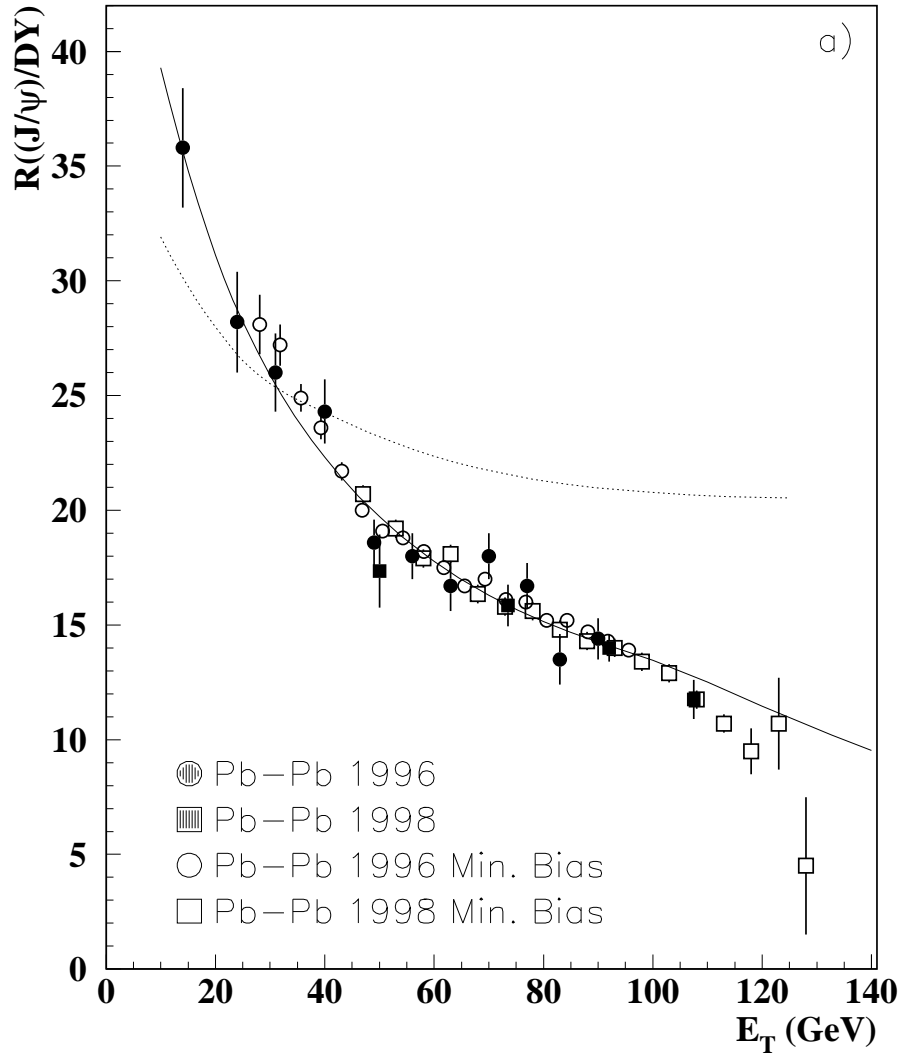
Figure 2.13: Comparison of the measured J/ψ - DY ratio of NA50 data to comover absorption model of Armesto et al. [48].

again to recombine as charmonium. However, at full RHIC energies it is possible that uncorrelated charm and anti-charm could combine to form charmonium. There have been four slightly varied approaches to exploring this component of production.

- Gazdzicki and Gorenstein[50] have demonstrated that purely statistical model of charmonium formation at QCD hadronization can account for the centrality dependence of J/ψ yields at full SPS energies. This model does not make any reference to the dynamic origin of the $c\bar{c}$.

- Braun-Munzinger and Stachel [51] use a statistical model assuming a fireball of $T = 160$ MeV and baryochemical potential of 266 MeV. Like the previous model, all charm is produced in the initial hard scattering and must be free to move within a deconfined QGP. Therefore, the charm component is not in chemical equilibrium with the medium. A charm-quark fugacity modifies the open and hidden charm thermal weights appropriate for the number of primordial $c\bar{c}$. This model thus requires an accurate assessment of total charm production and understanding of the system at the time of hadronization.

- The model Thews *et al.*[52] differs from previous models in that the dynamic evolution of the QGP fireball. The medium is assumed to be a ideal gas of free gluons and light quarks. In this model, the J/ψ is suppressed by interactions with the free thermal gluons. However, the reverse reaction is also possible. As the fireball evolves the rates of these competing processes are then integrated over the life of the QGP to determine the J/ψ yield.

- Grandchamp and Rapp[13] utilize a two-component model to combine direct production component and the model of Braun-Munzinger and Stachel for the statistical production. This allows the same model to be applied to SPS energies as well as RHIC and the relative importance of these contributions can be evaluated. This model will be further discussed below.

The model of Granchamp and Rapp has a strength in its applicability to CERN and RHIC energies. There are two sources of J/ψ production considered. First, the direct J/ψ's are produced by the primordial nucleon-nucleon collisions then subjected to dissociation in the QGP followed by the dissociation in the hadronic phase. Second, statistical recombination of independently produced c and $\bar{c}$ at the hadronization of the medium may form the J/ψ. Since they are not formed until hadronization, they are not subjected to dissociation in the QGP but may still be dissociated by comovers. Note that this model does not invoke any additional charm production in the QGP phase.

Within the QGP the primary dissociation mechanism is "quasifree" destruction arising from the in-medium modification to the chamonium binding energy. Within the hadronic phase the primary means of dissociation is due to inelastic collisions with π and ρ mesons since these are the most abundant in the hadron gas. These cross sections are produced using a SU(4) effective theory but in good agreement with the more rigorous quark-exchange model. These dissociation mechanisms can be evaluated over a range of temperatures within both media to determine a lifetime of both the J/ψ and its relevant feed-down states, ψ', χ_c as shown in Figure 2.14. The left panel shows the lifetimes within the QGP. At high temperatures all the

43
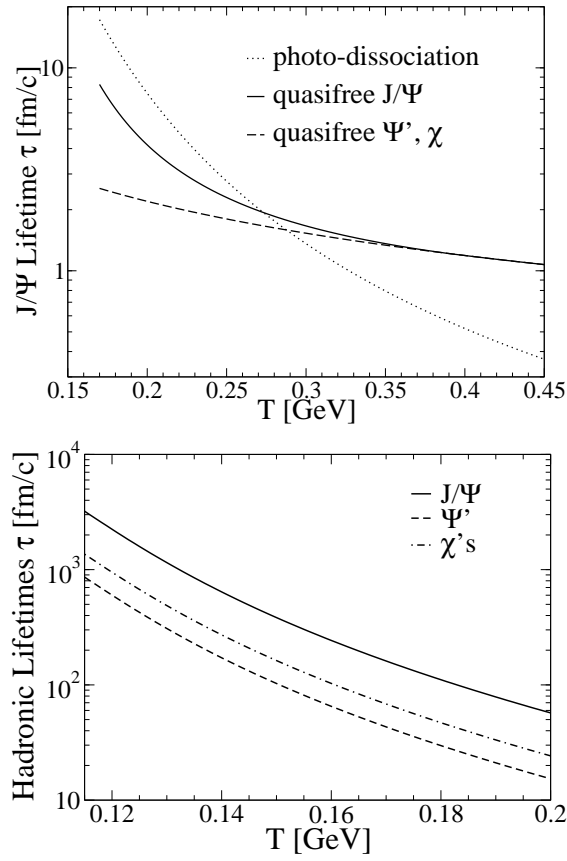
Figure 2.14: The lifetimes of the J/ψ and its relevant feed-down states within a QGP (upper) and a hadronic gas (lower) as function of temperature [13].

considered states have very similar lifetimes while at lower temperatures the more tightly bound J/ψ has a greater lifetime than the more weakly bound states.

Assuming a fixed initial J/ψ and open charm production rate, the J/ψ population can be evaluated as dissociation occurs within the cooling QGP, closed charm is recovered through hadronization, and dissociation occurs again in the expanding hadronic fireball. This time evolution is diagramed in Figure 2.15. A comparison of the model with the CERN NA50 data reveals a remarkably good agreement as demonstrated in Figure 2.16. In the left panel the first inflection in the data which is often attributed to the first melting of the J/ψ feed down states is in this model a result of the onset of the contribution of statistical production. At SPS only a small fraction of the observed J/ψ 's are created statistically.
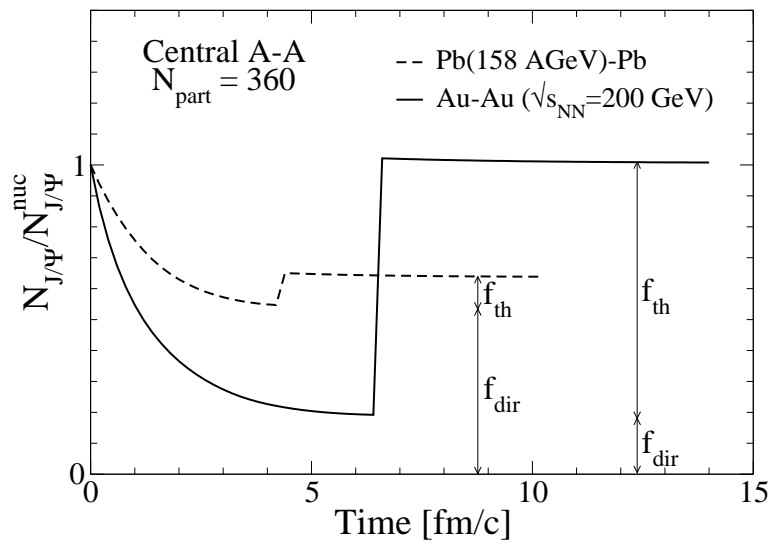
Figure 2.15: The time evolution of the J/ψ population using the two component production model of [13].
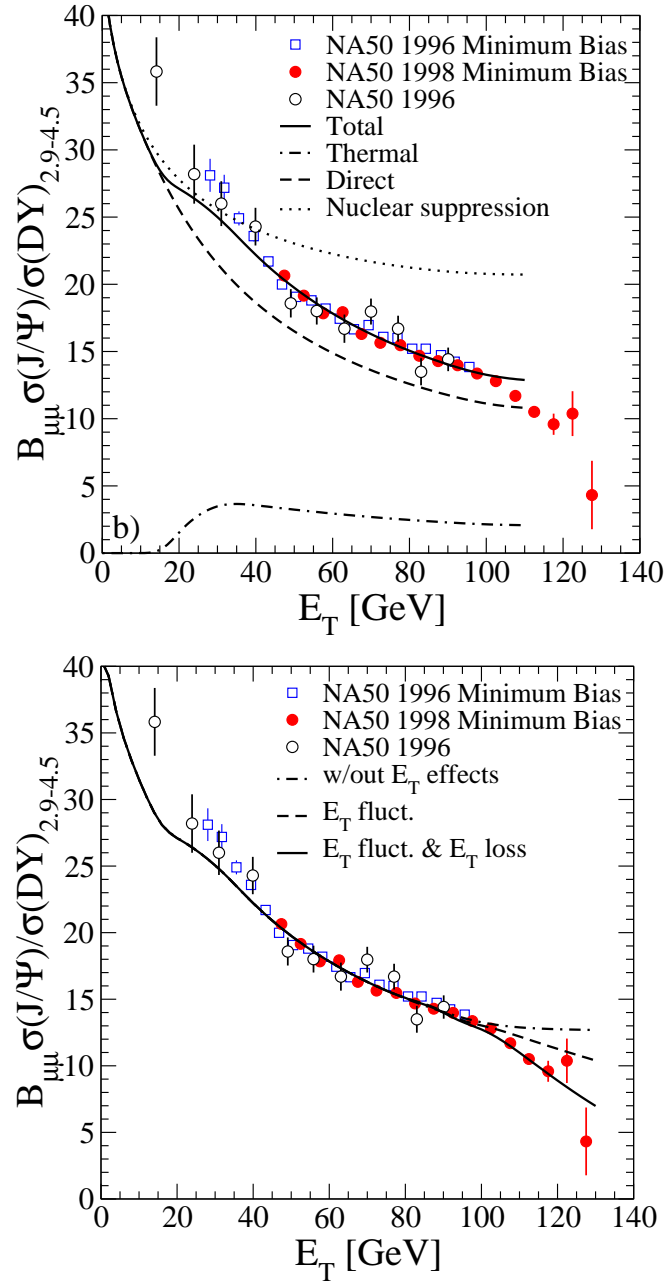
Figure 2.16: The CERN comparison with the two component production model of Grandchamp and Rapp without (upper) and with(lower) an accounting of the transverse energy fluctuations for the most central events[13].

Chapter 3

The Experiment

3.1 The Collider

The Relativistic Heavy Ion Collider (RHIC) at Brookhaven National Laboratory is a versatile machine able to accelerate a wide variety of nuclei up to 100 GeV per nucleon and protons up to 250 GeV. It is located at the Brookhaven National Lab in Upton, NY and builds upon the previous accelerator program of the Alternating Gradient Synchrotron (AGS). The design luminosity for Au beams is 200 $b^{-1}sec^{-1}$ and $20\mu b^{-1}s^{-1}$ for protons averaged over a 10 hour fill. Collisions occur at the six intersections of two independent accelerator rings in which ions are grouped into bunches to increase collision rates while minimizing the average current. Each ring contains 360 RF buckets separated in time by 106 ns. Ions are injected in bunches from the AGS into these buckets one at a time. A range of 6 to 56 bunches can be injected and provide collisions at each of the six interaction points simultaneously. To minimize intra-beam scattering the injection is performed in less than a minute. The acceleration from injection

energy to up to 100GeV/u is achieved within 2 minutes. At this time the bunches are transferred to the storage RF system which limits the bunch length growth to 30 cm rms. This parameter is important because it directly impacts the size of the collision diamond at the experiments and the the usable luminosity.

Figure 3.1 demonstrates the path of a Au ion through the accelerator complex, the Tandem - Van de Graaff, the Booster synchrotron, the AGS, and finally RHIC. The Au ions will begin their journey in the Tandem where negative Au ions are extracted from a pulsed sputter ion source and the ions with $Q_T = -1$ are accelerated through 14MV potential. After the negative ions pass through the stripping foil in the positive high voltage terminal with a positive charge Q_T. The positive ions are then accelerated back to the ground potential for a gain of $14Q_T$ MeV. The product of the Tandem is a beam of Au ions with a charge of +12 and 1 MeV/u kinetic energy. Upon exiting the Van de Graaff, the Au ions are further stripped to a charge of +32 before traversing the 850 meter long heavy ion transfer line to the Booster synchrotron. The Au beams are captured into six bunches and accelerated to 95 MeV/u before exiting the Booster where all but the two most tightly bound K-shell electrons are stripped. Almost half of all ions from the Tandem are successfully accelerated and stripped in the Booster. The +77 Au ions are filled in the AGS in four Booster cycles totaling 24 bunches. They are rebunched into four bunches before being accelerated to 8.86 GeV/u and exiting the AGS where they are fully stripped. The ions are transferred to the RHIC storage rings via the AtR beamline. There are five experiments at RHIC. Each experiment's position is tabulated in Table 3.1 and briefly described below:
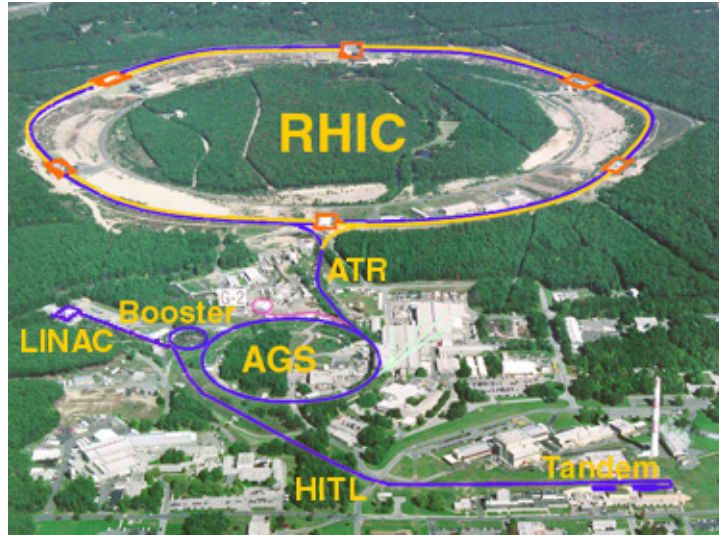
Figure 3.1: Arial view of the RHIC Complex.

Table 3.1: RHIC Experiments and their locations.

Interaction Point (clock position)	Experiment
12	-
2	pp2pp, BRAHMS
4	-
6	STAR
8	PHENIX
10	PHOBOS

- BRAHMS - The Broad Range Hadron Magnetic Spectrometer is capable of measuring inclusive momentum specta of identified charged hadrons over a wide range in rapidity and transverse momentum utilizing two magnetic spectrometers.

- pp2pp - This experiment measures total and elastic pp cross sections to provide an important comparison with existing $p\bar{p}$ data.

- STAR - The Solenoid Tracker at RHIC utilizes a Time Projection Chamber to track and identify a large fraction of the thousands of particles produced in a Au+Au collision at RHIC energies.

- PHENIX - The Pioneering High Energy Nuclear and Ion eXperiment utilizes a wide variety of detector technologies to detect hadrons, leptons, and photons in high multiplicity collisions and high event rates.

- PHOBOS - A large number of silicon detectors to measure charged particle multiplicity distributions in even the most central Au+Au collisions.

3.2 PHENIX Experiment

The PHENIX experiment is the largest of four experiments running during RHIC Run II. The collaboration has a wide variety of physics interests that are explored by the versatility of the RHIC machine. By utilizing RHIC's capabilities of colliding polarized protons the origin of the proton spin may be identified. Heavy-ions colliding at center of mass energies of 200 GeV per nucleon produce energy densities beyond the QCD confinement of hadronic matter. The

PHENIX detector combines many detector technologies as illustrated in Figure 3.2 to measure direct probes of the relevant physics interests such as electrons, muons, and photons. The experiment is separated mechanically into four large arms, three magnets, and inner detectors. Their acceptance is shown in Figure 3.3. Two large arms are located at mid-rapidity with a minimal intermediate material. The kinematics of photons and electrons are measured by tracking them in the field of the central magnet. The forward spectrometers are designed to measure muons. Unlike the central arm, the significant material of the central magnet is desired between the collision and the detector to absorb as much of the hadronic collision products as possible while allowing muons to sail through the material with a limited amount of energy loss and multiple scattering.

3.3   Inner Detectors

The PHENIX inner detectors are the Beam-Beam Counters (BBC) and the Zero Degree Calorimeters. Relevant to muon physics, they serve three major roles. First is the precise determination of the vertex. This is one of the major challenges of a collider experiment over a fixed-target experiment. In a fixed-target experiment the vertex distribution along the beam axis is essentially limited by the target thickness, while at RHIC the characteristic collision vertex distribution has a sigma of 25 cm. The second important role of these detectors is to determine the centrality (impact parameter) of heavy-ion collisions. Many of the physics goals of PHENIX depend on demonstrating trends in observables over a range of centralities. The independent determination of the centrality by two independent detectors using independent observables is an important
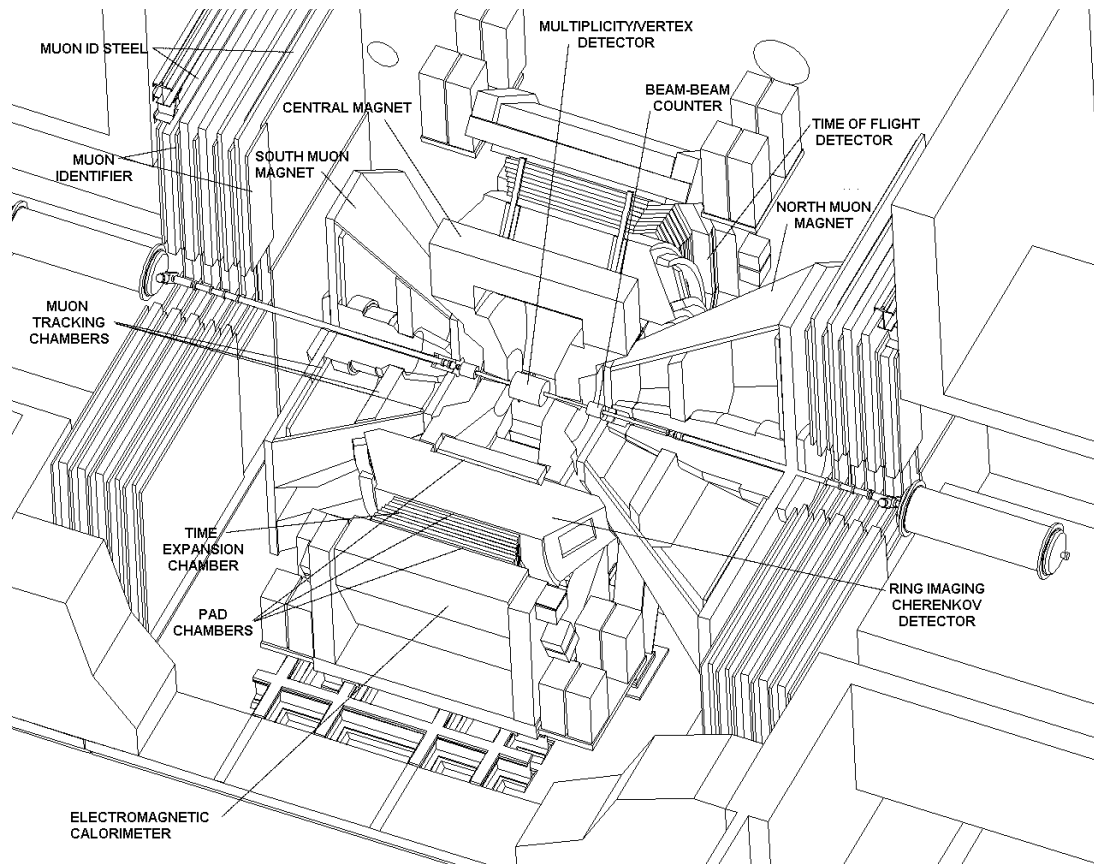
Figure 3.2: The PHENIX Detector is shown schematically. The nominal collision point is located within the region labeled MVD. The beam line then follows to the left and right. Centered along the beam-axis at the collision point is the PHENIX Central Arms Detectors and just up and downstream from the collision point are the pole tips of the Central Magnet.
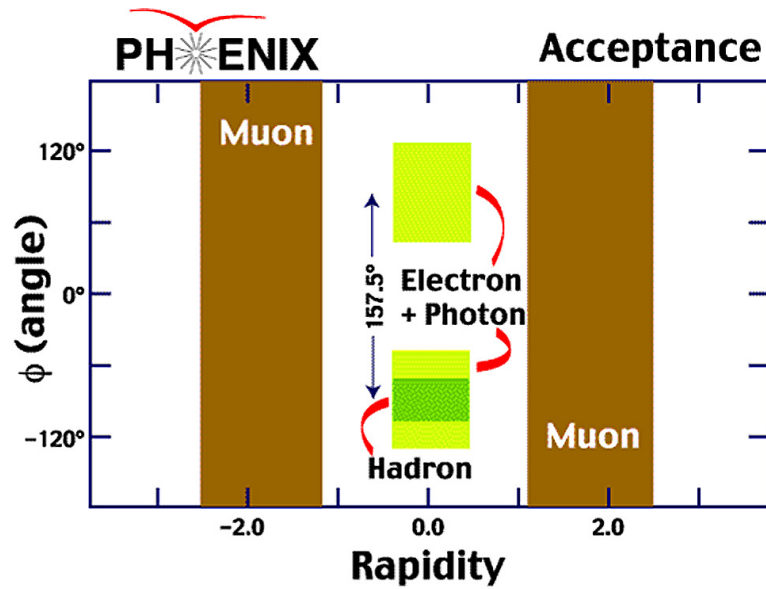
Figure 3.3: The Acceptance of the PHENIX Detector components in azimuth and rapidity.

cross-check on this critical parameter. Furthermore, one detector is able to complement the other in regions of phase space where they have differing levels of resolution as demonstrated in Figure 3.5. Lastly, while these detectors are sophisticated instruments, their readout is relatively simple and serve well as level 1 triggers.

3.3.1 Zero Degree Calorimeter

This detector is common to all RHIC experiments and provides a uniform baseline among all experiments as demonstrated in the vertex correlation with the PHENIX BBC shown in Figure 3.4. These forward detectors subtend an angle of 2.5 mr and are designed to measure beam energy neutrons that do not participate in the collision. Located about 19 meters from the collision vertex, the calorimeters are actually located between the diverging beam pipes of the blue
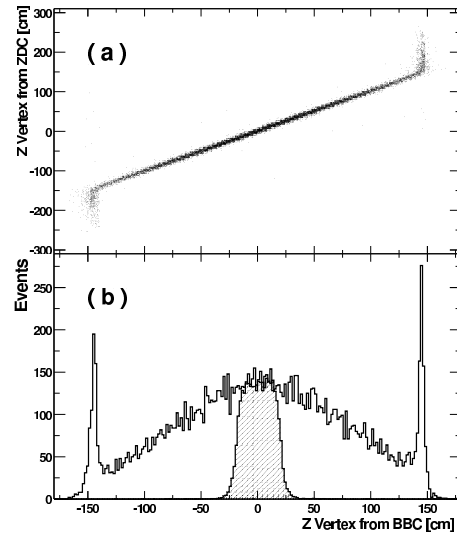
Figure 3.4: The BBC - ZDC vertex correlation is demonstrated in the upper panel. A typical BBC vertex distribution is shown in the lower panel [14].
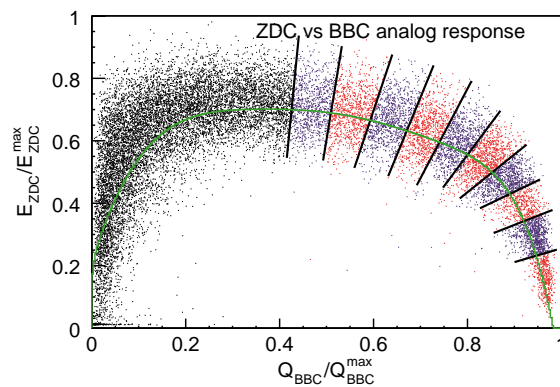
Figure 3.5: The BBC - ZDC Energy is correlated to define PHENIX centrality classes[14].

and yellow rings. This means that any fragment with a charge to mass ratio greater than 1/2 will be swept away from the ZDC by the RHIC DX magnets along with the beam itself. The neutral fragments however continue undeflected and deposit their energy in this forward detector.

3.3.2 Beam-Beam Detector

There are three essential functions of the Beam-Beam detector relevant to muon physics: level 1 triggering of vertex collisions, determining the vertex position along the beam axis, and measuring the collision centrality. The accurate determination of the vertex will directly affect both the J/ψ mass value and resolution. The technology employed for this role is a one-inch mesh dynode photo-multiplier tube mounted on a 3 cm quartz radiator. An array of 64 such channels are located on either side of the collision point along the beam axis. They cover the full azimuth at a pseudorapidity range of 3.0 to 3.9 in both directions and see 92% of the Au+Au cross section. Within the varied RHIC program the detector will experience a large range in charged-particle multiplicity requiring a dynamic range of 1 to 30 MIP's. The vertex position is determined by the timing difference of signals for the north and south beam-beam counters with a resolution of 50 ps. This corresponds to a vertex resolution along the beam axis of about 2 cm. This uncertainty in the vertex degrades the J/ψ mass resolution by about 13%.

3.4 Forward Spectrometers

The PHENIX Forward Spectrometers have been optimized to meet the relevant physics goals including measurements of vector meson production, the Drell-Yan process and heavy quark

production all through the muon decay channels. A combination of absorber and varied detector technologies shown in Figure 3.6 facilitate the tracking of muons in the forward regions while simultaneously filtering background resulting from hadronic sources. The amount and placement of absorber material was chosen to minimize the impact of multiple-scattering on momentum resolution of lower momentum muons associated with the ϕ as illustrated in Figure 3.7. Between Mutr Station I and the nominal collision point are 20 cm of brass and 60 cm of low-carbon steel [53]. This provides 4.9 nuclear interaction lengths to limit the hadronic background in the detector. However, the momentum resolution must be sufficient to separate the J/ψ and ψ'. These goals are achieved by combining the strengths of two very different detector technologies. The relatively finely segmented detector, the Muon Tracker (MuTr), can precisely reconstruct a particle's trajectory to the original collision point and provide a full kinematic description the precision of which is limited primarily by the multiple scattering within the absorber material. The very coarsely segmented detector, the Muon Identifier (MuID), lies behind even more absorber material and contributes little to the precision of the particle trajectory. However, the intervening absorber between the detectors and within the MuID itself provides increased hadron background rejection. Furthermore, the relatively small channel count and simplicity of the detector geometry allow the MuID to serve as a Level 1 trigger on a time scale much shorter that required to readout the MuTr. The design characteristics that enable these detectors to fulfill these complementary roles will be discussed in detail. During RHIC RunII only the south muon arm was instrumented and commissioned; therefore, the discussion will focus on the south arm.

58
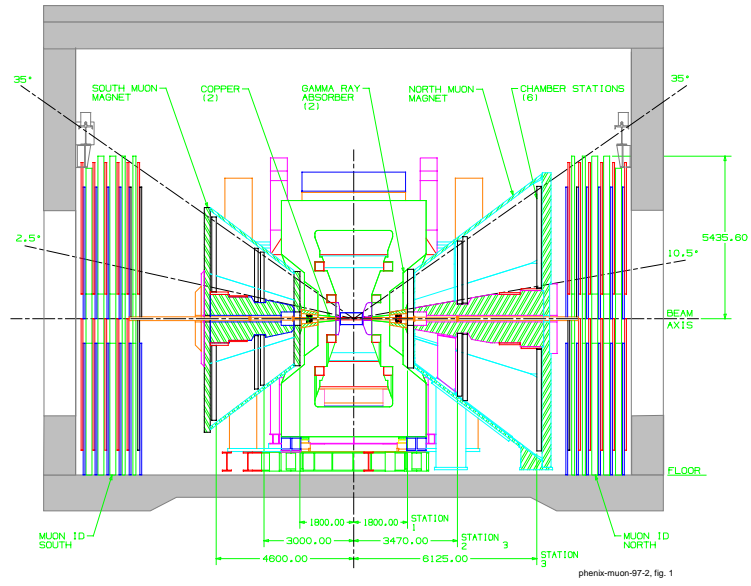
Figure 3.6: The PHENIX detector is diagramed from a side view.
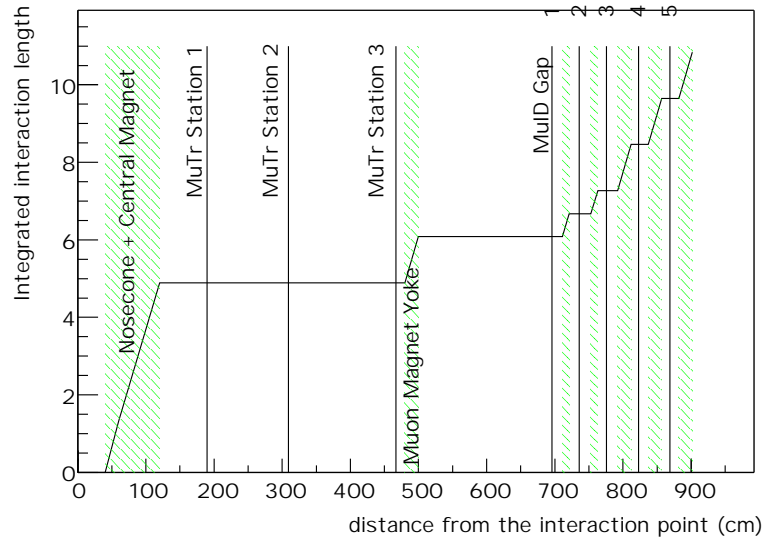
Figure 3.7: Integrated nuclear interaction length of the absorbers in the South Muon Arm[15].

3.4.1 Muon Tracker

The Muon Tracker is comprised of a radial field magnet as shown in Figure 3.8 with three stations of cathode strip chambers covering the full azimuth as diagrammed in Figure 3.9. As a particle from the collision point travels through the magnetic field, it is deflected in the azimuthal direction. There are three tracking stations that measure both the position and direction of the track. By comparing the position and direction of the three measurement points in a known magnetic field, the momentum of the particle can be determined as discussed later in Section 4.3.2.

The Muon south magnet utilizes two solenoidal coils to produce the necessary radial field to deflect charged particles originating from the collision point. The tapered piston around which the coils are wound is diagramed in Figure 3.8. The flux propagates through the piston and 20 cm thick backplane to be returned by the magnet lampshades. The magnet is shorter than its counterpart to the North because it is required to move out of the experiment hall to facilitate maintenance of the North Arm and Central Detectors. The Magnet has an minimum angle of acceptance of $12°$, slightly less acceptance than the North at $10°$, and a maximum angle of acceptance of $37°$. The average p_T kick in the magnet is about 200 MeV with a $\int B \cdot dl = 0.75 T \cdot m$ at a polar angle of $15°$.

There are three tracking stations in each of the muon arms. MuTr Station I South is located 189 cm from the nominal collision point. Station 1 is divided into four separate chambers (quadrants) and stations II and III are each divided into eight chambers (octants). Each tracking chamber is constructed as a conventional wire chamber. Cathode strips and anode wires are
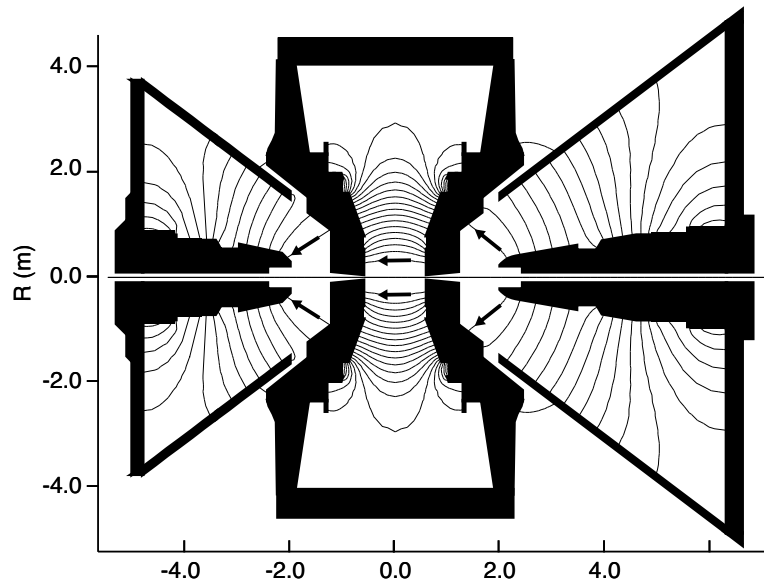
Figure 3.8: The PHENIX magnetic fields shown in the vertical plane along the beam axis.
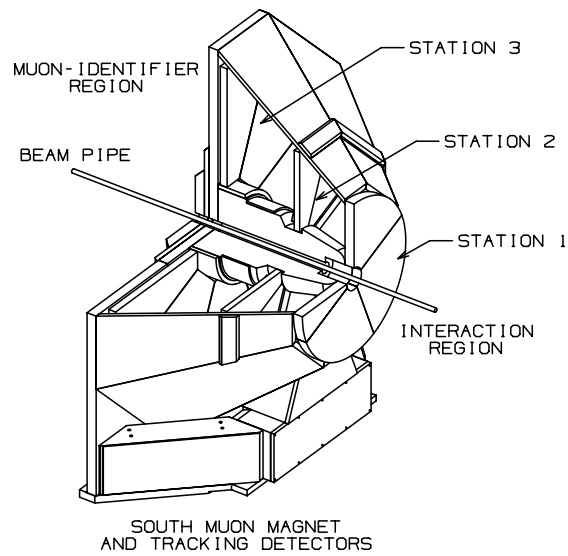
Figure 3.9: The Muon Tracker South has three stations. Station I has four chambers. Stations II and III each have eight chambers.

placed under high voltage in an ionizing gas. All tracking stations are constructed similarly, but station II has some differences to minimize multiple scattering in this critical mid-point measurement.

The muon tracking chambers at station I and II are each comprised of 3 gaps in which a layer of anode wires oriented azimuthally is sandwiched between two cathode planes as diagrammed in Figure 3.10. The anode wires are interleaved as sensing wires and field wires. The sense wires are $20\mu m$ gold-plated tungsten wires while the field wires are $75\mu m$ gold-plated Cu-Be wire with a spacing of 5mm. The cathodes strips are etched within a copper coating on a FR4 honeycomb panel. The cathode strip width is 1 cm and only every other strip is digitized. The 0.5 cm cathodes strips of one layer or oriented radially while the cathode strips of the stereo layer are oriented approximately 4-11 degrees relative to the radial strips of the same gap as shown in Table 3.2. The readout of one Station III gap was descoped due to budget concerns and since Station III benefits slightly from its proximity to the MuID.

The chambers of station II are constructed with slightly different materials such that the thickness is 8.5×10^{-4} radiation lengths. Instead of the honeycomb panel, a $25\mu m$ metalized mylar foil on which 5mm cathode strips are electro-mechanically etched.

As a particle enters the detector and ionizes the gas in the chamber, the charge is collected on the nearest anode wire. This induces a charge on cathodes layers on either side at the radial position of the anode wire (not necessarily the radial position of the particle's path). Each cathode strip is capacitively coupled with its neighboring strips. The distribution of this charge on the cathode strips is governed largely by the geometry of the conductors and is mathematically
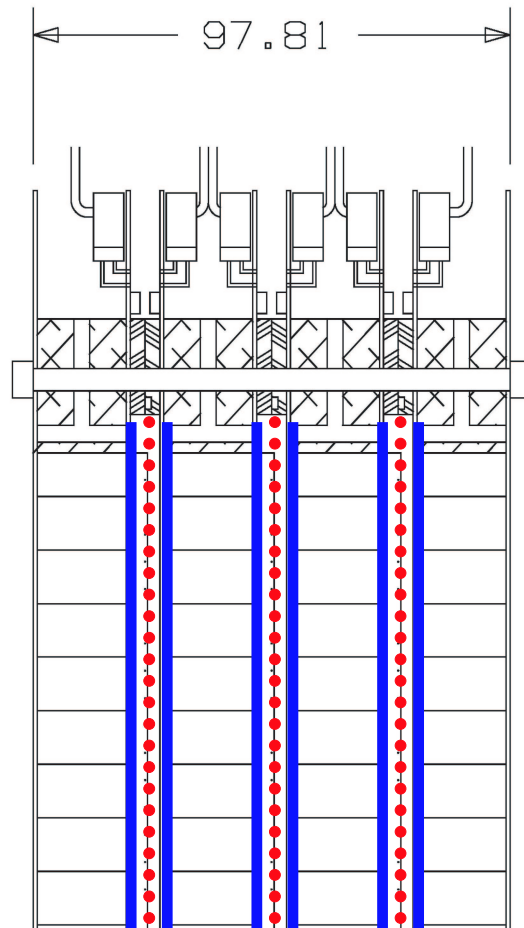
Figure 3.10: The three gaps of a Muon Tracking chambers is sketched. Stations I and III have similar chamber design.

Table 3.2: Each Gap of Muon Tracking Chambers contains one layer of cathodes strips oriented radially from the beam axis and one layer slightly rotated. The angle of rotation of the stereo plane relative to the radial plane is shown for the first half-octants of each station and gap where the plus sign represents the positive ϕ direction. The stereo layers of the second half-octants are a reflection across the half-octant boundary.

Station	Gap	angle (degrees)
	1	-11.25
1	2	+6
	3	+11.25
	1	+7.5
2	2	+3.75
	3	+11.25
3		-11.25
		-11.25

described by the Mathiason function. While all cathodes are capacitively coupled, only every other cathode is actually sampled and digitized, a design choice driven by the cost of the front-end electronics. The induction of the charge is most likely on three sampled strips as shown in Figure 3.11 with most of the charge residing on the central strip. By comparing the relative contribution of each strip to the total induced charge, the position of the particle's intersection with the detector can be determined far beyond the 0.5 cm detector segmentation.

3.4.2   Muon Identifier

3.4.2.1   Mechanical Design

The MuID is located just beyond the MuTr separated by the 30 cm thick steel backplane of the Muon magnet. The Muon Identifier is designed to efficiently detect muons while simultaneously filtering hadrons. This is achieved by layering absorbers and sensitive detectors as shown in figure 3.7. Further hadron rejection is gained by the detector's position forward of the Central
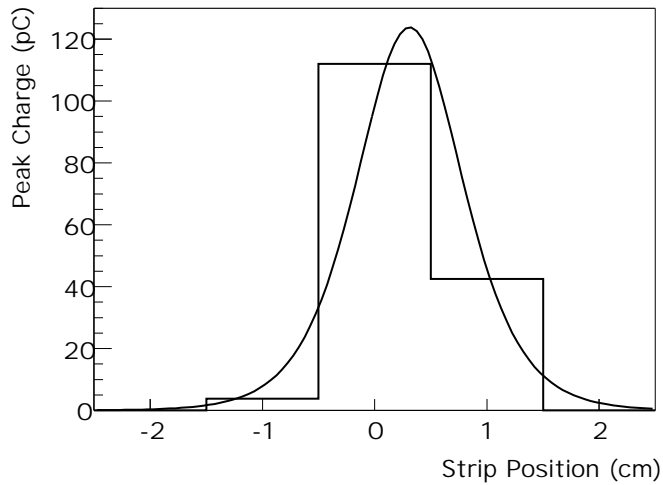
Figure 3.11: Induced charge distribution on the cathodes strips of one plane of the Muon Tracker.

Magnet and Muon Magnet yoke.

Each sensitive layer is comprised of six panels each positioned such that it overlaps slightly with adjacent panels as shown in Figure 3.12. This segmentation of the detector into these 6 panels reduces the stereoscopic ambiguities intrinsic to non-pixelated detectors with even limited occupancy. The Iarocci tube is mechanically the smallest detector unit and is diagrammed in Figure 3.13. Within each panel Iarocci tubes are organized into four layers. Two layers are oriented vertically and two layers are oriented horizontally. These two orientations are separated by an aluminum mid-plane that provides the mechanical support of the layers.

3.4.2.2 Front End Electronics

Within the MuID two-pack itself, the signals of the 16 wires that comprise a MuID two-pack are passively summed. The distance the raw signal must travel is minimized by positioning the
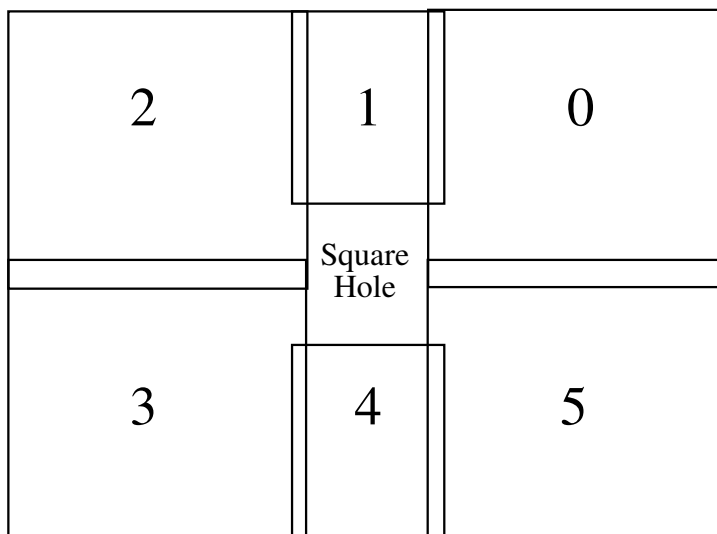
Figure 3.12: The arrangement of MuID panels is sketched. The south MuID panels are number counter-clockwise as seen from the interaction point. At the center is the MuID "square hole" which includes electrical and gas services to the small panels(1,4) and also passage of the the RHIC beam pipe. There are five such layers of panels separated by absorbing material.
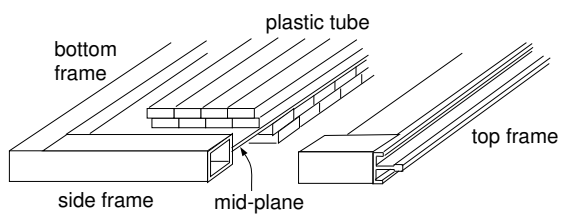
Cross section of the MuID panel
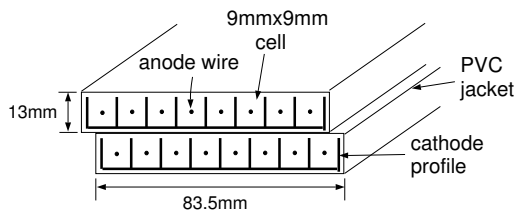
Cross section of the plastic tube(2-pack)

Figure 3.13: The MuID two-pack is comprised of two Iarocci tubes sandwiched together and slightly offset.

amplifiers as close to the electrical output of the two-packs as possible. These analog signals with travel up to 100 ft on twisted pair cables before being digitized. The amplifiers will provide two important functions to cope with this. Attenuation is addressed by amplifying the signal by a factor of 150 with the in-panel amplifier such that the minimum ionizing peak signal is about 40mV differential. Second, any common mode noise that might be introduced into the system is removed by duplicating the signal on both wires of a pair and inverting the signal of one copy. The signals of 16 adjacent channels are grouped together to be sent to the MuID electronics rack via a 34 conductor twisted pair cable.

The signals of one orientation for the entire arm are digitized inside one crate. Within a crate is one Front End Module (FEM) controller module and twenty read-out-cards (ROC). The FEM serves as a controller board for the crate and distributes the PHENIX beam-clock and controls to the ROCs. The ROC receives the amplified signals from the MuID panels and digitizes the data of 96 channels. The differential signal of each channel is amplified by a factor of three before it is split into three copies. A typical signal is shown in Figure 3.14. One copy is compared to a threshold value that can be set individually for each channel which provides an arming signal. The remaining two copies are used in a constant fraction discriminating (CFD) circuit which provides consistent timing of the signal independent of signal magnitude. A logical AND is formed from the threshold test and the CFD such that the timing of the signal is determined by the CFD.

The logical signals are then collected into one of six Digital Mux integrated circuits that will apply appropriate delays to each signal compensating for the varying cable lengths. Every
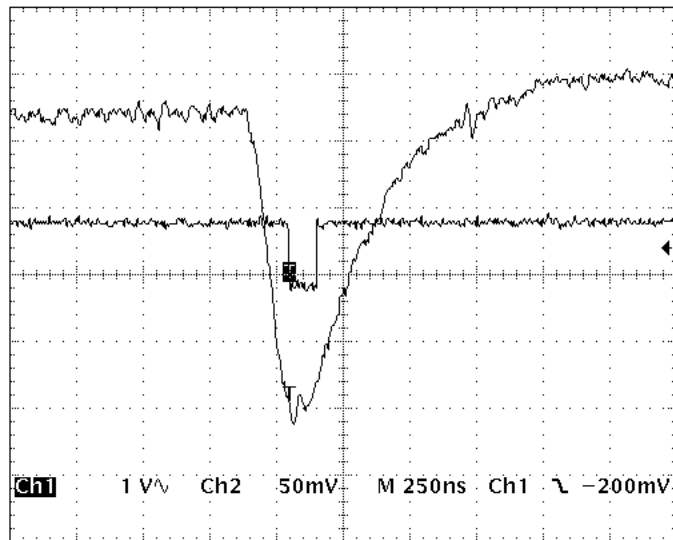
Figure 3.14: A typical analog signal after amplification on the MuID Read Out Card.

PHENIX beam clock, these six 16-bit values are collected and directed in two separate paths. First, the 96-bit data is inserted into a data buffer (FIFO) awaiting a signal from the Level 1 trigger that this data should be archived. Second, these data are transmitted via optical fiber to the MuID Local Level 1 trigger. This trigger was not active during Run II, but is planned to be operational in Run IV. When appropriate the PHENIX Global Level 1 Trigger (GL1) transmits a level 1 accept to the MuID FEM which is then relayed to all twenty ROCs in that crate. A configurable latency is then used to associate that level 1 accept with the data previously inserted into the data FIFO. The FEM then requests the data from each ROC one by one via the digital backplane to compile a packet of 120 16-bit words which are then transmitted to the PHENIX Data Collection Module (DCM).

3.4.3 The Data Acquisition System

Every subsystem is equipped with a Front End Electronics (FEE) system providing a standardized output of the subdetector. Every 106 nanoseconds the FEE reads all channels of the subdetector and stores the information in an internal buffer. Each FEE operates on a common timing signal from the Granule Timing Module (GTM) that facilitates a synchronized snapshot of the entire detector. The GTM provides all communication to the subsystem FEE.

While each subsystem FEE continuously takes a snapshot of the detector every beam-clock, it is the responsibility of the Data Acquisition System (DAQ) to decide whether the event is interesting and then to retrieve the information from the various subsystems to be archived. An overview of the DAQ is presented in Figure 3.15. Since not every beam-clock contains something interesting, a subset of the detectors provide the DAQ with information that can be used to quickly evaluate the usefulness of the event. These local level 1 (LL1) subdetectors are equipped with electronics that provide the common PHENIX Global Level 1 (GL1) with the synthesized information of that subdetector. The GL1 synthesizes the input of all LL1 detectors. If the combined information satisfies a Level 1 trigger condition, the GL1 informs the GTM that a signal to each subsystem should be made requesting that the information of the subdetectors be transferred to the DAQ. The subsystem FEE packages the subdetector's information and transfers the information for the requested event to the DAQ Data Collection Modules (DCM). The DCM's perform varying zero-suppression algorithms and prepare the data for the Event Builder system. The Event Builder is a farm of computers which collect the data from the various DCM's and combine it into one event. Since this is the first opportunity for the data to
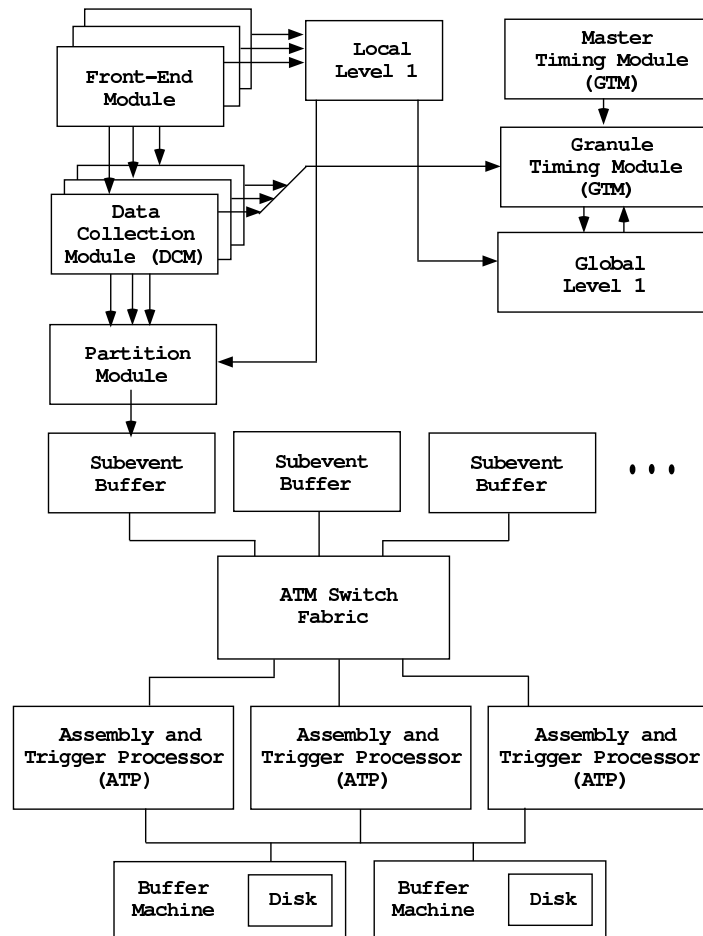
Figure 3.15: The PHENIX Data Acquisition system [16].

be examined for the entire detector, the level 2 algorithms are applied on the event builder.

3.4.4 Triggering

3.4.4.1 Minimum Bias Triggers

The primary minimum bias trigger for this data set is the Beam-Beam Local Level 1 trigger. The BBLL1 trigger utilizes the timing measurements of north and south BBC's to quickly estimate the point of collision along the beam axis and trigger on collisions within a specified vertex window. During the Au+Au run of 2001 the BBCLL1 required a collision vertex between +/- 40 cm. Within this vertex range a trigger efficiency of $93.1\% \pm 0.4\% (stat.) \pm 1.6\% (syst.)$ was achieved.

3.4.4.2 Level 2 Muon Triggers

Preparations for efficient use of a predicted high luminosity run included the development of a Level 2 triggering framework to enhance rare physics signals of interest to PHENIX. The expected collision rate for RunII Au+Au was 1.4 kHz which was dramatically lower than that predicted for the p+p run at 250kHz. While both are greater than the PHENIX data archiving rate of 20MB/s, the dramatically different occupancies drove us to two very different triggering schemes. The low occupancy of p+p collisions allow for very fast hardware based algorithms that are implemented in the PHENIX level 1 framework. However, for Au+Au the high occupancy requires and the lesser collision rate allows a more sophisticated and time consuming triggering algorithm implemented in the PHENIX level 2 framework. Analysis at level 2 re-

quires that the data from each event fall within the DCM bandwidth which is applicable to

Au+Au collision rates but not p+p.

The primary rare physics interest in the muon channel for RunII was J/ψ production. To enhance this signal, a Level 2 dimuon trigger was developed. An algorithm had already been developed for hardware implementation that could be easily adapted to the software. Since the algorithm was designed to use logical operations, we were confident that it would fit our limited CPU budget. The course segmentation and logical readout of the MuID detector result in a countably finite set of patterns in the MuID that can be formed from a track originating at the nominal collision point. Like the offline road finding algorithm tracking is first performed independently in each orientation. Thus, the trajectory of a particle following a perfectly straight path would intersect a set of MuID two-packs with a constant slope. This set of two-packs forms the centroid of a group called a symset. Since a real particle will multiply scatter within the MuID absorbers, adjacent two-packs are included within the set, closest two neighbors in the second plane, closest four neighbors in the fourth plane, and so on as shown in Figure 3.16. This increasing window also accommodates the deviation of a track from this nominal slope when the initial collision is not at the nominal vertex.

The hit pattern of every symset of the entire detector is evaluated to determine whether it satisfies the trigger conditions. If a hit is located on the centroid channel of either the first or second plane the following plane is searched in a three channel window centered at the location of the hit in the previous gap. If a hit is located within this window, the process repeats for the next plane. If a hit is not found in the current gap, the search window is widened in the

72
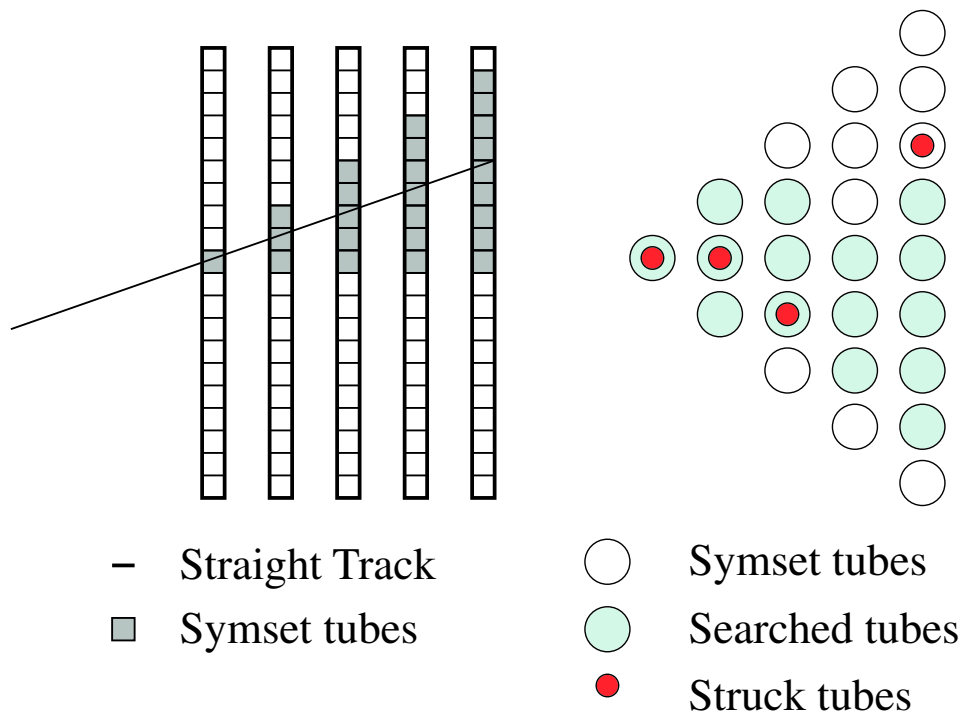
Figure 3.16: Level 2 Symset definition: Left panel diagrams five MuID planes with shaded two-packs belonging to the symset associated with the straight line track. Right panels diagrams an example hit pattern for one symset. The shaded circles are the two-packs included in the search determined by location of the hit in the previous plane.

following plane to five channels centered at the location of the last found hit. The right panel of Figure 3.16 demonstrates an example hit pattern for a symset that results in triggered symset to a depth of the third gap. A real track is likely to trigger not only the symset centered on the track path, but also the adjacent symsets. A simple edge finder provides ghost rejection. If consecutive symsets are fired, only one candidate is retained for subsequent consideration.

The algorithm planned for implementation in hardware forms the logical OR of all channels at the same slope within a given gap. While this will serve well for the low luminosity p+p collisions, concerns that this would limit the rejection power of the trigger in the high occupancy Au+Au environment drove us to a finer segmentation. One possibility would have been to independently consider the two-packs of each panel over the entire depth of the detector. However, tracks that are near the east and west edges of the small panels will transition to the inner edges of the large panels. Tracking within each panel independently would result in the loss of acceptance for such tracks. Instead the two-packs of the six panels within each plane were grouped into eight virtual panels: four upper logical panels and four lower logical panels. For the horizontal orientation the outer logical panels were formed by considering only the channels of the large panels. However, for the inner virtual panels the channels from both the inner panel and the large panel on the respective side are combined. Therefore, a track intersecting a small panel at shallow planes and large panels in deeper planes is contained in these inner virtual panels.

The result of processing all virtual panels for both channel orientations is a set of fired symsets and the corresponding depth to which they were tracked. These are stored as a level 2 primitive within the level 2 framework. Figure 3.17 diagrams the path of this low level primitive

Database Primitives   **Data Primitives**   **Decision Algorithms**

L2MuildXoZ
idxXoZ
[kNumArms]
[kOrientations]
[kNumSymsets]

L2MuiPairs	::Track2D_st
pnum	id1
mupairs	id2
calculate	openangle
	mass

\<uses\>

L2MuiTrigPar
swi[5][5]
showercut[5][5]
maxskip[5][5]
maxmisshits[5]
maxmisstotal
depthmatch
peripheral
anglecut
angleacceptance
shallowgap
pmin[2][5]
openanglecut

\<uses\>

\<uses\>

\<uses\>

L2MuiTracks	::Track2D_st
pnum	hid
tracks	vid
calculate	depth
	panel
	direction[3]
	pmin

\<uses\>

L2MuiSymset CalcPerPanel	::muiSymset
pnum	idx
arm	cos
orientation	depth
panel	gapbit[5]
nhitspergap	
nroads	
symsets	
calculate	

\<uses\>

L2MuiDBPrimitive	::Logicaltube
mui_logical_tubes	idx
[kNumFems]	gap
[kNumRocsPerFem]	panel
[kNumWordsPerRoc]	
[kChannelsPerWord]	

\<uses\>

\<uses\>

L2MuiData Accessor	::hit_st
packetid	roc
hits	word
calculate	channel

Figure 3.17: Muon Level 2 Trigger Overview

from the raw data accessor to a muon trigger decision. Symsets of opposite orientation within a virtual panel are compared for consistency, and then combined to produce a L2MuiTrack primitive. The consistency checks are important to reject false combinations resulting from multiple tracks entering the same panel and from combinatoric background. The symsets of opposite orientation must differ in tracked depth by no more than one plane. These track candidates are then considered by single muon triggers. For the dimuon triggers an additional L2MuiPairs primitive is formed by considering pairs of track primitives. A cut on the angle between the tracks is imposed to reduce false triggers from ghosts.

The figure of merit for a rare event trigger is signal efficiency × rejection factor (RF) where the RF is the ratio of considered events to accepted events. However, the modifications that would improve efficiency at the same time increase the susceptibility of the trigger to background and thus a loss in rejection. The muon level 2 trigger algorithms were optimized by studying their performance in simulation and attempting to balance rejection and efficiency. One-thousand minimum bias Hijing events were used to calculate rejection factors and one-thousand Pythia J/ψ events were used to calculate acceptances and efficiencies. It was assumed that efficiency would not be strongly anti-correlated with the expected occupancies of Au+Au. The Hijing events were produced without bias on impact parameter. The response chain used to generate the background input assumed 97% two-pack efficiency. The J/ψ events were thrown with a loose filter on the south muon arm acceptance, daughter-muon angles and momenta. Three different response chains were used to generate the signal input files varying the two-pack efficiency as shown in Table 3.3. The denominator of our acceptance and efficiency

76

Table 3.3: Level 2 Trigger Efficiency

Two-pack Efficiency (%)	100	97	90	RF
Dimuon Efficiency	86	84	71	20
Dimuon, Polar Angle $\geq 15°$	62	60	52	11

calculations is given by the number of J/ψ's for which the daughter muons in the 100% two-pack efficiency case recorded hits in the first three MuID gaps (a total of 750 of the thrown J/Psi's). The raw yield of these J/ψ's into the South Muon Arm is shown in Figure 3.18. Tighter cuts on track primitives were explored in an effort to maximize rejection; however, the trigger efficiency depended too strongly on the detector efficiency.

As the run began and real data became available, occupancies in the MuID were far greater than expected from previous simulations. Two unexpected sources of background were observed and verified in an improved simulation as discussed in the next chapter. The partial shielding of the MuID detector meant that small MuID panels located above the beam pipe would have high occupancies throughout the run. In order to meet trigger bandwidth requirements the upper virtual panels were removed from the muon level 2 triggering resulting in a 30% loss of efficiency for the J/ψ. Furthermore, both muons of a dimuon candidate were required to penetrate to the deepest plane of the MuID resulting in an additional efficiency loss of 25%.
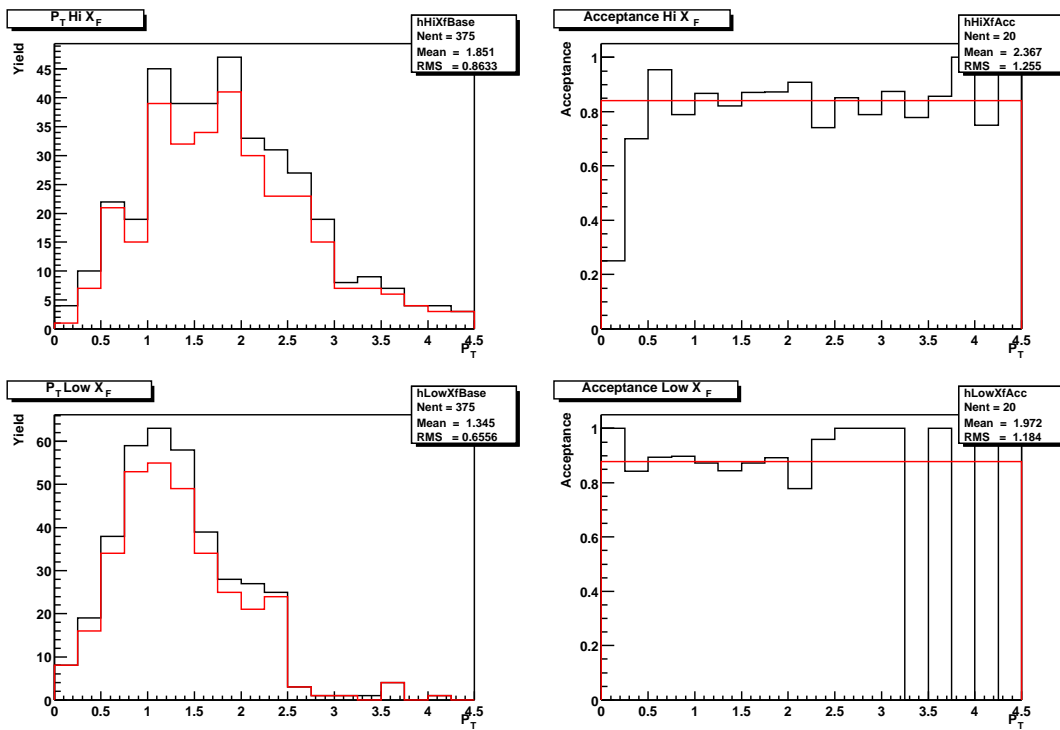
Figure 3.18: Muon Level 2 Acceptance for J/ψ requiring deeply penetrating muons.

Chapter 4

Data Reduction

The Au+Au run of RHIC Year 2 was the first year Au nuclei were collided at design energies of $\sqrt{s_{NN}} = 200 GeV$. While the PHENIX Central Arms had already operated the previous year observing lower energy collisions, these collisions were the first ever recorded by the PHENIX Forward Spectrometers. It was a tremendous accomplishment for the collaboration to have brought such a complex detector through its construction to actually taking snapshots of the most energetic collisions ever formed in the laboratory. Nevertheless, many aspects of the detector performance and design were realized only after the final assembly or after the run began. Some early observations of less optimal detector performance resulted in modifications to the detector during the run while others could not be fully addressed and the ramifications are still being resolved via software in the offline analysis. This section will describe the procedure used to render a physics signal from the experimentally recorded data.

4.1 Event Selection

The Au+Au collisions recorded in PHENIX for Run II can be divided into three distinct time periods as demonstrated in Figure 4.1. As the run progressed and machine performance improved the luminosity steadily increased, so that almost half the data was recorded in the last two weeks of the run. This section will discuss the limitations of these periods and justify the selection used in this analysis.

As soon as the first recorded data of real collisions could be analyzed, a discrepancy between the MuID occupancy of the real data and that expected from simulations was realized; the real data had about twice as many hits per minimum-bias Au+Au collision as indicated by the simulation. This high occupancy would hinder physics interests in two ways. First, the Level 2 trigger developed to enrich the J/ψ signal would not fall within the budgeted bandwidth. In the expected high-luminosity running the trigger would necessarily be pre-scaled limiting the sampled luminosity. Second, the offline performance of the detector would be diminished with regard to muon identification and efficiently seeding the muon track-finding. Improved simulations and experimental measurements demonstrated that the increased occupancy was due to collision particles at rapidities much larger than the acceptance of the MuID. These forward particles interacted with material along the beam line that travels through the unshielded "square" hole of the MuID. The solution would be to completely shield the MuID chambers from the beam line. This solution could be only partial implemented during the run leaving the MuID chambers above the beam pipe unshielded. The success of the shielding in reducing the occupancy is demonstrated in Figure 4.2. The upper unshielded panel is excluded from the
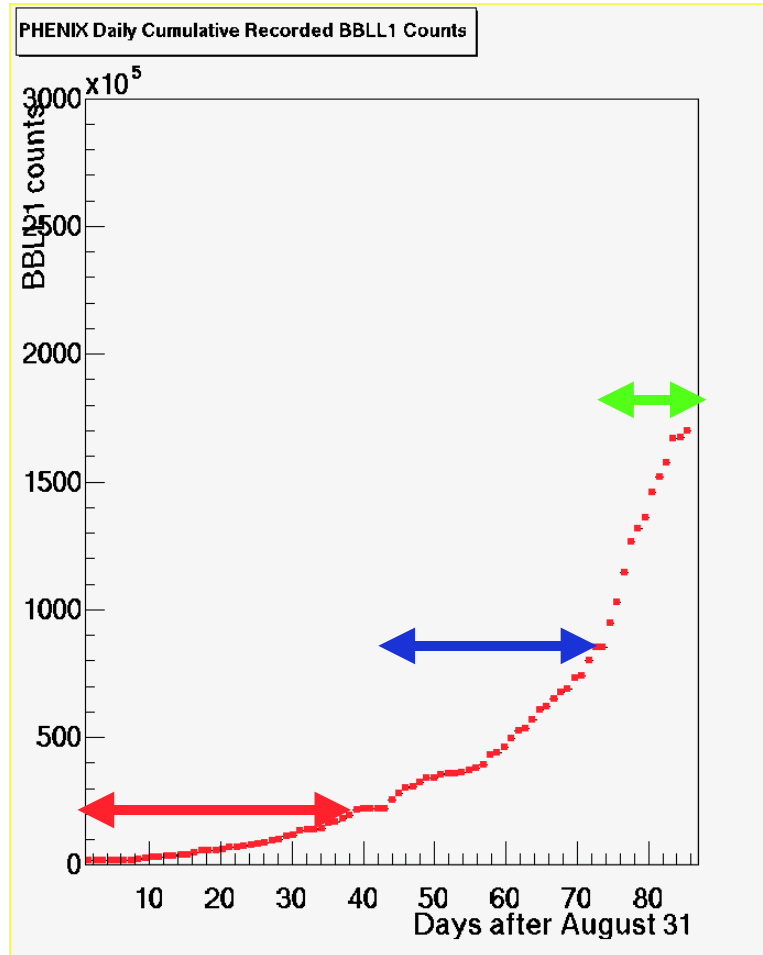
Figure 4.1: Integrated Luminosity of Au+Au collisions as a function of time. For the purposes of muon analyses the run can be divided into three segments. The first is characterized by low collision luminosity and pre-shielding high occupancy in the MuID. The second is characterized by low collision luminosity but lower occupancy in the newly shielded areas of the MuID. The last is characterized by high collision luminosity utilizing the Level2 Muon Trigger and high beam-related occupancies in the MuID.
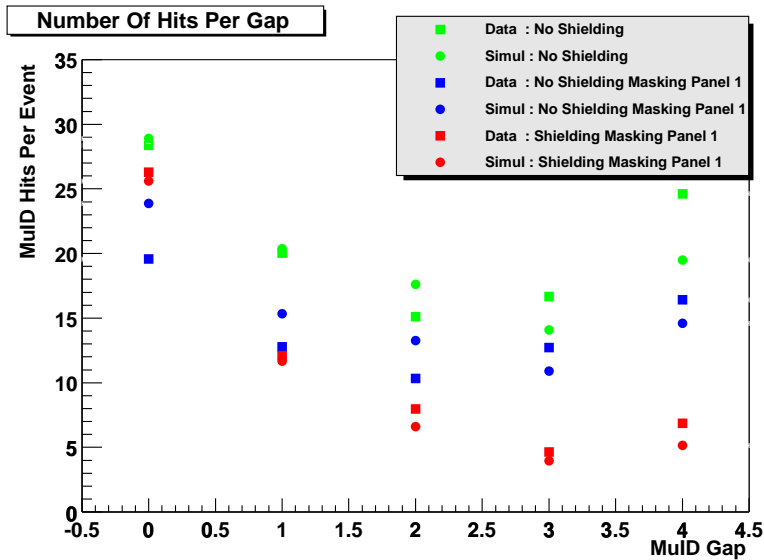
Figure 4.2: MuID Occupancy before and after Shielding Installation

blue and the red points. Note that the first plane of the MuID (Gap0) could not be shielded. In fact, the data indicate an increase in the occupancy of gap 0 after the shielding installation. It is possible that the additional shielding material provided a source for the high rapidity flux to shine onto the unshielded panels of the first plane. The shielding was observed to dramatically reduce the occupancy in the deeper planes of the MuID. In the deepest plane the shielding reduced the occupancy by more that a factor of 2. The large occupancies in the unshielded MuID then characterize the first of the three periods.

The second period is characterized by much lower occupancy for the majority of the MuID chambers. The beam luminosity during this period was sufficiently low to allow PHENIX to record all collisions without pre-scale of the minimum-bias triggers. The performance of both the Muon Tracker and Muon Identifier are well understood with regard to active high-voltage

for any data collected within this period.

The third period is marked by a dramatic increase in the collider luminosity. Unfortunately, the higher luminosity was accompanied by a new source of background for the Muon Identifier. What is now known to be beam-related background coming upstream in the collider tunnel was so severe as to produce large current draws in the MuID chambers. Snap shots from the experimental HV monitor are shown in Figure 4.3; the left panel indicates high currents for channels servicing the deepest gaps which have less shielding from the beam tunnel. The upper panels are not shielded from upstream beam related background by the tunnel mezzanine flooring as are the lower panels. The right panel demonstrates that under some beam conditions much of the detector was inundated with this background. For the channels that were not tripped, the resulting drop in high-voltage across the chambers dramatically reduce their efficiency. This background has since been studied extensively in the deuteron-gold collisions of RHIC Run III. Three scintillators placed inside the tunnel upstream from the North MuID were triggered in coincidence with the MuID deep-road trigger. Analysis of that data reveal a large number of tracks originating along the beam line in the tunnel. Figure 4.4 is the distribution of the track intersections along the beam axis and demonstrates a significant contribution tens of meters upstream. In future running, this background will be largely eliminated by the installation of shielding inside the tunnel. While half the sampled luminosity is in this third period, these factors prevent a useful study of this data.

This analysis will therefore include only the middle period after the shielding installation but prior to the high-luminosity running. We will consider two more criteria for the selection
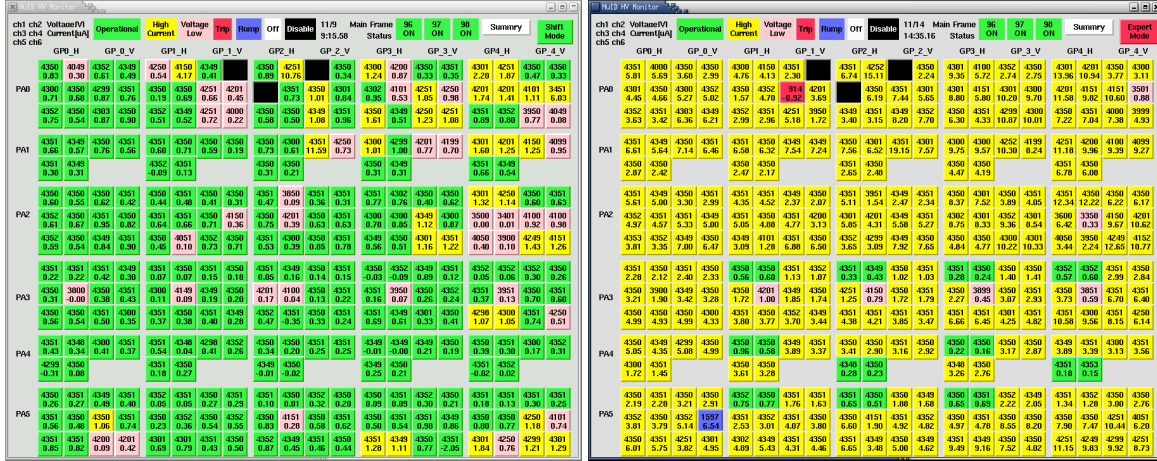
Figure 4.3: MuID HV Status during two different beam stores during the high-luminosity Au+Au run. The yellow channels indicate high currents in the chambers due to high hit rates. Left panel shows high currents in most susceptible chambers. Right panel demonstrates that some beam conditions affected the entire detector.
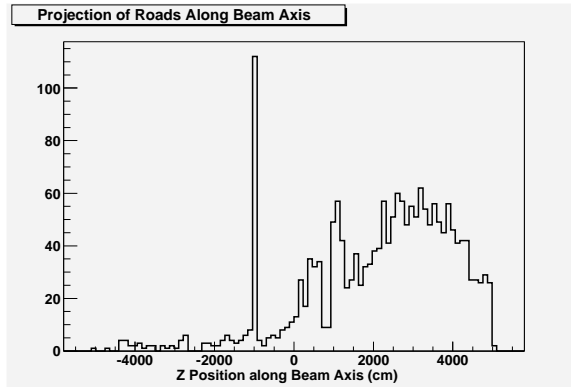
Figure 4.4: The projection onto the beam axis of MuID roads. Roads are reconstructed from a special run triggered by the North MuID BLT trigger in coincidence with scintillators located in the beam tunnel upstream from the North Muon Identifier. The artificial peak at -1000 cm is due to roads for which no intersection with the beam axis was found.

of events, the MuTr high-voltage status and the vertex of the collision along the beam axis. The muon tracker high voltage system was on the whole very stable for the commissioning run, but there was a significant fraction of the detector which could not be consistently activated. Figure 4.5 records the fraction of channels that were enabled for each PHENIX run. Only runs with 82.5% of the detector active and no high voltage channels trips during the run will be used. A total of 203 physics runs were taken during this period out of which 98 had at least one MuTr high voltage trip and 53 of which are below the 82.5% duty fraction cut leaving 87 runs to be analyzed.

From this period 7.6 million minimum-bias events were fully reconstructed in the offline analysis and were determined by the beam-beam counters to have a collision vertex within 40 cm of the nominal interaction point. The minimum-bias triggers are estimated to sample 92% of the 6.9 barn Au+Au inelastic cross section[1]. The integrated luminosity is $\int \mathcal{L} dt = 1.1 \mu b^{-1}$.

The dominant source of physics related background in the dimuon spectra result from the decay of pions and kaons to muons prior to reaching the south nose-cone. If the collision vertex is far from the absorber more of these hadrons will decay to muons that will penetrate into the south spectrometer. The hadrons from collisions occurring near the absorber have less time to decay. This trend is illustrated in the vertex dependence of dimuon yields of Figure 4.6. Deviation from this trend become significant for collision vertices near the south absorber. Particles of these collision do not traverse the entire material and are not as readily absorbed. This same deviation is also seen in single muons during p+p run and the deviation begins at a vertex of -20 cm shown in the left panel of Figure 4.6. The source of this additional component (or the rise in
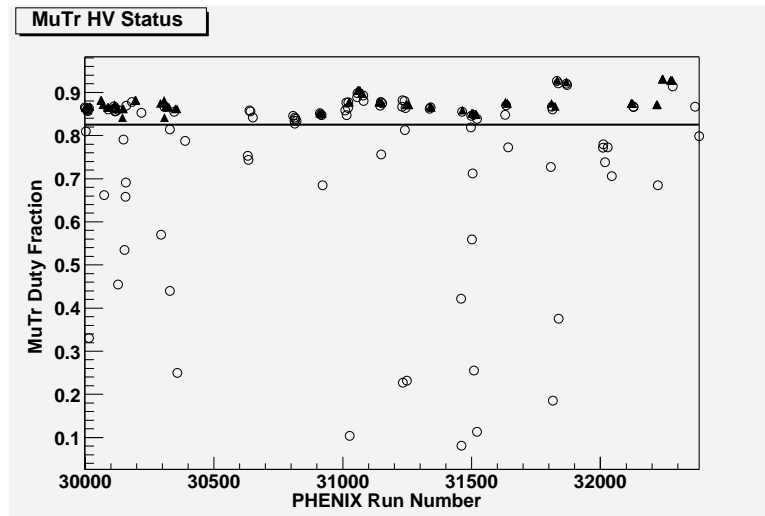
Figure 4.5: For each PHENIX run the fraction of high voltage enabled for that run shown. The closed triangles are runs used in this analysis. The open circles are runs for which less than 82% (horizontal line) of the MuTr high voltage was enabled or runs for which at least one high-voltage channel tripped during the run.
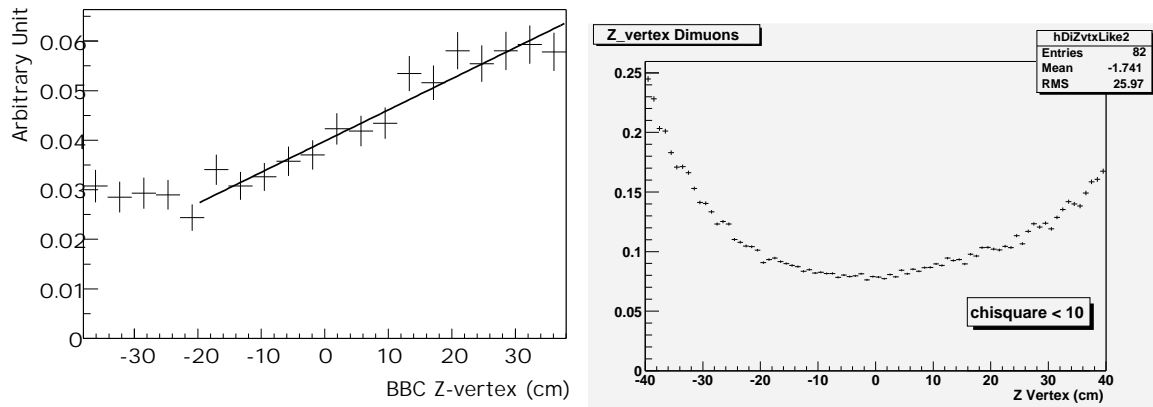
Figure 4.6: Single and dimuon yields show strong dependent on collision vertex. Single muons (left panel) yields depend on collision vertex in proton+proton run [15]. The yield of dimuon candidates (right panel) in Au+Au run dominated by uncorrelated single muons also depends on the location of the collision along the beam axis.

86

the relative contribution of one the previously mention sources) has not been extensively studied for this vertex range. Therefore, collisions of $z_{vertex} < -20$ cm will be excluded; remaining are 5.7 million minimum-bias events or $\int \mathcal{L} dt = 0.83 \ \mu b^{-1}$.

4.2 Muon Offline Reconstruction

The role of the offline analysis software is to transform the individual signals of thousands of electronic channels into a set of particle trajectories and corresponding kinematic descriptions. The complementing strengths of the MuID and MuTr are utilized in an iterative process to reconstruct each collision. This algorithm is diagrammed in Figure 4.7. First, crude roads are reconstructed within the Muon Identifier (MuID). The penetration depth through the MuID absorbers provides an estimate of the momentum of the particle. These roads provide seeding to the Muon Tracking which projects the course road through the three tracking stations and finally to the collision vertex. The details of this algorithm will now be discussed.

4.3 Muon Identifier Reconstruction

The MuID is a versatile subsystem that serves three distinct functions. Because of its relative simplicity and small event size, it serves as both a Local Level 1 trigger and a Level 2 Trigger. The interleaving of absorber material with detector chambers facilitates the separation of leptons and hadrons. Furthermore, it provides a clean sample of potential tracks with which to seed the Muon Tracker reconstruction. In this section we will examine the performance of the detector combined with offline tracking to fulfill this latter role.
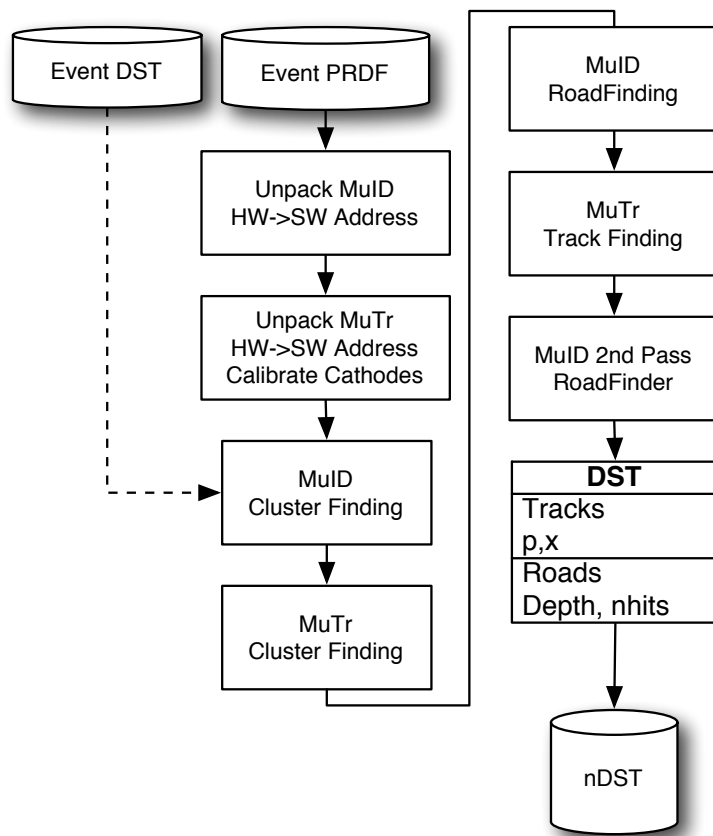
Figure 4.7: Overview of Event Reconstruction of Muon Arms.

4.3.1 First Pass Road Finder

The First Pass Road Finder is an algorithm implemented in offline software and is designed to recognize correlations in hits of the MuID that are likely to be associated with a particle passing through the detector. By collecting the hits associated with a single track and excluding all other hits, the trajectory of the particle is best determined. At this stage the estimate of the track trajectory must be optimized to provide the best extrapolation to Station III of the Muon Tracker. Since inclusion of an unassociated hit will decrease the projection accuracy, failing to include some associated hits is favored over including unassociated hits. The details of this algorithm's attempt to balance these competing factors will now be discussed.

4.3.1.1 Road Seeding

The Road Finder uses an iterative filtering method to reconstruct tracks in the MuID first in one dimension followed by combining the 1D tracks of opposite orientation. The measurement points are essentially the five planes of the MuID and the nominal vertex. Any subset of the MuID planes can be considered in any order. This facilitates calculating hardware efficiencies by excluding the plane under investigation, and allows the algorithm to be optimized against the higher occupancy of the planes nearest the interaction region. There are two distinct ways to seed the filtering. First, the nominal vertex may be considered in combination with hits of the first search plane. This is useful if the vertex of the interaction is well determined by other detectors. However, inefficiencies will be more likely for particles which undergo significant multiple scattering. Second, hits of the first search planes may be combined independent of

the nominal vertex. The projection of the candidate to the next search plane may then be made without preference to vertex particles. While this is useful when the interaction vertex is not well known, it is more susceptible to random combinatoric background.

To increase efficiency the Road Finder may use multiple seeding methods and multiple plane search orders on the same event. If the MuID hardware were perfectly efficient and in as much as the absorbing layers do not cause tracks scatter significantly from a strait trajectory, each iteration over the planes in a different search order would produce the exact same set of roads. The utilization of multiple orders of search then limits the dependence of the algorithm on the hardware efficiency of one particular plane that might be used at a critical seeding stage and also limits susceptibility of the algorithm on the overall efficiency. This aspect of the algorithm also improves efficiency for a track that is dramatically scattered beyond the search windows to the subsequent gap. This inevitably produces duplicate roads that are weeded after all combinations are considered.

4.3.1.2   One Dimensional Roads

Once a seed is constructed by either method, it is projected to the next search plane as demonstrated in panel 2 of Figure 4.8 and a list of hits within a search window is found. Since the hardware channels overlap in the transverse plane, there is an 8% likelihood that two channels will be fired. Furthermore, a separate track which passed through another part of the MuID panel may also fire a tube within this window. Therefore, the road finder will consider the combination of the projected seed with each hit as separate candidate as in panel 4 of Figure 4.8. If there is no hit within the window then adjacent panels are examined for hits within the window.
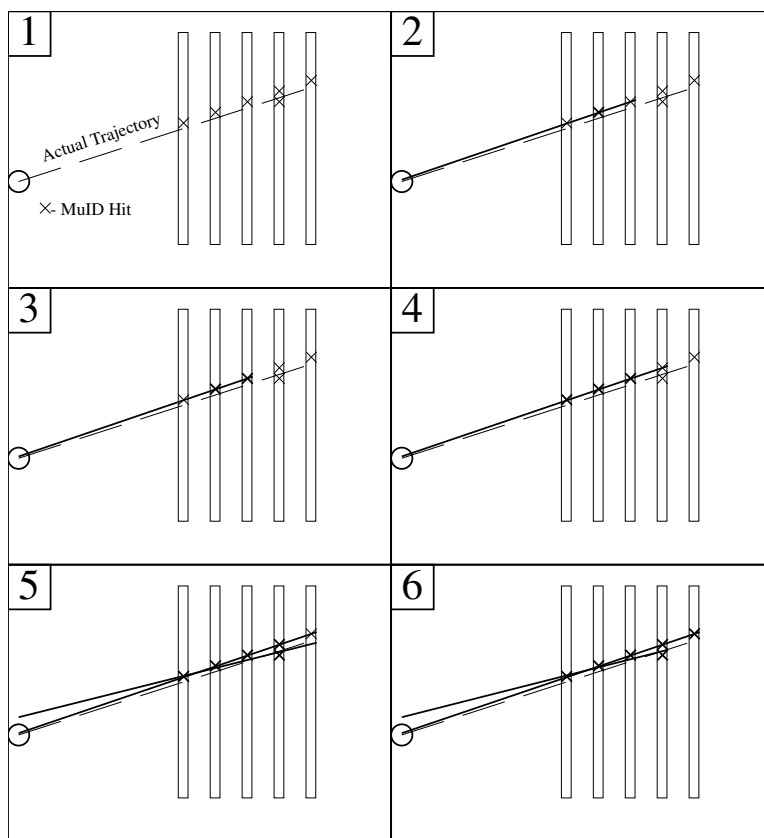
Figure 4.8: A schematic overview of reconstruction in one MuID orientation is demonstrated in the example hit pattern. Panel 1 shows the actual track trajectory (dashed line) and the associated hits of one orientation in each panel. Panel 2 is the seeding of the road (bold line) by associating the hit of the second plane with the nominal vertex. Panel 3 is the projection of the road to the third plane and association of a hit found within a fixed window (typically 5 channels wide). Panel 4 is the projection of the road to the fourth plane where there are two possible hits. Panel 5 is the bifurcation of the seed road into two road candidates each associating a different possible hit at the third plane. In Panel 6 both roads are projected to the fifth plane but a hit is only found for within the search window for one of the roads. Two roads are reconstructed: one to depth five and one to depth four.

This must be done to follow a track at such an angle that it begins in one panel for shallow planes and then transitions to another panel for deeper planes. If one or more hits are found then each hit is combined with the seed as a separate candidate as before, but furthermore the road candidate without any associated hit is retained. This allows the possibility that no hit was in the current panel because of a hardware inefficiency. All candidate roads are successively projected or interpolated to the next search gap until we have tracked each seed road through the detector.

Once a set of one dimensional roads is made for each orientation, the set can be examined for duplicates and unlikely candidates. The following parameters are considered for removal road candidates and are tabulated in Table 4.1. The road must contain hits in two of the five gaps. The road must penetrate the third gap. While this is very efficient for the J/ψ this is a limiting factor for the ϕ. The road must also contain fewer than two skipped gaps. At this point it is also useful to remove any duplicate roads, since it is likely that the same exactly the same collection of hits will be found from different orders of search. So only one candidate for a unique set of hits is considered further.

4.3.1.3   Two Dimensional Roads

Roads of opposite orientation can now be paired. It is important to evaluate these pairs for consistency to reject false combinations. As the right panel of Figure 4.9 demonstrates, if two particles intersect the same panel there exists a stereoscopic ambiguity. We are unable to distinguish the crossing of two hits produced by a real particle and the crossing of two hits associate with different particles. For every N crossings associated with real tracks there exist

Table 4.1: First Pass Road Finder Parameters

Parameter	Value	Description
SeedLoop[0]	{-1,1,0,2,3,4}	Order that gaps of MuID are searched, -1 indicates that the vertex is the first measurement
SeedLoop[1]	{-1,2,1,0,3,4}	Order that gaps of MuID are searched, -1 indicates that the vertex is the first measurement
ClusterCollectMode	0	Should the RoadFinder use multi-hit clusters or just treat each hit as a cluster
minLastGap1D	2	Minimum Depth of a 1D road
minFiredGaps	2	Minimum number of gaps containing hits for a 1D road
maxSkippedGaps	2	Maximum number of gaps missing in the planes preceeding the last gap
minSharedHits1D	5	Number of hits required for roads to be considered ghosts for the same orientation.
maxXRef1D	180	Maximum distance of a 1D roads projection to the nominal reference plane z=0 in cm.
maxYRef1D	182	Maximum distance of a 1D roads projection to the nominal reference plane z=0 in cm.
minLastGap2D	2	Minimum Depth of a 2D road
maxDelLastGap2D	1	Maximim difference of the last gap of paired 1D roads
maxDelHitsPerGap	1	Maximum difference of hits per plane for paired 1D roads
maxDelTotalHits	2	Maximum difference of hits for all planes for paired 1D roads
maxXRef2D	180	Maximum distance of a 1D roads projection to the nominal reference plane z=0 in cm.
maxYRef2D	180	Maximum distance of a 1D roads projection to the nominal reference plane z=0 in cm.
maxXChisq	1000	Maximum reduced χ^2 of vertical road fit
maxYChisq	1000	Maximum reduced χ^2 of horizontal road fit
minSharedHits2D	8	Number of hits required for roads to be considered ghosts.
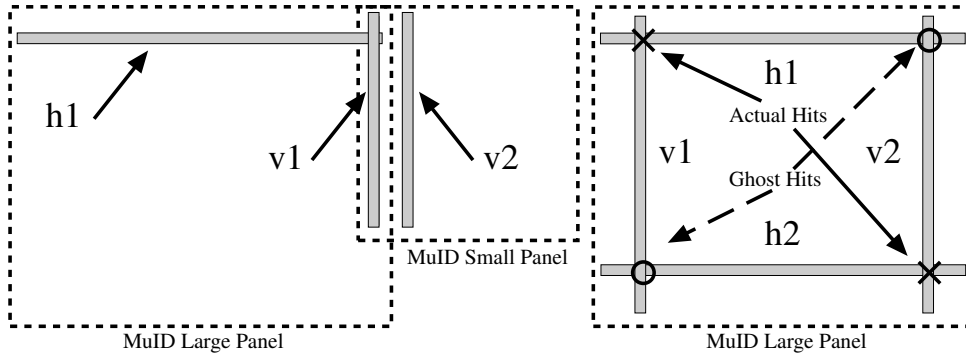
Figure 4.9: MuID RoadFinder diagrams. Left panel demonstrates the necessity of checking that hits of opposite orientation physically overlap. Right panel illustrates the stereoscopic ambiguities resulting from the geometry of the detector.

$N^2 - N$ false combinations. Since all gaps have identical geometry, the same is true for the pairing of 1D roads. This trend is observed in the reconstructed data. Figure 4.10 demonstrates a scaling greater than a linear dependence of the roads with hit occupancy. There appears to be a saturation at the highest occupancy due to the ghost rejection algorithm. There are additional factors that contribute to number of reconstructed roads.

- The segmentation of the detector into 6 panels per detector limits this ambiguity within a panel boundary; tracks that travel different panels are unambiguously resolved. This will reduce the number of false roads due to stereoscopic ambiguities.

- Second, MuID hits due to the background originating at the beam pipe are not correlated. In small numbers, this component readily contributes to ghosting of existing roads. However, at much larger occupancies this may contribute to false combinations which "appear" to be correlated. This is demonstrated in the greater number of roads reconstructed in the unshielded panels above the beam-pipe shown in Figure 4.11.

94
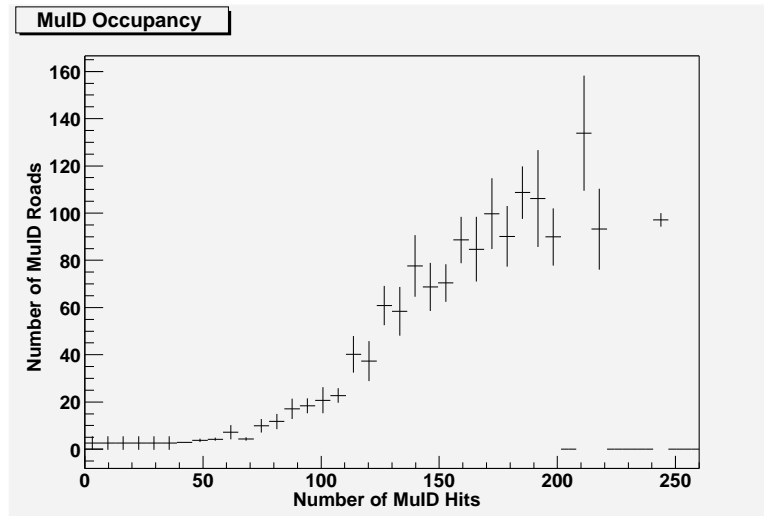
Figure 4.10: The number of roads per minimum-bias triggered event for the occupancies of a Au+Au collision.
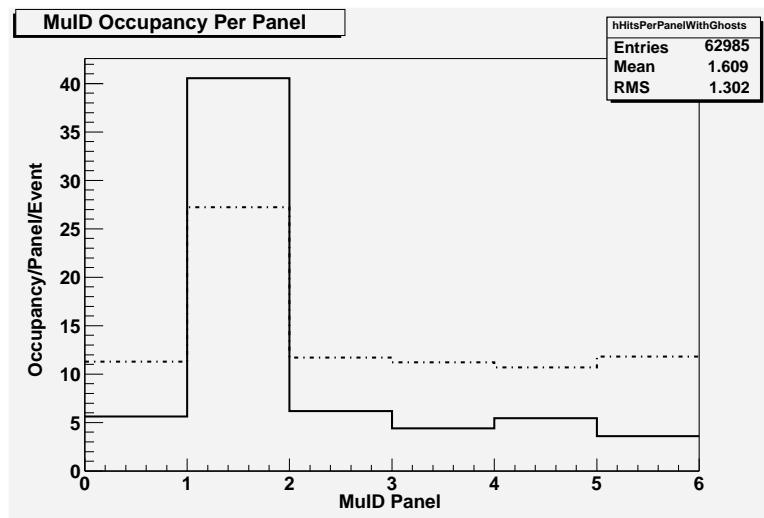
Figure 4.11: The number of hits (dashed) and roads (solid)per event for each of the six MuID panels (dashed): MuID panel 1 is the small panel located above the beam pipe. Occupancy is prior to MuID ghost rejection.

However, we can compare some characteristics of the 1D roads to reject the false combinations. First, the depth that roads of opposite orientation penetrate the detector should differ by no more than one MuID plane. If the detector was perfectly efficient we would require that the depth match exactly. However, allowing a difference of one gap compensates for hardware inefficiency in the last penetrated plane. Second, the two roads must basically contain the same number of hits. This would prevent matching a road of one orientation associated with a hadron to be matched with a road of the opposite orientation associated with a muon. Finally, the hits within each gap of each orientation are checked to see if they physically overlap. It is possible that a road of one orientation transitioned from one panel to another as discussed previously. A road of the opposite orientation that did not make the transition should not be paired with the previous road. As an example, a road containing the horizontal hit "h1" of shown in the left panel of Figure 4.9 could be paired with vertical hit "v1", but not vertical hit "v2".

4.3.1.4 Road Ghost Rejection

The Road Finder has now determined a set of roads by considering every unique combination of hits that is reasonable. The entire algorithm thus far is optimized for efficiency and will no doubt have produced multiple roads associated with the same physical track. These roads will be used to seed the track finding, and track fitting in the magnetic field is relatively costly in computing resources. Furthermore, similar roads are likely to produce almost identical tracks. Both in the interest of reducing processing time and accurately reproducing physics signals, it is necessary to group roads which are likely to be associated with the same tracks and pass only one road which characterizes the group to seed the Muon Tracking. Since efficiently seeding the

96

muon tracking is the prime deliverable of this process, we consider both similarity of the road in the MuID and its projection to station III. To determine whether a road should be part of a group we compare that road to each road within that group. The road is required to contain clusters within a fixed window of the hits of a group member in both orientations. The road is also required to project to MuTr station III within a fixed window of a group members projection. If both are satisfied the road is added to the group. If the road can be associated with more than one group, the groups are merged and the road is made a member of the resulting group. For each group one road is selected to characterize the group. This is achieved by projecting each road within a group to MuTr Station III and determining a median in the x-y plane. The road which projects closest to this median position is retained to seed further tracking.

4.3.1.5   MuID Reconstruction Performance

The performance of the MuID can be demonstrated by its efficiency and its precision in projecting to MuTr station III. By simulating the response of the J/ψ into the detector and subsequently reconstructing it, we can estimate its performance in these aspects. The performance is evaluated using the default reconstruction parameters in Table 4.1. The same software used to reconstruct real data is applied to simulation. If a road is constructed with at least 50% of the hits originating from the simulated particle, then that particle has been successfully reconstructed by the road finder. The reconstruction efficiency shown in Figure 4.12 is determined from simulation for several values of MuID hardware efficiency (the probability that a charge particle passing through a two-pack will register a hit in the electronics).

The MuID reconstruction efficiency for the J/ψ is somewhat dependent on the its kine-
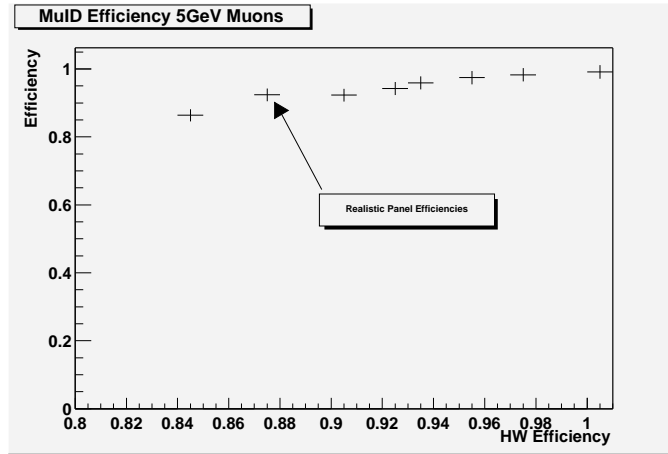
Figure 4.12: The simulated MuID reconstruction efficiency of 5 GeV/c muons is shown for several values of a detector channel efficiency uniform over the detector and a panel-by-panel efficiency extracted from real data.

matics and its decay polarization. Figure 4.13 indicates that within the acceptance transverse momentum does not seem to play an important role. However, the longitudinal momentum of the daughter particles does introduce some bias. If the longitudinal momentum of the J/ψ is large then it is more likely that both decay muons will penetrate the MuID. Figure 4.14 shows the x_F dependence of the efficiency. Specifically, if we require that all roads penetrate the entire detector in order to reduce background we will loose about 25% of the J/ψ signal predominantly for small x_F. One caution to aggressive ghost rejection is that the grouping of roads and selection method could select a less optimal road skewed by one or my outliers in the group; Figure 4.15 demonstrates the success of the ghosting algorithm in selecting the most appropriate road by providing an accurate projection to MuTr Station III. While multiple scattering makes this more challenging for lower momentum muons, Figure 4.16 demonstrates consistent precision for muons with momentum above 4 GeV/c.

98
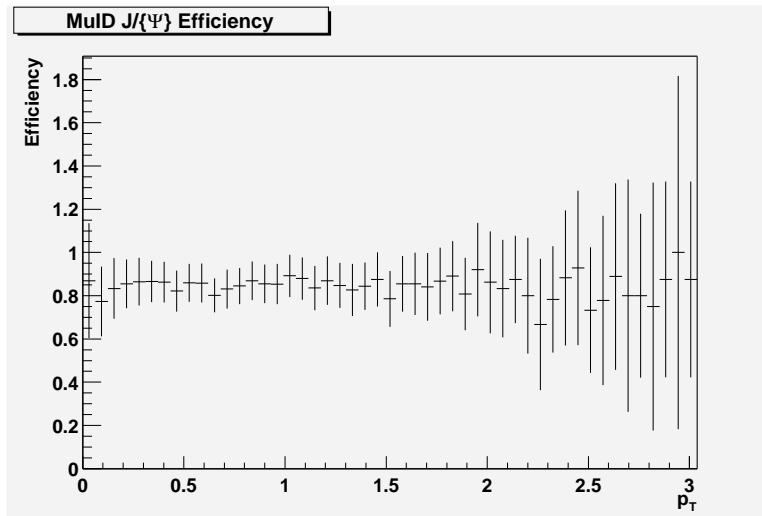
Figure 4.13: Transverse momentum dependance of MuID reconstruction efficiency of the J/ψ within the Muon Tracker acceptance using realistic MuID hardware efficiencies.
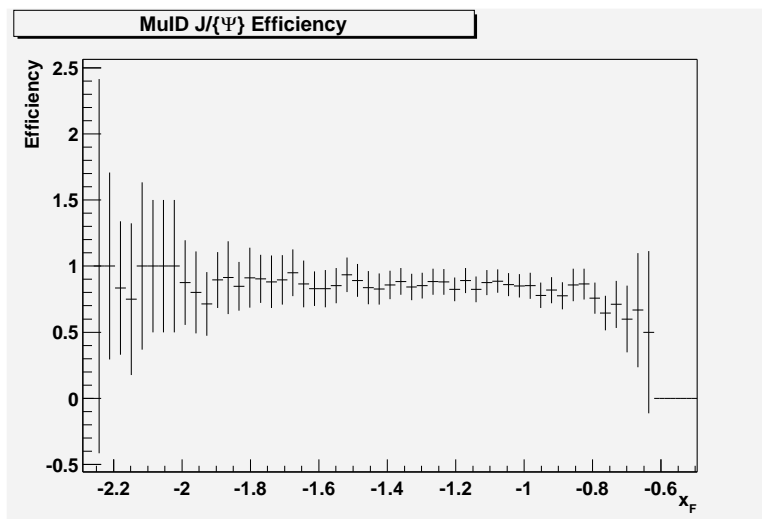
Figure 4.14: Longitudinal momentum dependance of MuID reconstruction efficiency of the J/ψ within the Muon Tracker acceptance using realistic MuID hardware efficiencies.
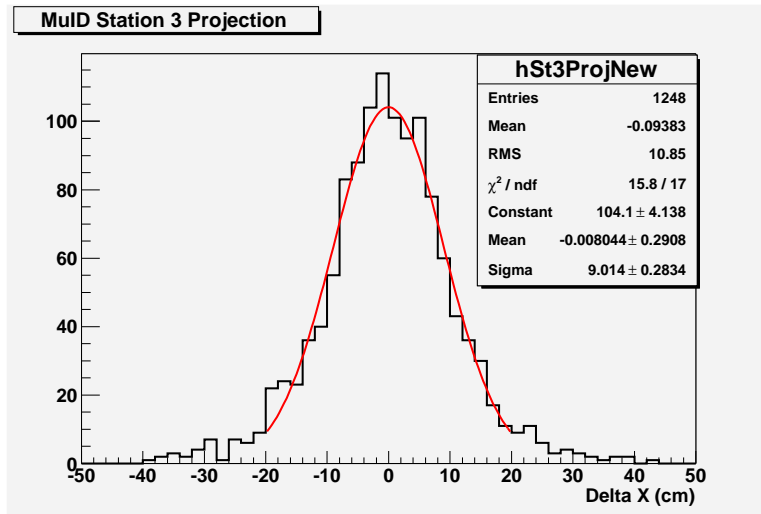
Figure 4.15: The accurate projection of roads to Muon Tracker Station III from J/ψ decay muons is demonstrated by the distribution of the residual of the projection with the simulated hit position in station III.
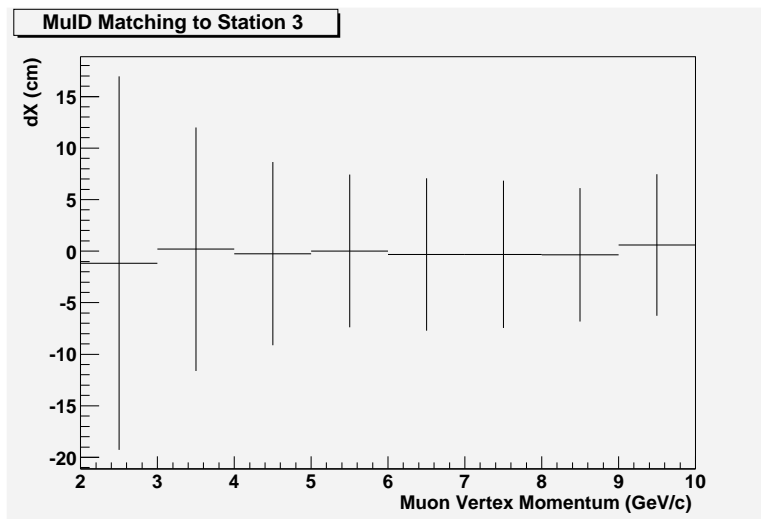
Figure 4.16: Projection of daughter muons of J/ψ roads to Muon Tracker Station III is much better for high momentum tracks due to deeper penetration gives more measurement points and there is less multiple scattering.

4.3.2 MuTr Cluster Fitting

The passing of a charged particle through a MuTr gap induces a charge on several cathode strips on either side of the anode layer as previously discussed in section 3.4.1. Typically, the induced charge is distributed over three cathode strips. A typical distribution is demonstrated in Figure 3.11. While the spacing of recorded strips is 1 cm, the fitting of a Mathiason function to the charge distribution provides a position resolution of 100 μm. An analysis of single particles from cosmic rays has confirmed this position resolution for regions of the detector where noise and gain fluctuations of the channels are less than 1% of the typical signal pulse.

4.3.3 Track Finding

Particles are reconstructed through the Muon Tracker by seeding Station III reconstruction from MuID roads and then extrapolating to stations closer to the collision point, station III to station II and station II to station I.

Each MuID road is projected to Station III and MuTr clusters that fall within a window centered about that intersection of that projection with Station III are grouped into a stub. The window must be wide enough to accommodate the coarse segmentation of the MuID and the multiple-scattering that occurs in the backplane of the magnet. However, a large window causes the algorithm to be more susceptible to forming false combinations of uncorrelated hits in the detector. The stub provides a local vector of the particles trajectory. During Run II significant regions of Station III had only one active gap. To remain efficient in these areas, stubs were created from the projections of MuID roads with as few as two cathode clusters from the active

gap. Based on the depth of the of the road into the MuID, a crude momentum estimate is then used to extrapolate the trajectory through the magnetic field to Station II. If a stub is found in station II within a window centered on the intersection of the extrapolation with station II, the clusters of station III and II are together fit to refine the trajectory and improve the estimated momentum. The window for considering clusters of station II is much smaller than that of station III given the finer resolution of the MuTr chambers over the MuID chambers. The subsequent extrapolation to station I allows an even narrower window to be utilized. The windows in the azimuth (ϕ) and polar (θ) angles are listed in Table 4.2.

Finally, the collision vertex measured by the beam-beam counters is used to fix the trajectory opposite the material of the central magnet and nose-cone. Corrections to the particle momentum and trajectory are made for energy-loss and multiple scattering in the material. Figure 4.17 illustrates the reconstructed tracks of simulated J/ψ daughter muons and Figure 4.18 shows the reconstructed mass for the J/ψ in a simulation with a realistic detector configuration providing 150 MeV mass resolution .

Table 4.2: Each station of the MuTr is assigned a search window reflecting the cumulative information available when hits of that station are considered within the algorithm.

Mutr Station	Polar (cm)	Azimuth (cm)
I	20	10
II	30	25
III	50	40
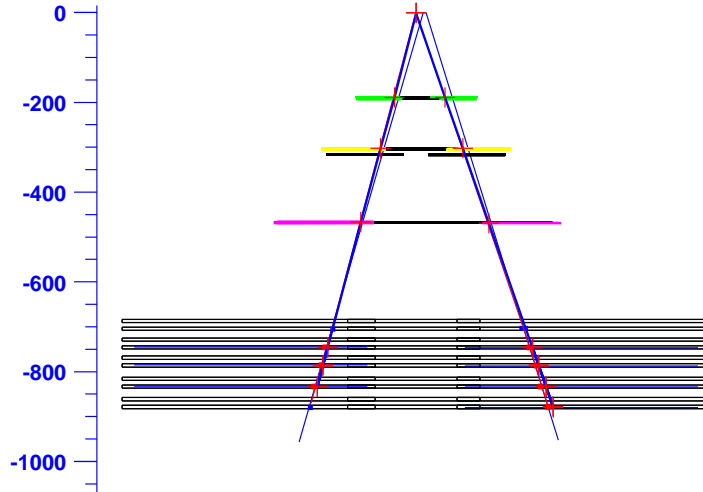
Figure 4.17: This PHENIX event display demonstrates the reconstruction of a simulated J/ψ event. The left axis is parallel to the beam axis so that the the J/ψ origin is at the top of the figure. Below then are the three MuTr stations and the five layers of the MuID.
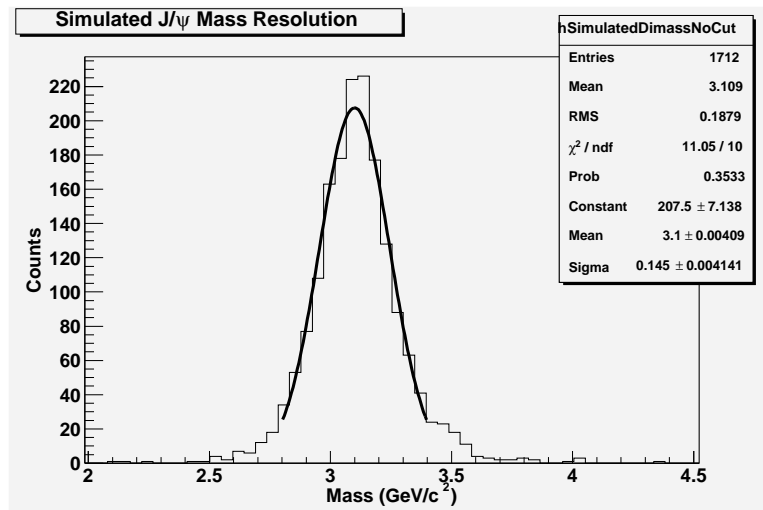
Figure 4.18: A realistic detector simulation and reconstruction yields the J/ψ mass peak with $150\mathrm{MeV}/c^2$ mass resolution. No background was present in this reconstruction.

4.3.4 Particle Identification

The muon arm is predominantly occupied by pions and muons from pion decays. The first can
be distinguished from vertex muons by capitalizing on two aspects of differing response in the
MuID detector. First, for a given momentum, a pion will penetrate less deeply into the MuID
than a muon of the same momentum. A muon only interacts with the absorber materal via the
Coulomb force as do all leptons, whereas pions additionally interact via the strong force as do
all hadrons. Second, as a pion ranges out in a MuID absorber a characteristic shower of parti-
cles may be produced resulting a wide cluster of hits at the deepest gap. These are promising
characteristics to be ensure the purity of a muon sample. However, high occupancies and low
Iarocci tube efficiencies of the detector's commissioning run have made practical application
very difficult.

In simulated embedding studies described later, 38% of roads that should have only been
tracked to the fourth MuID gap are actually tracked to the last gap. Presumably, this is the result
of an uncorrelated background hit within the search window of the road finding algorithm that
is incorrectly associated with the road. This analysis will not use any particle identification of
the MuID apart from the hadron rejection already afforded by the absorbing layers. The result is
that more J/ψ's will have both decay muons reconstructed to the deepest plane of the detector
in high occupancy events.

4.4 Detector Occupancy

A challenge of the heavy-ion analysis results from the drastically different occupancies of a peripheral and central collision. Station I is the closest to the interaction point and may be the most susceptible to background from collision particles at forward rapidities just beyond the detector's acceptance. Figure 4.19 shows the occupancy of the Muon Tracking chambers of each station for three centrality classes. The data indeed reveal that Station I has the highest occupancy of the three stations for most central events. A typical central Au+Au collision shown in Figure 4.20 illustrates the challenge of pattern recognition in high occupancy events.

4.5 Signal Counting

The number of J/ψ's reconstructed within the acceptance of the south spectrometer is determined by the following procedure. Each positively charged track is paired with each negatively charged track. The two tracks are assumed to be muons of $m_\mu = 0.106\text{GeV}/c^2$ and to be the only decay products of a single heavier particle. The invariant mass of this hypothetical particle is determined by the following equation.

$$M_{\mu^+\mu^-} = \sqrt{(\sqrt{m_{\mu^+}^2 + \vec{p}_{\mu^+}^2} + \sqrt{m_{\mu^-}^2 + \vec{p}_{\mu^-}^2})^2 - \vec{p}_{\mu^+} \cdot \vec{p}_{\mu^-}} \tag{4.1}$$

The momenta, $\vec{p}$, are the experimentally measured quantities at the collision vertex reconstructed from the particle trajectories in the magnetic field.

The invariant mass spectrum is shown in Figure 4.21. There are 72 counts in the mass region
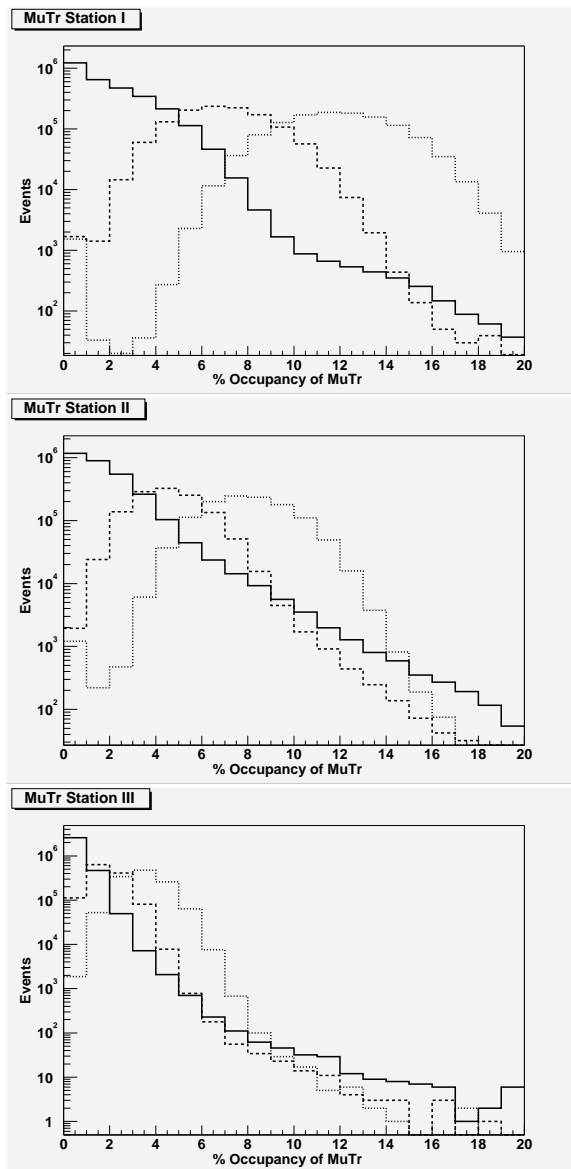
Figure 4.19: The hit occupancies of the Muon Tracker are shown for the three stations for three centrality classes, peripheral (40-90%) solid, mid-centrality (20-40%) dashed, and most-central (0-20) dotted.

106
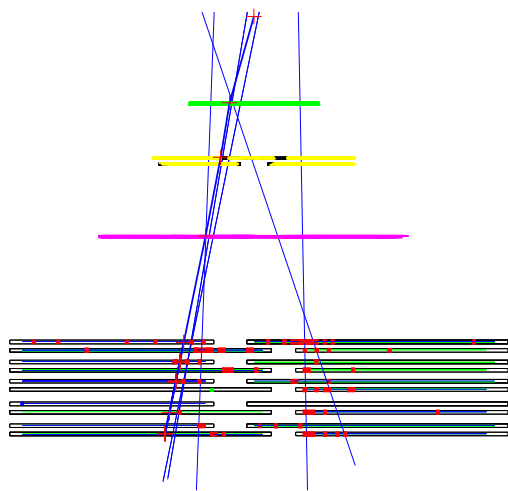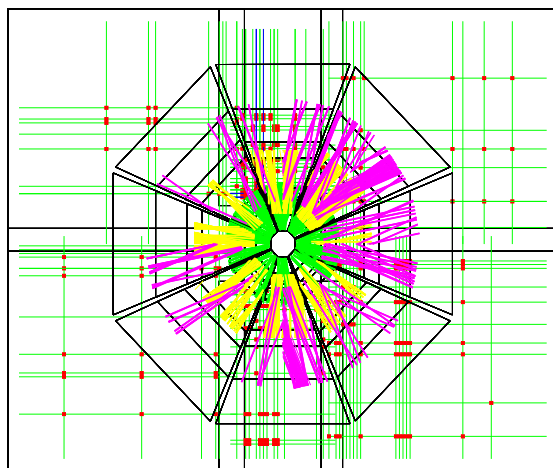
Figure 4.20: These PHENIX event displays of real Au+Au events demonstrate the challenge of reconstruction in a high occupancy environment. The upper panel is a view of the detector from the perspective of the collision point. The MuTr clusters of hit cathode strips fan radially outward and behind are the fired channels of the MuID horizontal and vertical layers. The lower panel is a side view of a real Au+Au collision illustrating the presence of MuID background near the beam pipe.
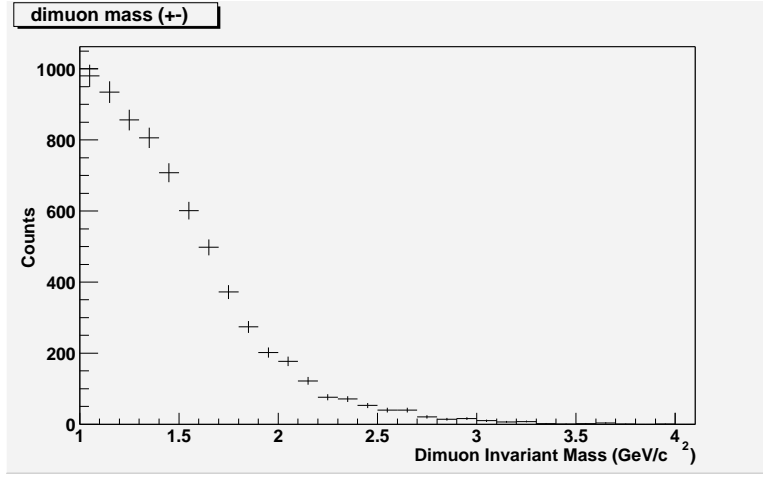
Figure 4.21: Invariant mass spectrum of opposite sign muon pairs.

$2.8 < M_{\mu^+\mu^1} < 3.4 \, \text{GeV}/c^2$. This region is chosen to accommodate a $2\sigma_{J/\psi}$ mass resolution of $160\text{MeV}/c^2$ as measured in the analysis of proton+proton collisions[17].

The majority of dimuons in the mass distribution are from uncorrelated tracks. This background component is well represented by forming the same invariant mass distribution from muon pairs of like-signed charge shown in Figure 4.22. There are 67 like-sign counts in the same mass region $2.8 < M_{\mu^+\mu^1} < 3.4 \, \text{GeV}/c^2$. The J/ψ yield is therefore $N_{J/\psi} = 5 \pm 12(stat.)$ which is not inconsistent with a null signal. Nevertheless, we will attempt to extract as much as these statistics offer. This method of measurement does attempt to isolate the directly produced J/ψ component; the J/ψ yield therefore includes contributions from decay feed-down from other charmonium states such as the χ_c. Contributions from B meson decays contribute less than 5% to the total J/ψ yield assuming both scale with the number of binary collisions [1].
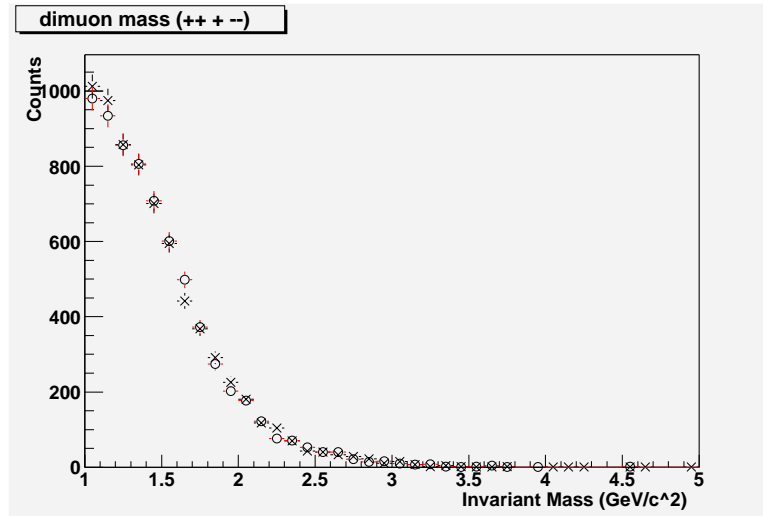
Figure 4.22: Invariant mass spectrum of opposite(crosses) and like(circles) sign muon pairs with identical quality cuts.

4.6 Efficiency Correction

Ideally we would measure the efficiency and acceptance of the detector for a specific signal like the decay muons of the J/ψ using a real source of that signal. If the exact kinematic description of the signal at its origin was know, it could then be compared to that as reconstructed by the detector. Unfortunately, there exists no such source; instead the acceptance and efficiency of the south spectrometer is calculated through a detailed simulation of the detector in the GEANT based PHENIX PISA framework. It is very important then that the simulation characterize the various aspects of the detector as accurately as possible. The position of the sensitive elements of the detector determine the geometric acceptance for single and multi-particle signals. We evaluate the acceptance of the detector and the efficiency of the reconstruction software by generating a realistic kinematic distribution of the signal and propagating these particles through

109

the virtual experimental apparatus within the simulation framework. The result of the simulation is a list of detector channels and associated detector response that are identical to that coming from the real detector. This allows the same software that reconstructs the recorded data to be used on the simulated signal to minimize any inconsistencies.

Realistic hardware efficiencies are incorporated into the simulation for both the MuID and MuTr. The MuID two-pack efficiencies are calculated by reconstructing real data of proton+proton collisions with a modified road finder that excludes the MuID plane containing the two-packs being evaluated. This process is repeated for each plane of the MuID and the efficiencies are averaged over consecutive channels of the same HV segment. This efficiency distribution is shown in Figure 4.23. The status of each MuTr HV channel was recorded throughout the run. If a HV channel tripped or was disabled, the region containing the anode wires serviced by that HV channel is completely dead. These regions shown in Figure 4.23 are masked during the simulation to prevent a simulated response in the corresponding cathode strips.

The limited statistics prevent a kinematic dependent correction to the J/ψ yield. The correction to the production integrated over rapidity and p_T will therefore be dependent on the distribution of the simulated J/ψ signal. The parameterized kinematic distributions used in this analysis is shown in Figure 4.24. The Acceptance $\times$ Efficiency is arbitrarily separated into two factors, $Acc_{geo} \times Eff_{resp+rec}$. The first is determined by an angular cut on the daughter muons between 12 and 45 degrees relative to the beam axis and a minimum momentum cut of $1\mathrm{GeV}/c$. This includes 4.7% of the total rapidity distribution. However, if we only consider J/ψ's within a rapidity window of -1.1 to -2.2 the acceptance is 30.5%. An additional acceptance loss of 54%

110
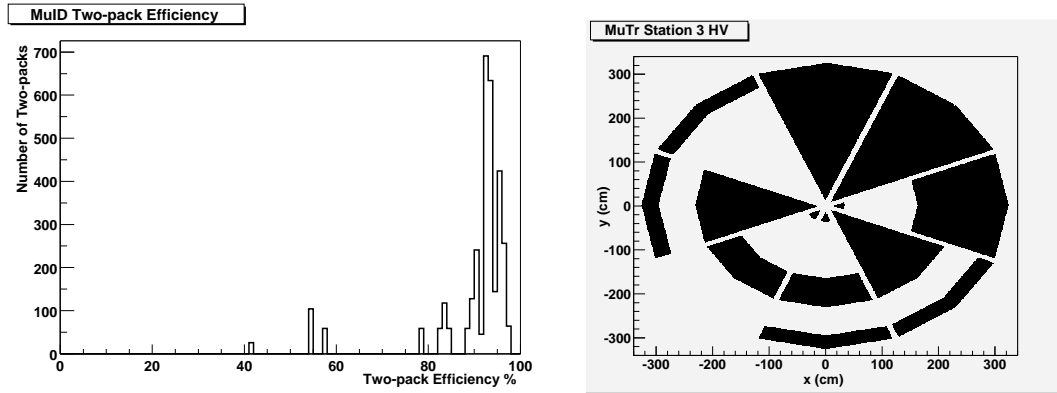
Figure 4.23: MuID channel efficiency distribution and an example MuTr HV mask used to simulate the J/ψ signal. The light regions are the inactive HV channels for Station III gap 1 during run 30916.
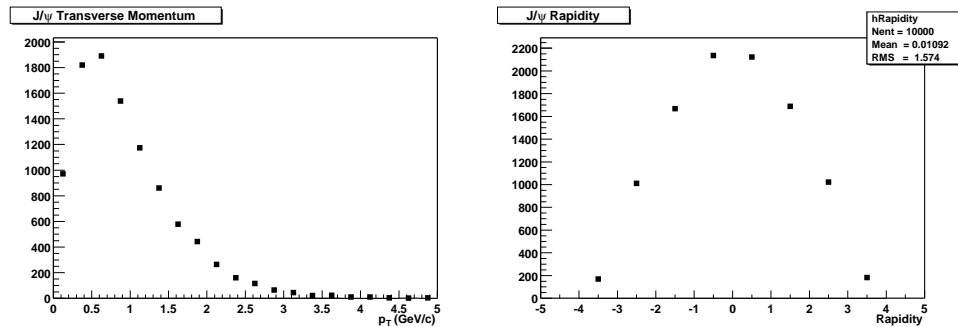
Figure 4.24: The p_T and rapidity distributions of the J/ψ from the PISA internal rv_jpsi event generator used to estimate the spectrometer acceptance and efficiency.

111

results from inactive regions of the detector that are realized in a detailed simulated detector response. For a perfectly performing detector 93% of these J/ψ are successfully reconstructed in both the MuID and MuTr. The detector did not perform perfectly during the run; the dead and inefficient regions resulting from tripped high voltage channels contribute an additional factor of 64% efficiency loss and 77% if track quality cuts are applied, $\chi^2/DOF < 10$ and number of MuTr hits is at least 12. The total acceptance and reconstruction efficiency for the realistic detector is then $0.305 \times 0.46 \times 0.23 \rightarrow 0.032$.

The non-sensitive material in the experimental apparatus must be well described for two reasons. First, all signal particles will suffer energy loss and multiple scattering in the detector material that will blur the precise geometric acceptance. Second, the material of the detector will interact with particles from the collision that are not within the geometric acceptance of the detector. The precise configuration of this material may render it as shielding for detector from such particles or as a source of decay particles that fall into the geometric acceptance. The latter results in a background component that must be disentangled from the signal component. One such contribution to the background is demonstrated in Figure 4.25; the large contribution of hits in the MuID from collision particles with very large pseudo-rapidity indicate that interactions with the RHIC beam pipe within the MuID produces showers of particles transversely into the MuID. Due to the sensitivity of this background component on the precise description of the detector in simulation, the simulation was not used to describe the background component. Since the forward spectrometer is limited by finite segmentation, the ability of the detector to resolve the path of a particle decreases as the number of particles traveling into the detector increases.
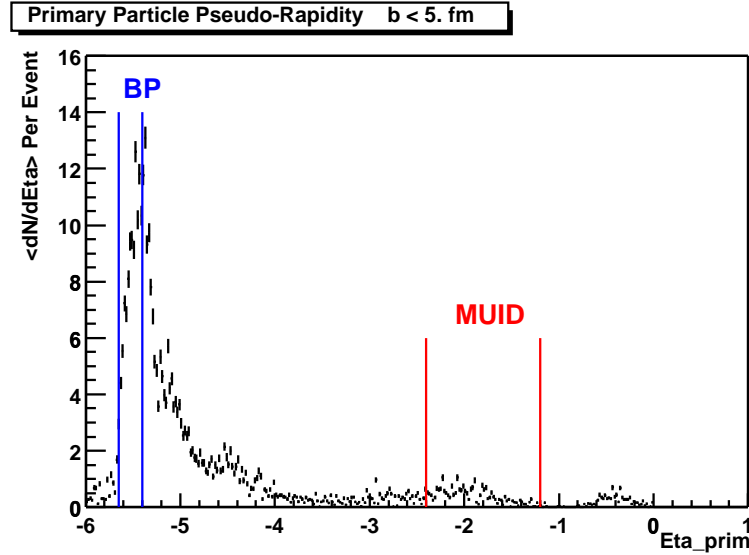
Figure 4.25: Simulated pseudo-rapidity distribution of primary particles from the collision that produce hits in the MuID detector. Vertical lines indicate the location in pseudo-rapidity of the MuID detector and the collider beam pipe.

Therefore, an accurate calculation of the efficiency of the reconstructing a signal requires the presence of a background that is characteristic of a real collision. No better representation can be made than the recorded data itself.

The effect of the background on the signal reconstruction efficiency is estimated by combining the simulated signal with the recorded data of a Au+Au collision. Then the same reconstruction software used to process the real data is applied to this combination of detector signals. The success of the reconstruction is evaluated event-by-event over the recorded centrality distribution. The dependance of the acceptance and efficiency, $Acc_{geo} \times Eff_{resp+rec}$, on the centrality of the collision for one set of quality cuts is shown in Figure 4.26 and Table 4.3. It shows a smoothly increasing efficiency loss with more central (higher occupancy) events.
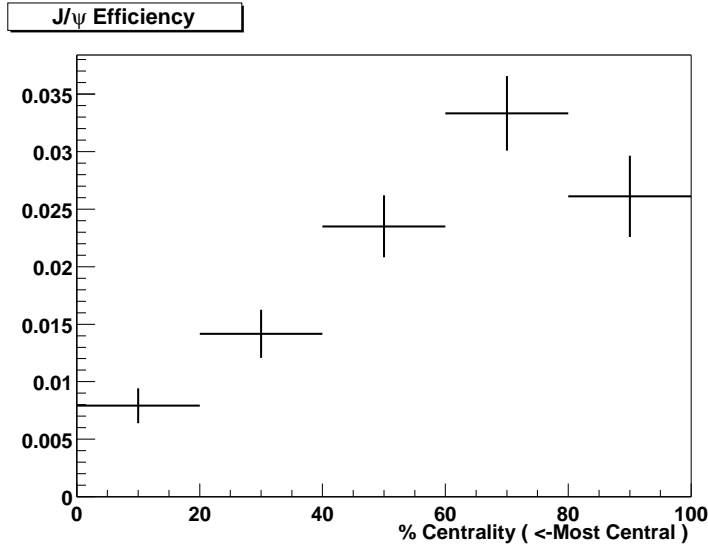
Figure 4.26: The centrality dependance of the Acceptance×Efficiency of J/ψ's with rapidity $-2.2 < y < -1.1$ into the south spectrometer. Efficiency is calculated by embedding simulated decay muons into a real Au+Au collision.

Table 4.3: South Arm Acceptance×Efficiency estimated by simulating the MuTr high-voltage conditions of run 30916 and embedded in recorded events of appropriate centrality. Recorded events outside the vertex range ($-20 < Z_{vertex} < 40$cm) were excluded from the embedding.

% Centrality	$Acc_{geo} \times Eff_{resp+rec}$	Statistical Uncertainty
0-20	0.008	25.0%
20-40	0.016	17.0%
40-90	0.027	8.9%

4.7 Signal/Background Optimization

The J/ψ efficiency calculation previously discussed may be used to estimate the expected number of counts in the data set by extrapolating the "normal" nuclear production and suppression measured at lower energies to be discussed later in Section 5.2.2. Given the detector performance we expect only tens of counts to be successfully reconstructed depending on the quality cuts used. In this section, the available data quality cuts are explored to determine the set of cuts that should produce the most statistically significant result.

4.7.1 Dimuon Open-Angle

The polarization of the J/ψ decay determines in part the separation of the decay muons in the lab-frame. If the decay is precisely along the direction of the J/ψ lab momentum, the backward muon will exactly trail the forward muon until separated by interactions in the absorber and the Muon Magnetic field. However, within the South Muon Arm acceptance this represents a very small phase space. The angles subtended by the muon pair at the origin (open-angle) are shown in left panel of Figure 4.27 in a simulation of the South Arm acceptance. Requiring a minimum open-angle of 20 degrees should then introduce very little bias beyond the detector acceptance itself. Some background reduction could be gained by requiring larger opening angle as shown in the right panel of Figure 4.27. A 30 degree open-angle cut would result in less than a 10% acceptance loss, but the introduction of this additional bias only provides a background reduction of 22%. Unless otherwise stated all dimuon candidates will require a 20 degree open-angle.
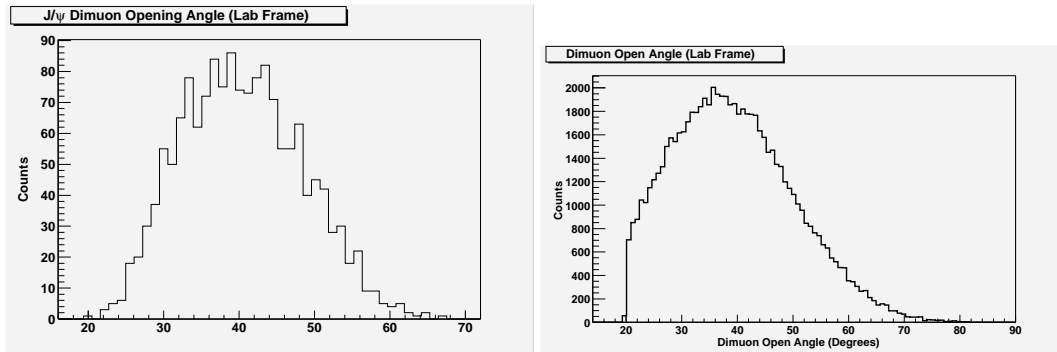
Figure 4.27: The angle subtended in the laboratory frame (open-angle) by candidate dimuons within the invariant mass region $2.8 < M_{\mu\mu} < 3.4$ GeV/c^2 for simulation (left) and real data (right). A 20 degree minimum cut has already been placed on the data shown.

4.7.2 MuID Depth

As previously stated this analysis does not use any explicit muon identification; however, the decay characteristics of the J/ψ allow the MuID depth information to provide significant background reduction. At least one muon originating from J/ψ decays will penetrate to deepest MuID plane for more than 99% of J/ψ's within the MuID acceptance. Requiring that both decay muons penetrate the entire detector gives an acceptance loss of about 18%. Figure 4.28 shows the MuID depth distribution of the least penetrating muon of the J/ψ decay pair.

4.7.3 Track Fit Quality

The statistical summary of each track's quality is its reduced χ^2. A particle's track-hit residuals are normalized by the resolution of the hit position measurement such that the quantity is unitless. The sum is then normalized by the statistical degrees of freedom. For simulated tracks this value peaks sharply near 1 as one might expect, but the recorded data are shifted with mean of

116
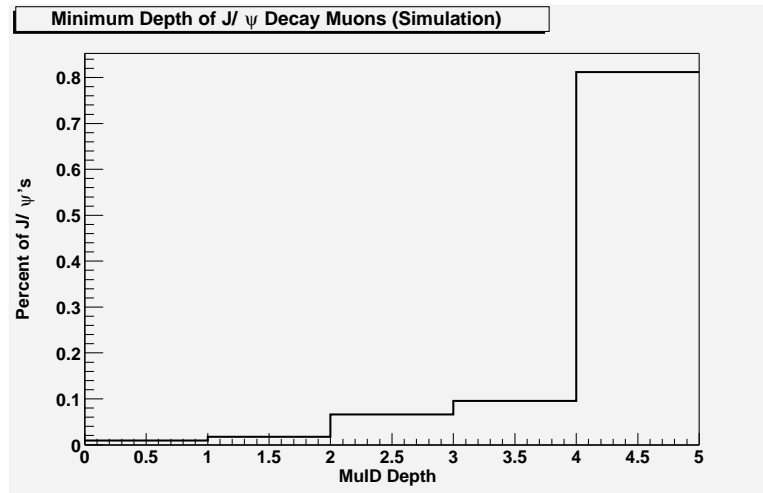
Figure 4.28: The MuID depth of the least penetrating J/ψ decay muon from simulation.

about 5 with some structure retaining perhaps a vestige of the ideal distribution. In Figure 4.29 the reduced χ^2 distribution is shown for the tracks that have hits in all planes of the Muon Tracker in peripheral collisions. The shift is likely caused by the mis-association of hits that are not correlated with the track. A detailed account of the shift has not been fully explored.

4.7.4   Number of MuTr Hits

Ideally, only tracks with associated hits at all 16 planes of the MuTr would be considered. Even if all active areas were 98% efficient, this would represent a track efficiency loss of about 30%. As illustrated earlier there were many inactive regions of the detector during the data collection. Such a stringent requirement would then result in more than a 90% efficiency loss.
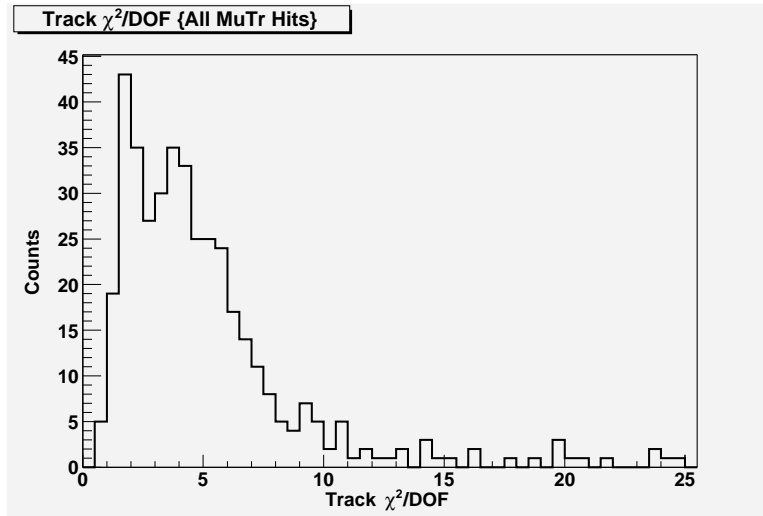
Figure 4.29: The Reduced χ^2 of tracks that have associated hits in all 16 planes of the Muon Tracker.

4.7.5 Quality Cut Summary

By varying these cuts simultaneously the statistical significance may be maximized. A subset of explored parameters is shown in Table 4.4. The reduced χ^2 characterizes the quality of the track fit; the best fit tracks should typically be near 1. The quantity MuID Depth is the required depth on both single tracks. A value of 2 requires both tracks to only penetrate the the third MuID plane; a value of 4 requires full penetration. The minimum number of required hits for any track to be reconstructed in the MuTr is 10; if the chambers were perfectly efficient each track would have 16 associated hits. The effects of these cuts are applied to a simulated signal reconstructed within the background hit occupancy of real data and to the real data dimuon distribution. The Signal is a simple scaling of the simulated yields to match the expectations of the recorded luminosity. The background is the number of like-sign dimuons within the mass

Table 4.4: Optimization of Statistical Significance

Reduced χ^2	MuID Depth	Required MuTr Hits	Simulated Counts	Signal	Background	S/N	Statistical Significance
1000	2	10	560	20.0	36038	0.0006	13.43
10	2	10	491	17.5	1279	0.014	2.89
5	2	10	401	14.3	186	0.077	1.37
1000	2	12	345	12.3	2279	0.0054	5.49
1000	2	15	9	0.3	3	0.11	7.82
1000	2	16	4	0.1	1	0.14	10.25
1000	4	12	298	10.6	925	0.012	4.05
10	4	12	266	9.5	69	0.14	1.28
5	4	12	223	8.0	20	0.40	0.87

region $2.8 < M_{\mu^+\mu^-} < 3.4$ GeV/c^2 after the same cuts are applied. The S/N value is the ratio of the remaining signal to background; the statistical significance is the ratio of the signal to the statistical uncertainty associated with subtracting the background from the hypothetical unlike-sign distribution containing signal and background, $\sigma_S/S = \sqrt{(S + 2N_{background})}/S$; the result is significant when the statistical significance is less than 1. The cut providing the most dramatic reduction in background is the reduced χ^2 improving the S/N by a factor of 23. Tightening the cut on the number of hits dramatically reduces the effective acceptance of the MuTr given the high voltage performance of the run. However, requiring full penetration into the MuID reduces the signal by less than 20% and improves the S/N ratio by more than a factor of 2. The most promising set are the last two entries with statistical significances of 1. While the last candidate is slightly better, it requires a reduced χ^2 cut into a region of the distribution that is not well understood. Therefore, the yield resulting from this analysis will be derived from the previous entry.

4.8 Centrality Dependent Invariant Yield

The centrality dependence of the dimuon invariant mass distributions are used to extract the invariant yield, BdN/dy for three exclusive centrality selections, where B is the $J/\psi \to \mu^+\mu-$ branching ratio.

4.8.1 Signal Counts

The invariant mass spectra discussed in section 4.5 have been divided into three centrality bins shown in Figure 4.30. The most central collisions contain both the largest physics background contributions and the largest potential for random combinatoric background due to the high occupancy. In contrast, the peripheral selection is a much cleaner environment. The like-sign and unlike-sign dimuon candidates within the mass region $2.8 < M_{\mu^+\mu^-} < 3.4 \text{ GeV}/c^2$ are summarized in Table 4.5. The values for all centralities are not inconsistent will a null result. However, the mid-centrality observations do result in a marginal, but positive signal. The significance of these results will be discussed further in the next section.

Table 4.5: The signal and background dimuon counts within the mass region $2.8 < M_{\mu^+\mu^1} < 3.4 \text{ GeV}/c^2$ with standard cuts described in Section 4.7.5.

Centrality	Like-sign Counts	Unlike-sign Counts	Difference
0-20%	58	51	-7
20-40%	20	8	12
40-90%	1	1	0
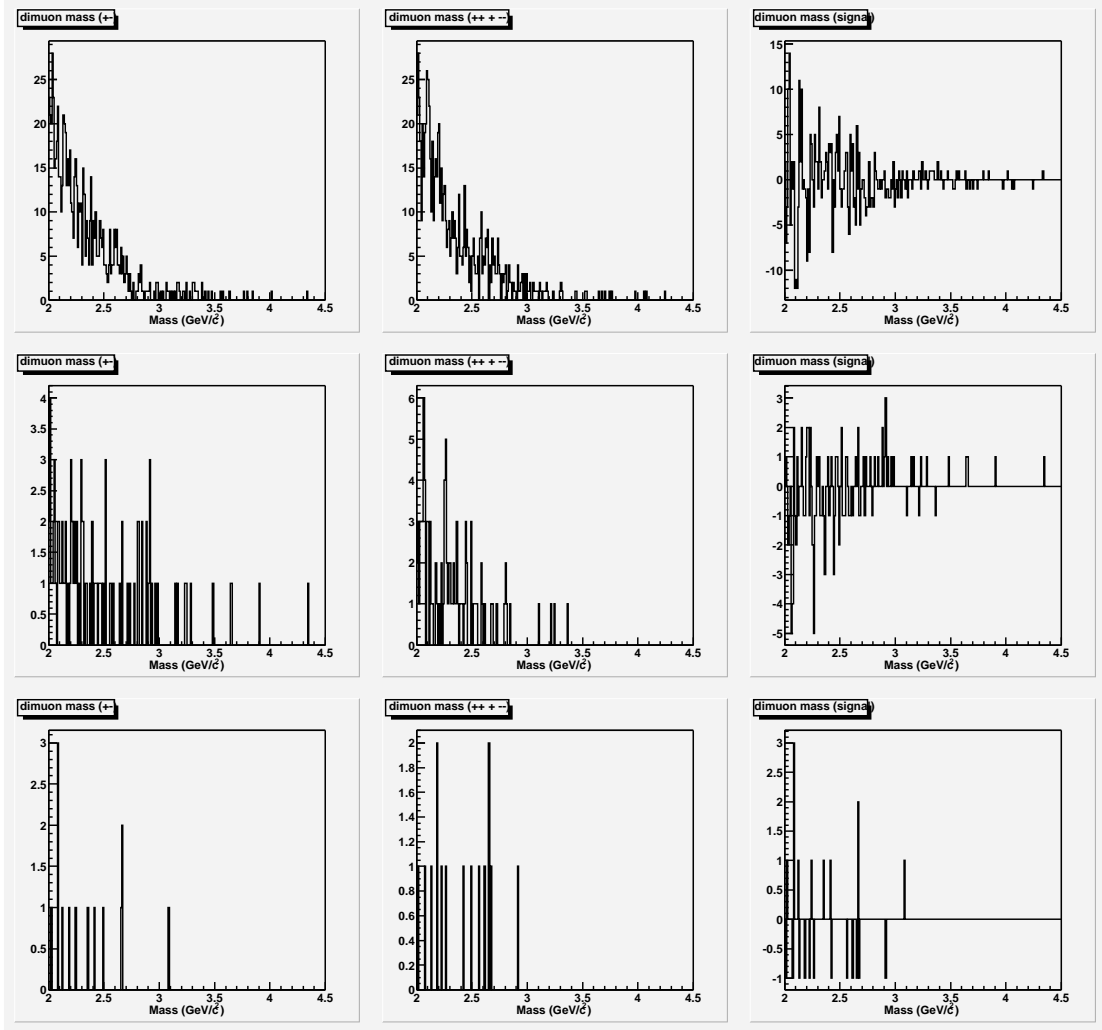
Figure 4.30: Dimuon invariant mass distribution (top row: most central, 0-20%; middle row: mid-central, 20-40%; and bottom row: peripheral, 40-90%) for unlike-sign pairs (left column), like-sign pairs (center column) and the subtracted difference (right column).

4.8.2 Statistical Analysis

We will now examine the statistical significance of the like and unlike sign dimuon yields as a function of centrality. The analysis procedure utilized by the PHENIX collaboration in the dielectron analysis will be followed [1]. The dimuon counts within the mass region, $2.8 < M_{\mu\mu} < 3.4 \text{ GeV}/c^2$, for the like-sign and unlike sign pairs will be considered. Since the sampling of each follows Poisson statistics, the likelihood that given a measurement of the like-sign and unlike-counts, N_u and N_l, was sampled from a distribution with expectation values, ν_u and ν_l is

$$L(\nu_l, \nu_u) = \frac{\nu_l^{N_l} e^{-\nu_l}}{N_l!} \times \frac{\nu_u^{N_u} e^{-\nu_u}}{N_u!} \tag{4.2}$$

It is assumed that the unlike-sign distribution includes both the pairing of uncorrelated single particles and a the pairing of correlated muons of the J/ψ decay; the like-sign distribution contains only the contribution from uncorrelated single particles. The contribution of the correlated signal is then given by $N_s = N_u - N_l$.

By integrating over the $L(\nu_l, \nu_u)$ the likelihood $L(\nu_s)$ is determined where ν_s is the expectation value for the number of signal counts.

$$L(\nu_s) = \int_0^\infty \int_0^\infty L(\nu_l, \nu_u) \delta(\nu_s - \nu_u + \nu_l) d\nu_l d\nu_u \tag{4.3}$$

In this formulation there is a finite probability of extracting a negative signal which would be unphysical. This constraint is imposed by forcing $L(\nu_s)$ to zero for values of ν_s less than zero

and renormalizing the distribution to unity as shown in Figure 4.31. The vertical bar at the most

right marks 90% of the distribution above a zero signal. The most likely value is $12^{+5.22}_{-5.32}$ counts.

Values for all centralities are tabulated in Table 4.6

These results are presented as the decay branching ratio of $J/\psi \to \mu^+\mu^-$ times the invariant

yield; N_{mb-evt} is the number of events included in the analysis.

$$B \times \frac{dN}{dy}|_{-2.2<y<-1.1} = \frac{N_{J/\psi}}{N_{mb-evt}} \times \frac{1}{\triangle y} \times \frac{1}{Acc_{geo} \times Eff_{resp+rec}} \tag{4.4}$$

A non-zero signal count was only measured for the mid-centrality event class and a most-

likely invariant yield can be calculated. For all centrality classes a 90% confidence level upper

limit is calculated in Table 4.7.
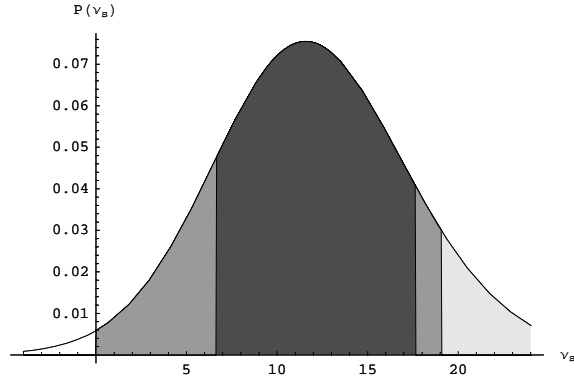
Figure 4.31: The likelihood of extracting a signal, ν_s, in the case of an unlike sign sampling of 20 and and a like-sign sampling of 8. The right vertical line is the extracted 90% confidence level and the two vertical lines left and right of 12 marks the 34% confidence above and below the most-likely value.

Table 4.6: Statistical results for observed J/ψ counts using a log-likelihood analysis for three exclusive centrality selections. Shown are the most likely signal values and the 90% confidence level upper limits.

% Centrality	Events	Like-sign	Unlike-sign	Most Likely	90% C.L.U.L.
0 - 20	1198160	58	51	0	13.6
20 - 40	1241160	8	20	$12^{+5.7}_{-5.4}$	19.1
40 - 90	3085660	1	1	0	3.3

Table 4.7: Invariant yields at forward rapidity calculated for the most likely value and 90% confidence levels.

% Centrality	N_{part}	N_{coll}	BdN/dy per binary collision ($\times 10^{-6}$)	
			Most Likely Value	90% C.L.U.L.
0 - 20	280 ± 4	779 ± 75	N.A.	1.65
20 - 40	140 ± 5	296 ± 318	1.73	2.84
40 - 90	34 ± 3	45 ± 7	N.A.	0.795

4.9 Systematic Errors

The primary systematic uncertainty associated with the invariant yield calculation is the detector acceptance and efficiency, $Acc_{geo} \times Eff_{resp+rec}$ which is calculated for each centrality class as described previously. Several contributions to this systematic error will be considered.

- The p_T dependence of the efficiency is illustrated in Figure 4.32. The systematic uncertainty due to the p_T dependence is estimated by comparing the $Acc_{geo} \times Eff_{resp+rec}$ averaged over $0.0 < p_T < 4.0$ when applied to the distribution of shown in Figure 4.24 and when applied to a uniform distribution. The difference of the average $Acc_{geo} \times Eff_{resp+rec}$ is 9.1%.

- Similarly, the choice of rapidity distribution of the simulation contributes some uncertainty. This was evaluated in the proton+proton J/ψ analysis and found to contribute less than 3%. The detector occupancies of proton+proton environment are much less than Au+Au. Therefore, any convolution of an occupancy-dependent efficiency varying with rapidity would not be included.

- The efficiency loss in the most central bin reduced dramatically the statistics of the simulation used to determine the efficiency. For this centrality the statistical uncertainty of the extracted $Acc_{geo} \times Eff_{resp+rec}$ is 25%. The calculation was compared with two other running conditions and found to be within this statistical uncertainty.

- Run-by-run efficiency differences introduce a systematic error; the efficiency correction $Acc_{geo} \times Eff_{resp+rec}$ is not made for each MuTr HV configuration and background
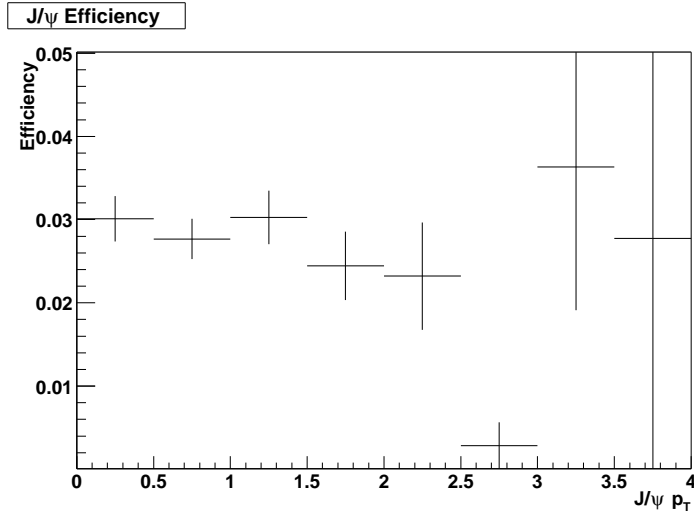
Figure 4.32: The simulated p_T dependence of J/ψ acceptance and efficiency not including mixed background.

conditions associated with each run. Similar detector performance and variations were seen during the proton+proton run which immediately followed the Au+Au run. This effect was evaluated in the J/ψ analysis of the proton+proton data and found to contribute 5% to the systematic error[17].

The systematic uncertainty of the invariant yield is dominated by the acceptance×efficiency correction and a cross-check is performed. The total J/ψ acceptance and efficiency calculated in the PHENIX proton+proton analysis is $Acc_{geo} \times Eff_{resp+rec} = 0.035 \pm 0.03\%(stat) \pm 0.13(sys)$. The proton+proton run immediately followed the Au+Au run and the performance of the PHENIX forward spectrometer was very similar. The peripheral Au+Au collisions have the lowest detector occupancy and provide the most useful comparison to the proton+proton result. The value derived in this work for peripheral Au+Au collisions ($0.027\pm8.9\%$) is consistent

126

with the published proton+proton analysis within the stated errors. The subsequent degradation of efficiency at higher occupancies (more central collisions) is expected and observed to be a smooth transition. A high statistics simulation could reduce the statistical uncertainty of this measurement, but the statistical limitations of the data on which the corrections are being applied do not warrant what would be at most a factor of 2 reduction in the overall systematic error. The estimated systematic errors are summarized in Table 4.8

Table 4.8: Summary of systematic errors considered for the acceptance and efficiency correction to the observed dimuon yields.

Source	Systematic Uncertainty
p_T Dependence	9.1%
Rapidity Dependence	3%
Simulated Statistical	25%
Run-by-run Variations	5%
Total (Quadrature Sum)	27%

Chapter 5

Experimental Results, Model

Comparisons, and Discussion

In the preceeding analysis we have examined 5.5 million Au+Au reactions at $\sqrt{s_{NN}} = 200\,\mathrm{GeV}$ selected with a minimum bias trigger representing 90% of the Au+Au cross section. The data recorded by the PHENIX forward spectrometer were used to reconstruct the momentum and trajectory of particles from the collisions. The invariant mass spectra were made by combining particles of like-sign charge and unlike-sign charge. The like-sign spectra (uncorrelated) were subtracted from the unlike-sign (correlated+uncorrelated) spectra, but no statistically significant J/ψ signal was found. However, the 90% confidence level upper limits set by the measured yields have been extracted for three exclusive centrality selections. Systematic corrections have been applied to these values to derive an invariant yield for these centrality classes. The BdN/dy values of the J/ψ in Au+Au reactions at $\sqrt{s_{NN}} = 200$ GeV from this analysis

are presented in Figure 5.1 for three exclusive centrality selections. These are measured within a rapidity range $-2.2 < y < -1.1$ via the $\mu^+\mu^-$ (dimuon) decay channel. Also shown is the proton+proton measurement at the same collision energy and rapidity [17]. The grey band outlines the invariant yield assuming binary scaling of the proton+proton measurement. The measurements made in Au+Au reactions are compatible with any prediction that would be comparable to or below binary scaling. Before this result and other recent measurements by the PHENIX experiment are discussed further, several theoretical predictions for RHIC will be surveyed.

5.1   Previous PHENIX Measurements

5.1.1 J/ψ Production in proton+proton reactions at $\sqrt{S_{NN}} = 200$ GeV

Immediately following the Au+Au run examined in this analysis, PHENIX recorded proton+proton reactions at $\sqrt{S_{NN}} = 200$ GeV. J/ψ production was measured at both mid-rapidity within the PHENIX central arms and at forward rapidity within the PHENIX forward spectrometers. The J/ψ was observed at mid-rapidity via the dielectron decay channel and at forward rapidity via the dimuon decay channel. This measurement of J/ψ production is important for several reasons.

First, the successful reconstruction of the J/ψ peak shown in Figure 5.2 represents an important milestone in the commissioning of the PHENIX forward spectrometer. In spite of a challenges presented by less than optimal detector performance, the efforts of many years of design and construction were realized.

Second, J/ψ hadroproduction mechanisms can only be understood by examining data over
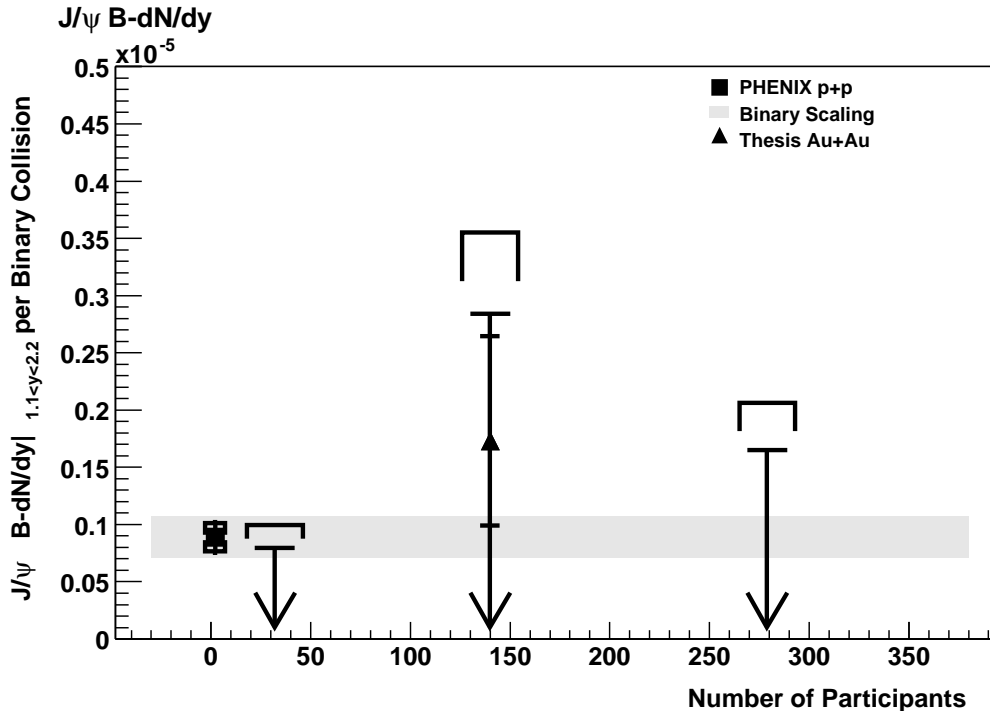
Figure 5.1: The J/ψ invariant yield per binary collision is shown for proton+proton reactions and three exclusive centrality ranges of Au+Au reactions at $\sqrt{s_{NN}} = 200$ GeV. The most likely value for the proton+proton measurement is shown with statistical errors and bracketed by the systematic error. For the three Au+Au measurements, 90% confidence level upper limits are shown bracketed above by the estimated systematic uncertainty. The most likely value is shown for mid-centrality, marked above and below by the 68% confidence limits. The grey band indicates the scaling of the proton+proton measurement with the number of binary collisions and the width is the quadrature sum of the systematic and statistical uncertainties. The systematic uncertainty in the invariant yield per binary collision does not include the systematic uncertainty of the expected number of binary collisions.
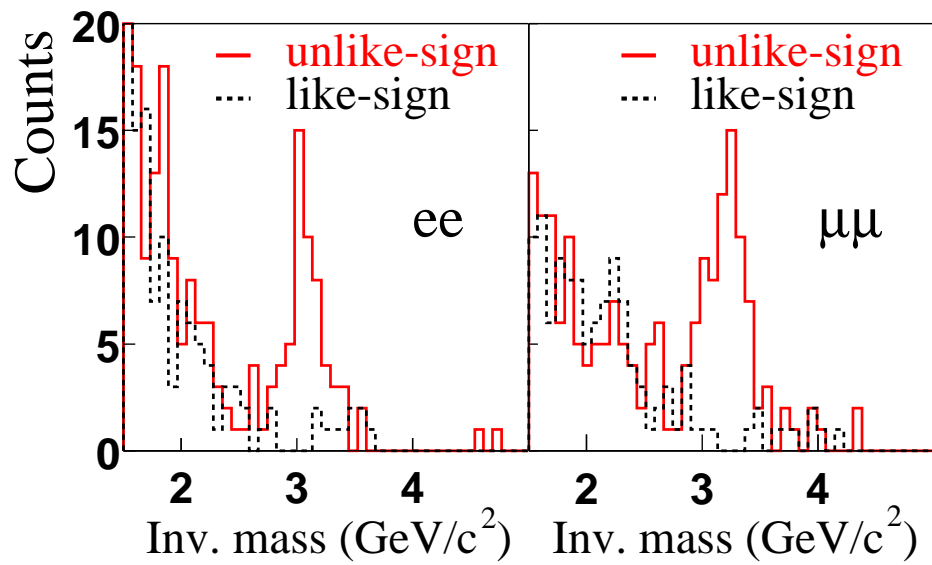
Figure 5.2: The invariant mass spectra for dielectron and dimuon pairs in proton+proton collisions at $\sqrt{s_{NN}} = 200$ GeV [17]. Unlike-sign pairs are shown as solid lines, the sum of like-sign pairs as dashed lines.

a large range of collision energies, rapidity coverage, and transverse momentum. Theoretical interest was rekindled when the color singlet model dramatically under-predicted the CDF high p_T prompt J/ψ cross sections. Two models are able to successfully describe the excess over the color singlet model by including the contributions of color octet production processes, the color octet model (COM) based on the NrQCD framework and the phenomenological color evaporation model (CEM). This measurement can explore production within the energy gap of fixed target energies and high-energy colliders. In fact, the PHENIX J/ψ result for proton+proton collisions provides the first measurement of $< p_T >$ above $\sqrt{s} = 63$ GeV [17].

Third, the search for the quark gluon plasma in the heavy-ion physics program requires a baseline measurements in proton+proton reactions and proton-nucleus reactions.

The J/ψ transverse momenta spectra have been measured [17] and are shown in Figure 5.3. The predictions of the color singlet model, shown for both central and forward rapidities, consistently under-predict the measurements. Also shown are the predictions of the COM which are compatible with the measured spectra [18]. The latter calculations are only valid between p_T of 2 GeV/c and 5 GeV/c. Below this range, the intrinsic transverse momentum, k_T, of the partons is not properly accounted. Within this range the gluon fusion production process dominates; however, for $p_T > 5$GeV the fragmentation of gluons is shown to be the dominant production process. The latter contribution has not been included in the calculation. With the increased statistics of future runs at RHIC the measured p_T will be extended and calculations covering the full p_T range will be needed.

The wide kinematic coverage obtained by combining the acceptance of the PHENIX central
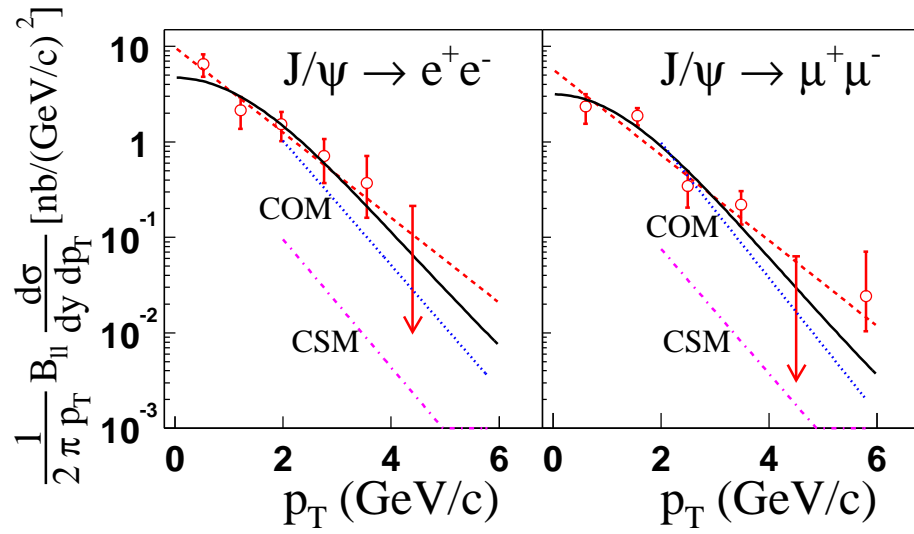
Figure 5.3: The J/ψ p_T distributions for the dielectron and dimuon measurements in proton+proton collisions at $\sqrt{s_{NN}} = 200$ GeV with statistical uncertainties[17]. The solid line is a phenomenological fit of the form $1/(2\pi p_T)\ d\sigma/\sigma p_T = A(1 + (p_T/B)^2)^{-6}$. The dashed line is an exponential fit. The CSM (dot-dashed) and COM (dotted) calculations are from [18].

arm and the acceptance of the PHENIX forward spectrometer removes the ambiguity present in many high energy collider experiments by extrapolating into kinematic regions beyond their acceptance. The importance of this is demonstrated in the variation of calculations in Figure 5.4. Shown are the central arm measurement at mid-rapidity and the muon arm measurements divided in two rapidity bins. There are two COM calculations using different parton distribution functions. Since the integrated yield is dominated by the gluon fusion process, the shape of the calculated distribution is very sensitive to the choice of PDF. While one may be favored slightly over the other, a measurement with greater statistical precision is required to constrain them.

The total J/ψ production may be determined by integrating the PYTHIA calculation which reproduces the shape of the data best. The PHENIX measurement is compared to measurements at lower energies in Figure 5.5. Also shown are the COM calculations for two different parton distribution functions. Both are consistent with the measurement once the factorization scale is optimized to give the best agreement with the data. The color evaporation model (CEM) provides similar agreement with the measurement. Unfortunately, the recorded data did not provide sufficient statistics for a J/ψ polarization measurement. The different predictions of the COM and CEM for this observable discussed in section 2.3 are an important test of these models. Future measurements planned at RHIC with increased luminosity and over an energy range of $\sqrt{s} = 200$ GeV to 500 GeV will make this measurement possible.
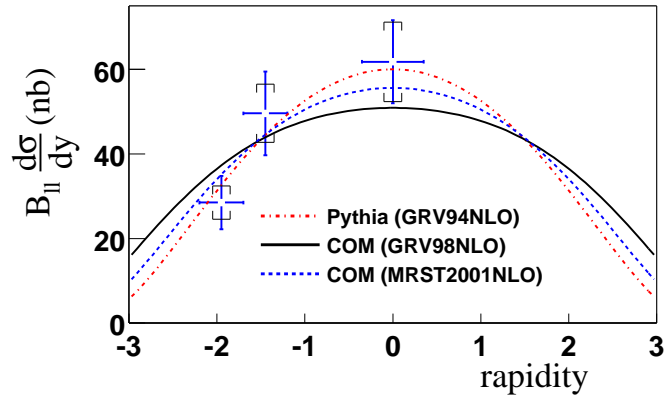
Figure 5.4: The PHENIX measurement of J/ψ production in proton+proton collisions at $\sqrt{s_{NN}} = 200$ GeV [17]. The central rapidity point is from $J/\psi \to e^+e^-$ and forward rapidities are from $J/\psi \to \mu^+\mu^-$. The brackets represent systematic uncertainties. The overall normalization of all curves is determined from a fit to the data. The PYTHIA shape was used to determine the cross section. There is an overall 10% absolute normalization not shown.
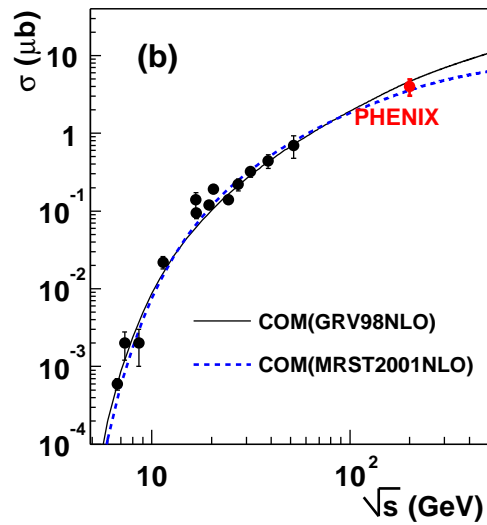
Figure 5.5: The measured J/ψ total cross section compared with previous measurements at lower energies. The curves are predictions of the COM using two different parton distribution functions. [17]

5.1.2 Open Charm Production

During RHIC's first year of running collisions of Au nuclei were made at $\sqrt{s_{NN}} = 130$ GeV. The PHENIX detectors located at central rapidity were commissioned during this period. The electron transverse momentum spectrum was measured using the PHENIX west-arm spectrometer and published for $p_T > 1$ GeV/c [19]. The relevance of this measurement to J/ψ production and the search for the QGP is in the extraction of the total charm production. As previously discussed, Drell-Yan production is no longer the viable baseline for J/ψ suppression that it was for lower energies; measurements of the total charm production must provide this baseline.

Four sources of background are evaluated that contribute to the single electron spectra: Dalitz decays of π^0, η, η', ω, and ϕ; dielectron decays of ρ, ω, and ϕ; photon conversions; and kaon decays ($K^{0,\pm} \rightarrow \pi e \nu$). All of these sources are considered background; their contributions are estimated from a detailed GEANT simulation. Also contributing to the spectrum are the electrons from semi-leptonic decays of charm; this is the signal of interest. The calculated background spectra are subtracted from the measured spectra resulting in the distributions of Figure 5.6. Remaining sources are considered; expected J/ψ and Drell-Yan are negligible. Bottom decays are expected to only be significant beyond the measured p_T range. It is possible that conversions of direct photons could contribute 10-20% of the spectrum, but there are large theoretical uncertainties.

Assuming that all of the electron signal of Figure 5.6 is from charm, an electron PYTHIA calculation of charm is fit to the data allowing the extraction of the rapidity density, $dN_{cc}/dy|_{y=0}$, and the total yield of charm, N_{cc}. The cross section per binary collision is derived from
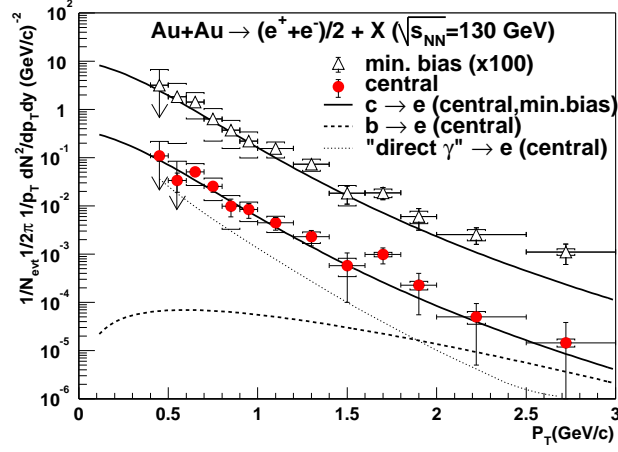
Figure 5.6: Single electron p_T spectra at mid rapidity in central and peripheral Au+Au events at $\sqrt{s_{NN}} = 130$ GeV [19].

$d\sigma_{c\bar{c}}/dy = (dN_{cc}/dy)/T_{AA}$ where T_{AA} is the integrated nuclear overlap function. These values are tabulated for the 10% most central collisions and for the minimum bias data set in Table 5.1. The number of $c\bar{c}$ pairs per binary collision is observed to be independent of centrality within the experimental uncertainties; there does not appear to be a large charm enhancement due to any nuclear or medium effects.

The total charm production measured by PHENIX at $\sqrt{s_{NN}} = 130$ GeV is compared to measurements at lower energies in Figure 5.7. A PYTHIA calculation has been tuned to fit both the PHENIX data and the data from lower energies. It is worth noting the implication of multiple charm pairs per central (0-20%) Au+Au collisions and perhaps a factor of two greater at $\sqrt{s_{NN}} = 200$ GeV. For the most central 5% collisions, calculations indicate a value of 10 $c\bar{c}$ pairs for collisions with impact parameter, $b = 0$ [54]. Confirmation of this prediction through experimental measurement will be a necessary step in understanding the measured J/ψ yields.

138

Table 5.1: Charm cross section per binary nucleon-nucleon collision derived from the PHENIX single electron data for central (0-10%) and minimum bias (0-92%) collisions. Statistical and systematic uncertainties are included in that order [19].

Centrality	$T_{AA}(mb^{-1})$	$d\sigma_{cc}/dy|_{y=0}(\mu b)$	$\sigma_{c\bar{c}}(\mu b)$
0-10%	$22.6 \pm 1.6(sys.)$	$97 \pm 13 \pm 49$	$380 \pm 60 \pm 200$
0-92%	$6.2 \pm 0.4(sys.)$	$107 \pm 8 \pm 63$	$420 \pm 33 \pm 250$
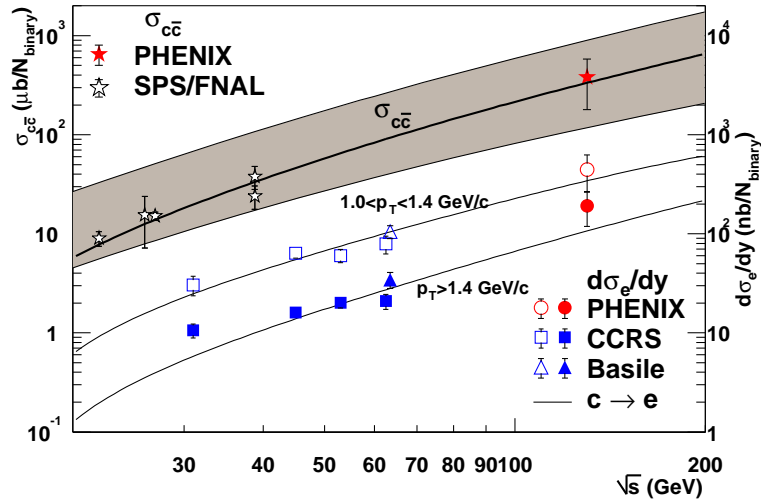
Figure 5.7: Single electron production at RHIC and ISR experiments [19]. Open and closed symbols are for $1.0 < p_T < 1.4$ GeV/c and $p_T > 1.4$ GeV/c respectively (right-hand scale). The left-hand scale indicates the charm contribution derived from PYTHIA.

139

5.1.3 J/ψ **Production in Au+Au at** $\sqrt{s_{NN}} = 200\,\mathrm{GeV}$

In the preceding chapter the data recorded by the PHENIX forward spectrometers were ana-
lyzed. At the same time that these data were collected, the PHENIX central arm recorded J/ψ
decays via the dielectron channel [1]. Figure 5.8 shows the invariant mass spectra for like-sign
pairs, unlike-sign pairs, and like-sign subtracted for three exclusive centrality selections. The
signal counts extracted from the spectra within the J/ψ mass region are shown in Table 5.2
along with the muon results of this thesis. While a larger data sample was analyzed (almost a
factor of 10 more than for the muon analysis), very similar yields to the muon decay channel
were observed due to a much smaller geometric acceptance.

The same centrality selection is used for the electron analysis as was described in the pre-
vious chapter for the muon analysis. The procedure outlined in section 4.8.2 was applied to the
signal counts of the electron spectra between invariant mass $2.8 < M_{\mu\mu} < 3.4\,\mathrm{GeV}/c^2$. Signal
counts of the muon and electron analysis are tabulated in Table 5.2. The Acceptance×Efficiency
correction was made appropriately for the PHENIX central arm acceptance. As in the muon
analysis, a p_T dependent correction could not be applied. However, the central arm accep-
tance has a much stronger p_T dependance than the muon arm. The uncertainty in the true
$< p_T >$ results in the largest source of systematic errors for the Acceptance $\times$ Efficiency,
$\epsilon_{acc-eff} = 0.0027^{+0.0009}_{-0.0005}$.

The measured invariant yields are tabulated in Table 5.3 shown in Figure 5.9 for both mid-
rapidity and forward rapidity (the latter arbitrarily shifted in the plot for clarity). The upper band
is the scaling of the proton+proton J/ψ measurement at central rapidity with the number of bi-
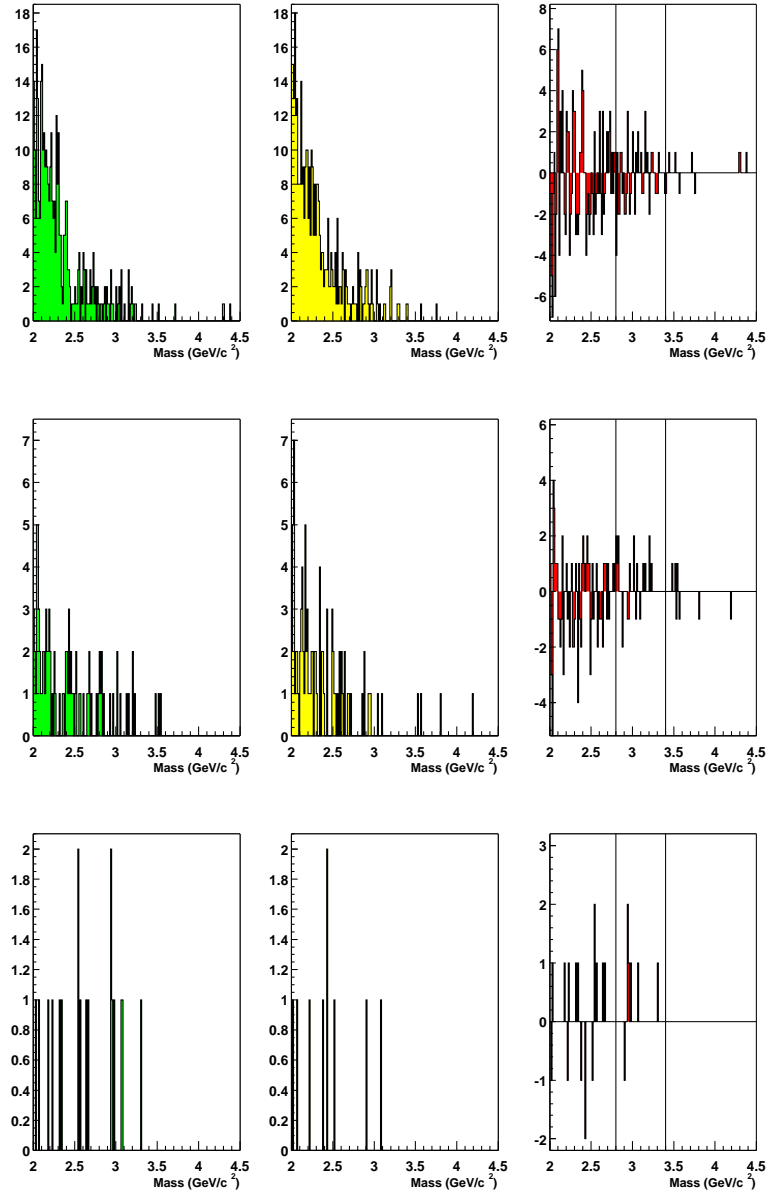
Figure 5.8: Dielectron invariant mass distribution in Au+Au collisions. Shown are (top row: most central, 0-20% central; middle row: mid-central, 20-40% central; and bottom row: peripheral, 40-90% central) for unlike-sign pairs (left column), like-sign pairs (center column) and the subtracted difference (right column)[1].

Table 5.2: The dimuon and the PHENIX dielectron[1] channel J/ψ yields with statistical results of three exclusive centrality selections are shown from the invariant mass window, $2.8 < M_{\mu\mu} < 3.4 \, \mathrm{GeV}/c^2$.

% Centrality	Rapidity	Like-sign	Unlike-sign	Most Likely	90% C.L.U.L.
0 - 20	$-2.2 < y < -1.1$	58	51	0	13.6
20 - 40	$-2.2 < y < -1.1$	8	20	$12^{+5.7}_{-5.4}$	19.1
40 - 90	$-2.2 < y < -1.1$	1	1	0	3.3
0 - 20	$-0.35 < y < 0.35$	41	33	0	9.9
20 - 40	$-0.35 < y < 0.35$	8	16	$8^{+4.8}_{-4.1}$	14.4
40 - 90	$-0.35 < y < 0.35$	2	7	$5^{+3.1}_{-2.6}$	9.3

Table 5.3: Shown are the number of participating nucleons and the number of binary collisions for three exclusive centrality selections[1] of Au+Au reactions. The most likely invariant yields BdN/dy have been divided by the number of binary collisions for the mid-central and peripheral PHENIX measurements and the mid-central measurement of this thesis at forward rapidity. The 90% confidence level upper limits are shown for both rapidity ranges and all centrality selections.

Centrality (% Events)	Rapidity	N_{part}	N_{coll}	BdN/dy per binary collision ($\times 10^{-6}$)	
				Most Likely Value	90% C.L.U.L.
0 - 20	$-2.2 < y < -1.1$	280 ± 4	779 ± 75	N.A.	1.65
20 - 40	$-2.2 < y < -1.1$	140 ± 5	296 ± 318	1.73	2.84
40 - 90	$-2.2 < y < -1.1$	34 ± 3	45 ± 7	N.A.	0.795
0 - 20	$-0.35 < y < 0.35$	280 ± 4	779 ± 75	N.A.	0.78 + 0.20 (sys)
20 - 40	$-0.35 < y < 0.35$	140 ± 5	296 ± 318	$1.35^{+0.79}_{-0.68}(stat)^{+0.46}_{-0.54}$	2.43 + 0.82 (sys)
40 - 90	$-0.35 < y < 0.35$	34 ± 3	45 ± 7	N.A.	3.55 + 1.21 (sys)
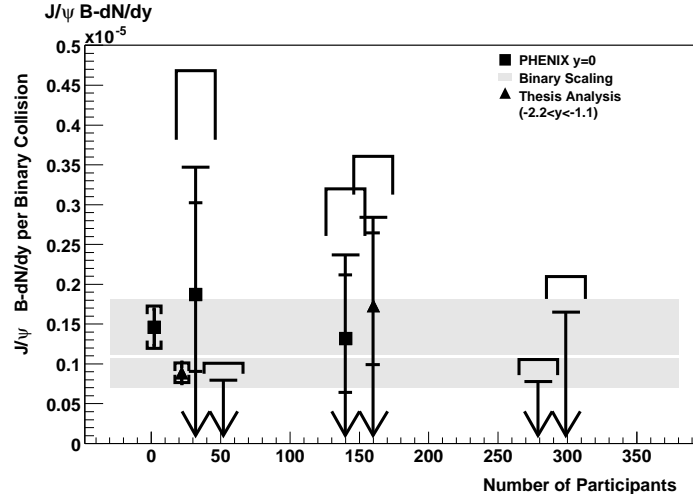
Figure 5.9: The J/ψ invariant yield per binary collision is shown from proton+proton reactions and three exclusive centrality ranges of Au+Au reactions all at $\sqrt{S_{NN}} = 200$ GeV for both mid-rapidity and forward rapidity measurements. (The values of the forward rapidity have been shifted by +20 units along the x-axis for clarity.)

nary collisions. The lower band is the same for the forward rapidity measurement. For the most

central measurements, only the 90% confidence level upper limits are available; the forward

rapidity measurement is consistent with scaling with the number of binary nucleon-nucleon col-

lisions. However, the central rapidity measurement marginally disfavors binary scaling. While

there is a dramatic difference between the upper limits of the most peripheral centrality selec-

tion, they are both consistent with the corresponding proton+proton measurements.

5.2 Model Comparisons for PHENIX Au+Au Measurement

We will now examine several theoretical and phenomenological calculations that have impor-

tant implications for understanding J/ψ production. Both current and future measurements

in nucleus-nucleus collisions at RHIC energies are best explored with measurements over the full kinematic range available to PHENIX. The nuclear parton distributions are predicted to be quite different from the bare nucleon (proton) distributions. The effect of this nuclear shadowing would modify rapidity distributions of J/ψ production in the primordial nucleon-nucleon collisions. The break-up of the J/ψ with interactions with the original nucleons, "normal" suppression, is expected to remain relevant at RHIC energies. If a quark gluon plasma is formed in the collisions, most if not all of the $c\bar{c}$ forming J/ψ's may be dissociated. In a QGP all $c\bar{c}$ pairs would be dissociated from their original partners. However, if sufficient numbers of $c\bar{c}$ pairs are formed in the central Au+Au collisions, the c and $\bar{c}$ pair created in separate initial collisions may find one another in a completely new, and unexplored production process of bound charm.

5.2.1 Nuclear Shadowing

The nuclear modifications at high energies predicted by gluon saturation and the color glass condensate have been quantitatively studied in the light-cone dipole approach [20]. In the infinite momentum frame of the projectile, the effect is that at small values of the fractional momentum, x, the parton densities are suppressed in large target nuclei compared to smaller target nuclei (CGC). Evaluated in the target nucleus frame the effect results from coherent production by multiple nucleons in competition. This nuclear shadowing is predicted to be a large effect at and above RHIC energies. In Figure 5.10 there is a strong x dependence of the gluon density in a Au nucleus relative to the näive scaling of the proton. Furthermore, a much larger suppression is predicted for the singlet process than for octet processes; the suppression of the parton dis-
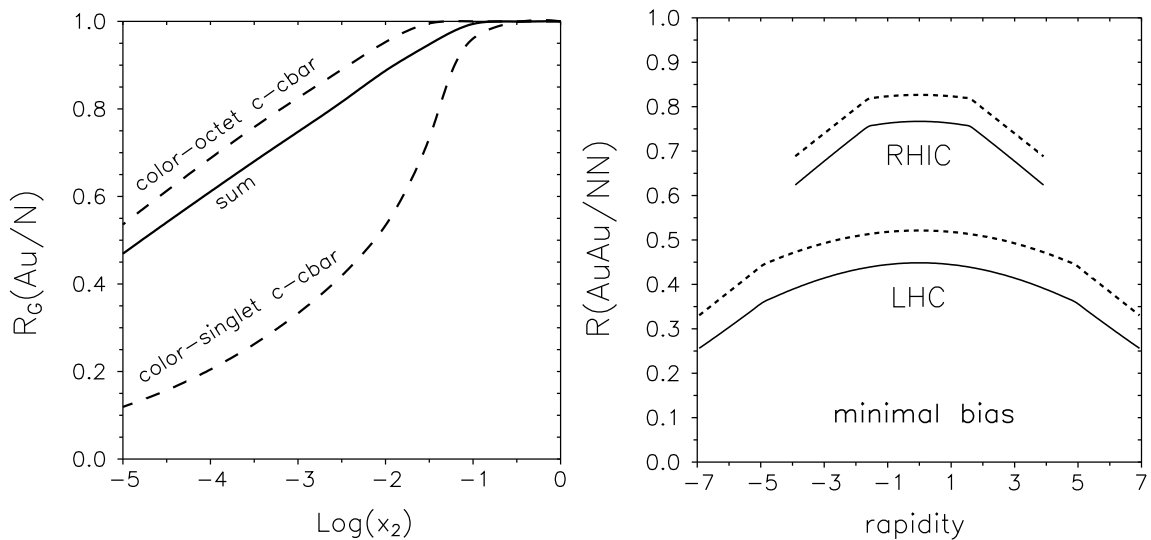
Figure 5.10: Nuclear shadowing evaluated evaluated in the light-cone dipole approach predicts process dependent shadowing (left) and an increase in shadowing at RHIC energies and above (right) [20].

tribution will affect the distribution of produced J/ψ's. These are significant for measurements in PHENIX which has a large coverage in rapidity. The combined measurements of muon arm and central arm will enable PHENIX to be sensitive to the shape shown in the right panel of Figure 5.10. While other effects might also affect this shape, any possible QGP effects can be separated from conventional affects by a comparison with the same measurement in a proton+Au (deuteron+Au) collisions by PHENIX at the same energy. The data from such a run has already been collected and is being analyzed.

145

5.2.2 Normal Nuclear Absorption

Normal nuclear absorption discussed in section 2.4.1 is expected to remain relevant at RHIC energies. The total number of expected J/ψ's from the Au+Au muon dataset may be estimated assuming only "normal" nuclear absorption using the following equation.

$$N_{J/\psi} = \sigma_{Au+Au \to J/\psi} \times \mathcal{L} \times A_{Geometric} \times \epsilon_{HW+Rec} \times B_{J/\psi \to \mu^+\mu^-} \qquad (5.1)$$

The cross section for of Au+Au minimum bias collision forming a J/ψ is calculated by scaling production in proton+proton collisions, $\sigma_{Au+Au \to J/\psi} = A^{2\alpha}\sigma_{p+p \to J/\psi}$, where A is the number of nucleons in the Au nucleus (197) and α is experimentally measured (0.92). The J/ψ production cross section in proton+proton collisions is measured to be 3.99 μb [17]. Based on Figure 4.26 we may estimate the total acceptance and reconstruction efficiency, $A_{Geometric} \times \epsilon_{HW+Rec} \approx 0.003$. The PDG branching ratio, $B_{J/\psi \to \mu^+\mu^-} = 0.06$, is used to obtain $N_{J/\psi} = 10$. This result is consistent with the measured yield of $5 + 17(90\% C.L.U.L.)$ within the statistical uncertainty. It is worth noting that a much larger yield might have been observed had the detector and collider machine had operated more efficiently as outlined in section 4.1. If the detector had performed ideally and beam conditions had allowed for all of the sampled data (170 million events) to be analyzed, the "normal" suppression-only calculation would predict approximately 1300 J/ψ's with a 10% statistical uncertainty due to the background subtraction.

The "normal" nuclear absorption is also expected at central rapidity. The expected invariant yield with conventional absorption is shown in Figure 5.11. Two cross sections are considered for the dissociation of the J/ψ in a nucleon reaction. The measurement at central rapidity is
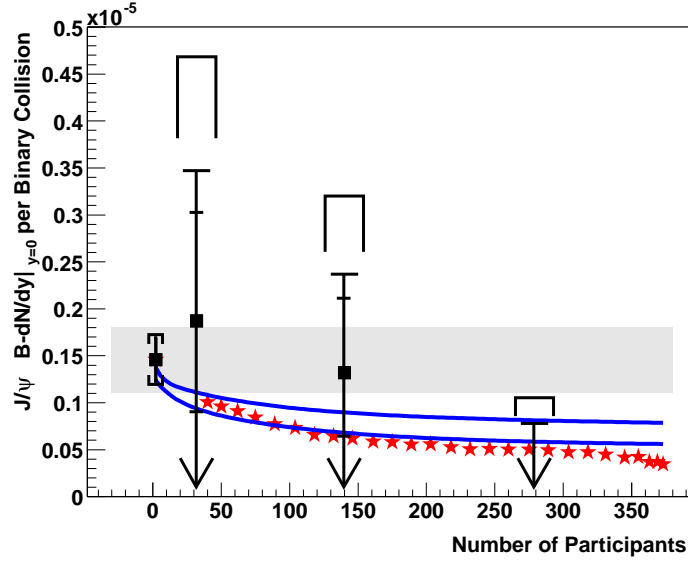
Figure 5.11: The J/ψ invariant yield per binary collision is shown from proton+proton reactions and three exclusive centrality ranges of Au+Au reactions at $\sqrt{S_{NN}} = 200$ GeV. The solid lines are the theoretical expectations from "norma" nuclear absorption with $\sigma_{c\bar{c}-N} = 4.4$mb (upper curve) and 7.1 mb (lower curve) cross section [1]. The stars are the J/ψ per binary collision measured by the NA50 experiment at lower collision energies. The NA50 data have been normalized to match the central value of the PHENIX proton+proton results.

compatible with both a break-up J/ψ cross section of 4.5 mb (upper curve) and of 7.1 mb (lower curve). Also shown is the NA50 measurement; these data were collected at lower energy so they are scaled to match the measured proton+proton yield at $\sqrt{s_{NN}} = 200$ GeV.

5.2.3 Color Screening

In 1986 Matsui and Satz proposed the suppression of the J/ψ to be a valuable probe of QGP formation in high-energy nuclear collisions [41]. The same model of Satz used to describe the SPS Pb+Pb data discussed in section 2.4.3.2 has been applied to RHIC energies. According to his percolation model the onset of color deconfinement will have occurred for even the most
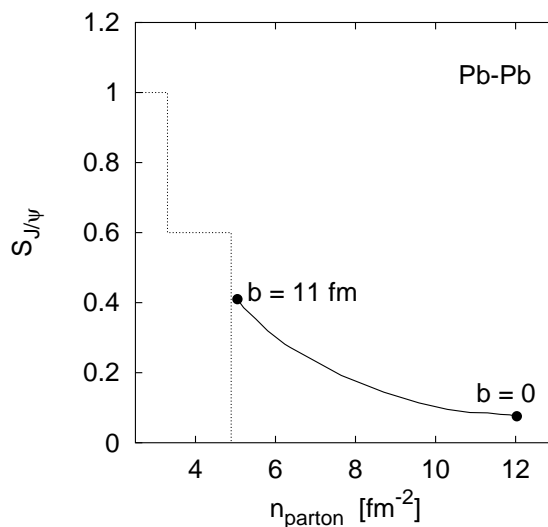
Figure 5.12: The J/ψ survivability as a function of transverse parton density calculated in the parton percolation model of Satz [21]. The dotted curve is the J/ψ survivability assuming uniform parton density over the collision volume. The solid curve includes the correction for variations in the parton density over the collision volume.

peripheral Pb+Pb (or Au+Au) collisions at full RHIC energy. Figure 5.12 demonstrates that

even in the most peripheral collisions, 60% of the initial J/ψ 's will be dissociated in the color

deconfined medium. There is no prediction of a rapid onset of suppression as in SPS Pb+Pb re-

actions, since at RHIC the most peripheral Au+Au collisions are beyond the parton percolation

point. For nucleus-nucleus reactions at RHIC energies, Satz suggests a lighter system such as

Cu+Cu would allow the onset of deconfinement to be explored by its centrality dependence.

Described in section 2.4.3.6 the model of Grandchamp *et al.* [13] utilizes a reduced charmo-

nium binding energy to calculate the J/ψ suppression in a QGP scenario. In Pb+Pb collisions

at the SPS about 40% are lost in the QGP phase. In central collisions at RHIC energies, 80% of

the initial production is estimated to be lost in the de-confined phase. This effect is displayed

in lower curve (solid) of Figure 2.15 for time less than 5 fm/c. There is no prediction of a rapid onset as was predicted by the percolation model at SPS.

5.2.4 J/ψ Enhancement

An extension of the previous model of Grandchamp *et al.* considers the total charm produced in the system [13]. In the most central collisions on the order of 10 $c\bar{c}$ pairs is expected to be produced. A very small fraction of the initially produces $c\bar{c}$ pairs evolve directly into a J/ψ, ~ 0.004. In the QGP the dissociated charm and anti-charm are free to move about the system. As the QGP expands and cools, color confinement will be restored when the system hadronizes. There is a finite probability that a charm will pair with an uncorrelated anti-charm at hadronization. The effect of this additional production mechanism shown in the upper solid curve of Figure 5.13 would compensate entirely for the loss in the QGP phase in the most central collisions. The implication is then that 80% of the observed J/ψ 's will not be from primordial production nor from feed-down from a primordially produced excitations. Instead, the characteristics of this signal will be determined by the thermalized medium.

Two alternate approaches are offered to consider the effects of multiple $c\bar{c}$ pairs. As previously discussed in section 2.4.3.6, neither the previous model nor the following models invoke any charm production beyond that produced in the initial nucleon-nucleon collisions. Nevertheless, all three models predict a total J/ψ production cross section comparable to or greater than that of normal nuclear suppression in spite of the fact that they all also require the formation of the QGP.
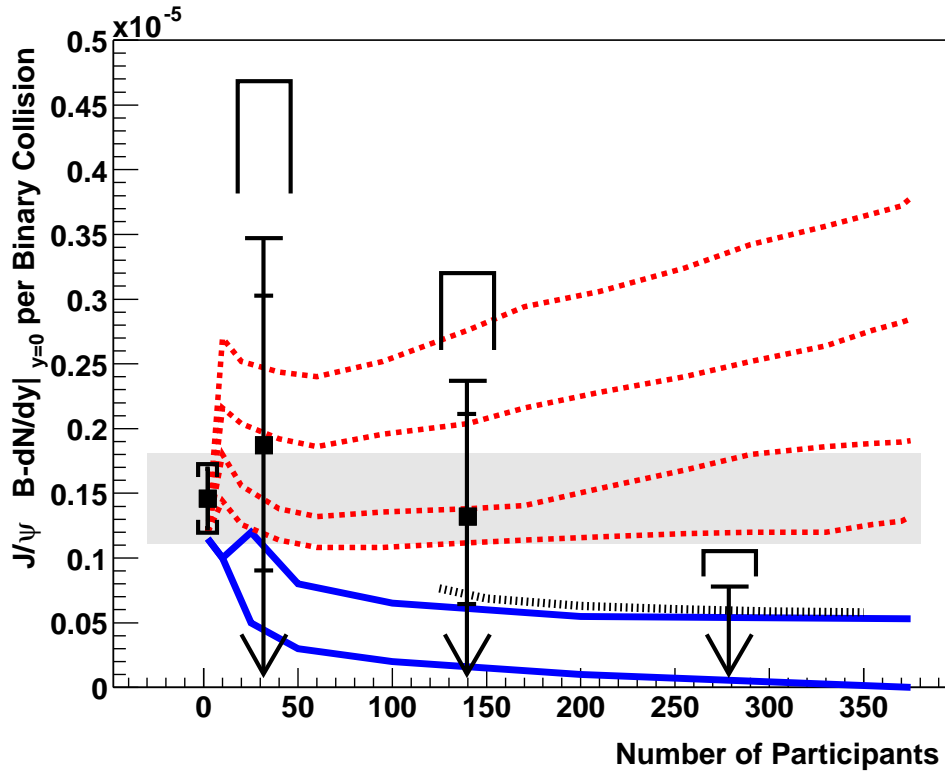
Figure 5.13: The PHENIX measured J/ψ invariant yield per binary collision for proton+proton and Au+Au reactions is compared to several models. The most likely values for central rapidity (squares). The arrows indicate the 90% confidence level upper limits for the Au+Au reactions bracketed above by the corresponding systematic uncertainty. The model predictions are described beginning with the lowest curve: The solid curves include normal absorption combined with a significant QGP suppression (lower) and the coalescence (upper) of uncorrelated charm in an additional component of J/ψ production [13]. The statistical model result is shown as the dotted curve. The four upper curves are the kinetic model for charm rapidity widths of $\Delta y = \{4, 3, 2, 1\}$; the upper most curve is for a charm width of 1 unit rapidity [22].

The statistical model utilizes the framework of canonical thermodynamics to balance the closed charm and open charm populations during hadronization. This balance is quantified by the following equation.

$$N_{c\bar{c}}^{dir} = \frac{1}{2} g_c N_{oc}^{th} \frac{I_1(g_c N_{oc}^{th})}{I_0(g_c N_{oc}^{th})} + g_c^2 N_{c\bar{c}}^{th} \tag{5.2}$$

The number of open charm (N_{oc}^{th}) and hidden charm ($N_{c\bar{c}}^{th}$) are related to the number of initially produced $c\bar{c}$ pairs. I_n are the modified Bessel functions. The initial charm of the system is not in chemical equilibrium; the initial hard production artificially increases the charm multiplicity. The fugacity, g_c, properly accounts for this deviation in the balance equation. The measured charged particle multiplicity is used to extract the volume of the system at the central unit of rapidity. The total initial charm is scaled to the nucleus-nucleus collision from a pQCD calculation of proton+proton collisions. The prediction of this model is shown for intermediate and most central collisions in Figure 5.13; the model is valid only if the volume is sufficiently large, $N_{part} > 100$. The statistical model follows closely the coalescence model of Grandchamp *et al.* and is compatible with the PHENIX measurements.

The kinetic model differs from the previous in that bound charm is not only formed when the QGP hadronizes, but throughout the QGP evolution. The same process that may dissociate the J/ψ $g + J/\psi \rightarrow D + \bar{D}$, should also be properly accounted in reverse. A thermal distribution of the total charm would result in a very narrow rapidity distribution of the charm, $\Delta y = 1$; with this distribution the kinetic production is most effective as demonstrated by upper most curve of Figure 5.13. As the rapidity distribution widens, the effect is less dramatic as demonstrated

by the three curves just below. The predictions of all four choices of rapidity distributions are relevant to the measurement at central rapidity and are disfavored.

The muon data was collected at rapidity of $-2.2 < y < -1.1$; the kinetic model prediction assuming a charm rapidity width of four units is then applicable to the measurement of this thesis. Narrower rapidity distributions would provide dramatically lower yields at forward rapidity. The J/ψ invariant yield measurements of PHENIX and of this thesis are overlaid with the kinetic model prediction $\Delta y = 4$ in Figure 5.14. Factorized QCD and PYTHIA with CTEQ5L structure functions favor this rapidity distribution [19]. While narrow rapidity distributions are more strongly disfavored by the PHENIX central measuremnt, $\Delta y = 4$ is only marginally disfavored. This kinetic model prediction is compatible with the forward rapidity measurement of this thesis.

5.3   Summary

In this chapter, the suite of initial PHENIX J/ψ and charm measurements have been presented. An important goal of these measurements is to address mechanisms for both production and suppression of the J/ψ . The measured electron spectrum at $\sqrt{s_{NN}} = 130$ GeV has provided the only charm measurement near RHIC energies and guided expectations for $\sqrt{s_{NN}} = 200$ GeV. The proton+proton J/ψ production cross section has provided a baseline for the heavy-ion program in both central and forward rapidity. This measurement demonstrates another success in the design, construction, and operation of the PHENIX experiment and a milestone of the debut run of the forward spectrometer.
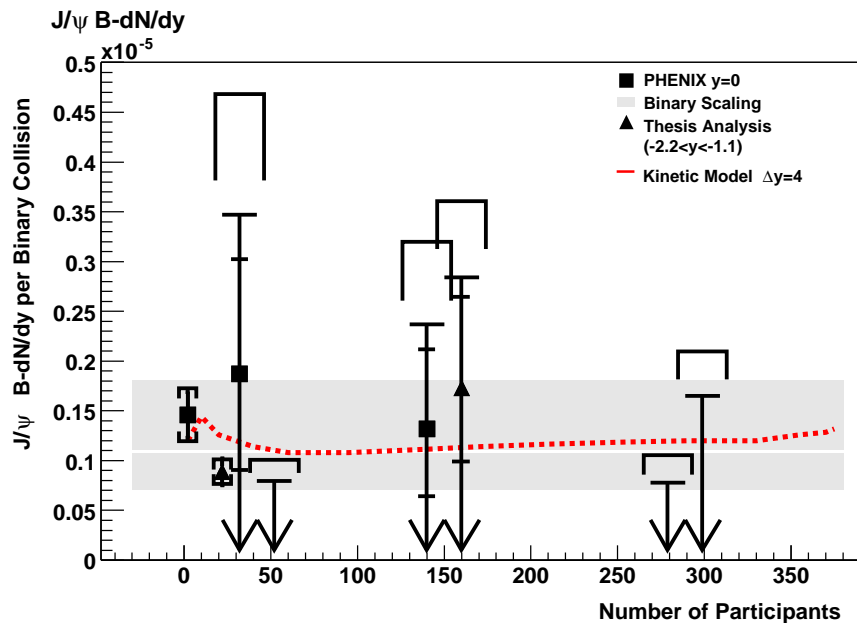
Figure 5.14: The PHENIX measured J/ψ invariant yield per binary collision for proton+proton and Au+Au reactions is shown at central rapidity, most likely values (squares). Also shown are forward rapidity measurements of PHENIX in proton+proton reactions and this thesis analysis in Au+Au reactions at forward rapidity, most likely values (triangles). Forward rapidity measurements are arbitrarily shifted right 20 units for rapidity. The arrows indicate the 90% confidence level upper limits for the Au+Au reactions bracketed above by the corresponding systematic uncertainty. The kinetic model prediction is shown for charm rapidity width of $\Delta y = 4$ [22].

The first analysis of the PHENIX Au+Au data at forward rapidity has been presented. While consistent will a null result, there is no dramatic deviation from the scenarios that were considered in the planning and design of the experiment. The Au+Au analysis is comparable to the published PHENIX measurement at central rapidity both in the limited statistics and the results. A variety of models have been examined that address scenarios including conventional suppression, quark gluon plasma suppression, and new production mechanisms within the quark gluon plasma. The implication of these models demonstrate the importance of measuring both the J/ψ and total charm production over the wide kinematic range offered by the combined measurements of the the PHENIX central arm and forward spectrometers. As the performance of the detector and of the RHIC machine continues to improve, the precision of future measurements will be able resolve the competing production and suppression processes of the J/ψ including the elusive quark gluon plasma.

Chapter 6

Conclusions

This work reports the results of the first J/ψ measurement in Au+Au reactions at $\sqrt{s_{NN}} =$ 200 GeV at forward rapidity. Results presented in this work are not able to discern among various model predictions for J/ψ production due to insufficient statistics; there is no conclusive indication of QGP formation. However, the consistency of this analysis with the similar measurement at central rapidity indicates that the planning and design of the PHENIX experiment is probing the correct range of possibilities.

A systematic study of hot, dense nuclear matter was recently completed at the SPS at CERN observing collision energies below that of RHIC. The measured production of J/ψ indicated a new suppression mechanism in the most energetic collisions. Controversial conclusions were drawn from this observation including the first creation of the predicted quark gluon plasma. However, alternative scenarios surveyed in this work that do not require color deconfinement are also able to explain the observations. The conclusive discernment of conventional and QGP

production and suppression measurements requires further study.

An overview of the theoretical landscape has been presented; the limited understanding of J/ψ production mechanisms and the subsequent interaction with the nuclear medium accommodate models employing a wide spectrum of physical scenarios. The heavy-ion collisions at the Relativistic Heavy Ion Collider at the Brookhaven National Lab provide the ideal system to extend the study of high-energy nuclear collisions.

One of the primary goals of the PHENIX experiment is to probe this matter in comprehensive study of charm and J/ψ production. The initial measurements of PHENIX and an analysis of the PHENIX muon arm data have been presented. The analysis included in this work has a vital role in the overall plan of this comprehensive study in present and future measurements. The present observations and their comparison to the current theoretical understanding are summarized.

1. PHENIX has measured total charm production in Au+Au reactions at mid-rapidity at $\sqrt{s_{NN}} = 130$ GeV and presented preliminary results at $\sqrt{s_{NN}} = 200$ GeV.

   (a) The PHENIX charm measurement is consistent with expectations from binary scaling of PYTHIA calculation.

   (b) This provides confirmation of previous estimates of order 10 $c\bar{c}$ pairs per central Au+Au collision.

   (c) No large p_T suppression was observed in the charm measurement as was in the PHENIX π^0 measurement relative to binary scaling.

2. PHENIX has measured J/ψ production in proton+proton reactions at $\sqrt{s_{NN}} = 200$ GeV at mid-rapidity (dieletron) and forward rapidity (dimuon).

   (a) The color singlet model drastically under predicts the measurement.

   (b) The color octet model describes the data reasonably well between for the applicable p_T range.

   (c) Both the color evaporation model and the color octet model well describe the total J/ψ production.

3. PHENIX has presented first results of J/ψ production in Au+Au collisions at RHIC for mid-rapidity (dieletron) at $\sqrt{s_{NN}} = 200$ GeV. The PHENIX measurement is extended in this thesis by a measurement at forward rapidity (dimuon). The discerning power of both measurements is limited by similar statistics, yet the measurements are compatible.

   (a) The PHENIX central rapidity measurement disfavors binary scaling while this cannot be ruled out by the forward rapidity measurement of this thesis.

   (b) The PHENIX measurement at central rapidity is consistent with: "normal" nuclear absorption, "normal" plus QGP absorption, and statistical production at hadronization. The measurement presented in this thesis at forward rapidity is also consistent with these scenarios since all scale less than the number of binary collisions.

   (c) The PHENIX central rapidity measurement disfavors dynamic coalescence which predicts enhancement above binary scaling. The dynamic coalescence prediction for a flat charm rapidity distribution of width 4 is relevant for both central and

forward rapidity. This calculation is only marginally disfavored by the PHENIX central measurement and cannot be excluded by the forward measurement of this thesis.

The strength of the PHENIX experiment is its ability to study the production of charm and J/ψ production in a wide kinematic range (rapidity) and in a variety of systems: proton+proton reactions, deuteron+Au reactions, and Au+Au reactions. At present the PHENIX J/ψ measurements and this thesis analysis cannot confirm the CERN observation of an "anomalous" suppression nor conclude observation of the production of a quark gluon plasm due to the statistical limitations of existing data.

Many performance issues of the PHENIX forward spectrometer challenging the commissioning run have been addressed during or after the collection of the data analyzed in this thesis.

- The temporary and partial shielding installed during Run II to reduce collision related background has been replaced with a permanent more comprehensive shielding solution.

- Shielding behind the MuID will be installed to address the beam related background that overwhelmed the MuID during the high luminosity Au+Au running.

- The inactive or inefficient detector channels in both the MuID and the MuTr have been recovered by resolving high-voltage issues and replacing readout electronics.

- Advancements in the performance of the RHIC machine were realized during the following Run III that will provide greater luminosity and less beam related background.

158

The maturing analysis of d-Au reactions already recorded at RHIC will provide important information on the effective J/ψ nucleon cross section and shadowing effects. The conclusive observation of the QGP in nucleus-nucleus reactions continues to be an exciting and promising pursuit. Future Au+Au runs at RHIC will provide the statistics for a precise measurement of J/ψ production as a function of several observables: collision centrality, transverse momentum, and beam energy. In this systematic study the complex and competing processes of J/ψ production and suppression will be unraveled.

Bibliography

Bibliography

[1] S. S. Adler *et al.* (PHENIX), "J/ψ production in Au-Au collisions at $\sqrt{s_{NN}} = 200$ GeV at the Relativistic Heavy Ion Collider" (2003), nucl-ex/0305030.

[2] M. C. Abreu *et al.* (NA50), Phys. Lett. **B477**, 28 (2000).

[3] J. J. Aubert *et al.*, Phys. Rev. Lett. **33**, 1404 (1974).

[4] J. E. Augustin *et al.*, Phys. Rev. Lett. **33**, 1406 (1974).

[5] A. Mosher, *The Strong interactions: Proceedings of the 9th SLAC Summer Institute on Particle Physics (SSI 81), Stanford, Calif., 27 Jul - 7 Aug, 1981*, sLAC-0245.

[6] E. L. Berger and D. L. Jones, Phys. Rev. **D23**, 1521 (1981).

[7] M. Kramer, Prog. Part. Nucl. Phys. **47**, 141 (2001), hep-ph/0106120.

[8] M. C. Abreu *et al.*, Phys. Lett. **B466**, 408 (1999).

[9] M. J. Leitch *et al.* (FNAL E866/NuSea), Phys. Rev. Lett. **84**, 3256 (2000), nucl-ex/9909007.

[10] H. Satz, Nucl. Phys. **A661**, 104 (1999), hep-ph/9908339.

[11] C.-Y. Wong, T. Barnes, E. S. Swanson, and H. W. Crater, Nucl. Phys. **A715**, 541 (2003), nucl-th/0209017.

[12] C.-Y. Wong, Phys. Rev. **C65**, 034902 (2002), nucl-th/0110004.

[13] L. Grandchamp and R. Rapp, Nucl. Phys. **A709**, 415 (2002), hep-ph/0205305.

[14] M. Allen *et al.* (PHENIX), Nucl. Instrum. Meth. **A499**, 549 (2003).

[15] H. D. Sato, *J/ψ Production in p+p Collisions at $\sqrt{s} = 200$ GeV*, Dissertation, Kyoto University (2002).

[16] S. S. Adler *et al.* (PHENIX), Nucl. Instrum. Meth. **A499**, 593 (2003).

[17] S. S. Adler *et al.* (PHENIX), "J/ψ Production from proton proton collisions at $\sqrt{s} = 200$ GeV" (2003), hep-ex/0307019.

[18] G. C. Nayak, M. X. Liu, and F. Cooper, Phys. Rev. **D68**, 034003 (2003), hep-ph/0302095.

[19] K. Adcox *et al.* (PHENIX), Phys. Rev. Lett. **88**, 192303 (2002), nucl-ex/0202002.

[20] B. Z. Kopeliovich and A. V. Tarasov, Nucl. Phys. **A710**, 180 (2002), hep-ph/0205151.

[21] H. Satz, "Parton percolation in nuclear collisions" (2002), hep-ph/0212046.

[22] R. L. Thews, "An assessment of J/ψ formation in the light of initial RHIC data" (2003), hep-ph/0305316.

[23] R. V. Gavai, Pramana **55**, 125 (2000), hep-ph/0003147.

[24] H. Satz, Rept. Prog. Phys. **63**, 1511 (2000), hep-ph/0007069.

[25] C. Gerschel and J. Hufner, Phys. Lett. **B207**, 253 (1988).

[26] P. A. Rapidis, in *SLAC Summer Inst.*, Stanford, CA (1992), pp. 469–477, invited talk given at 20th Annual SLAC Summer Institute on Particle Physics: The Third Family and the Physics of Flavor (School: Jul 13-24, Topical Conference: Jul 22-24, Symposium on Tau Physics: Jul 24) (SSI 92), Stanford, CA, 13-24 Jul 1992.

[27] A. D. Martin, R. G. Roberts, W. J. Stirling, and R. S. Thorne, Phys. Lett. **B443**, 301 (1998), hep-ph/9808371.

[28] H. Fritzsch, Phys. Lett. **B67**, 217 (1977).

[29] M. Gluck, J. F. Owens, and E. Reya, Phys. Rev. **D17**, 2324 (1978).

[30] R. Vogt, Heavy Ion Phys. **18**, 11 (2003), hep-ph/0205330.

[31] R. Gavai *et al.*, Int. J. Mod. Phys. **A10**, 3043 (1995), hep-ph/9502270.

[32] M. Beneke and I. Z. Rothstein, Phys. Rev. **D54**, 2005 (1996), hep-ph/9603400.

[33] W. E. Caswell and G. P. Lepage, Phys. Lett. **B167**, 437 (1986).

[34] G. T. Bodwin, E. Braaten, and G. P. Lepage, Phys. Rev. **D51**, 1125 (1995), hep-ph/9407339.

[35] C. Gerschel and J. Hufner, Z. Phys. **C56**, 171 (1992).

[36] R. L. Anderson *et al.*, Phys. Rev. Lett. **38**, 263 (1977).

[37] E. Iancu, A. Leonidov, and L. McLerran, *"The Colour Glass Condensate: An Introduction"* (2002), hep-ph/0202270.

[38] G. R. Farrar, H. Liu, L. L. Frankfurt, and M. I. Strikman, Phys. Rev. Lett. **61**, 686 (1988).

[39] B. Z. Kopeliovich, Nucl. Phys. **A698**, 547c (2002), hep-ph/0104032.

[40] B. Z. Kopeliovich and B. G. Zakharov, Phys. Rev. **D44**, 3466 (1991).

[41] T. Matsui and H. Satz, Phys. Lett. **B178**, 416 (1986).

[42] T. Hashimoto, O. Miyamura, K. Hirose, and T. Kanki, Phys. Rev. Lett. **57**, 2123 (1986).

[43] D. Kharzeev, L. D. McLerran, and H. Satz, Phys. Lett. **B356**, 349 (1995), hep-ph/9504338.

[44] S. Gavin, M. Gyulassy, and A. Jackson, Phys. Lett. **B207**, 257 (1988).

[45] R. Vogt, M. Prakash, P. Koch, and T. H. Hansson, Phys. Lett. **B207**, 263 (1988).

[46] T. Barnes and E. S. Swanson, Phys. Rev. **D46**, 131 (1992).

[47] Lin, Zi-wei and Ko, C. M., Nucl. Phys. **A715**, 533 (2003), nucl-th/0210014.

[48] N. Armesto, A. Capella, E. G. Ferreiro, A. Kaidalov, and D. Sousa, Nucl. Phys. **A698**, 583 (2002), nucl-th/0104004.

[49] N. Armesto and A. Capella, Phys. Lett. **B430**, 23 (1998), hep-ph/9705275.

[50] M. Gazdzicki and M. I. Gorenstein, Phys. Rev. Lett. **83**, 4009 (1999), hep-ph/9905515.

[51] P. Braun-Munzinger and J. Stachel, Nucl. Phys. **A690**, 119 (2001), nucl-th/0012064.

[52] R. L. Thews, M. Schroedter, and J. Rafelski, Phys. Rev. **C63**, 054905 (2001), hep-ph/0007323.

[53] S. Aronson, J. Bowers, J. Chiba, G. Danby, A. Drees, O. Fackler, A. Franz, J. Freidberg, W. Guryn, A. Harvey, *et al.*, Nucl. Instr. and Meth. (2002).

[54] R. L. Thews, in H. T. Elze, E. Ferreira, T. Kodama, J. Letessier, J. Rafelski, and R. L. Thews, eds., *an American Advanced Studies Institute on New States of Matter in Hadronic Interactions* (American Institute of Physics, Campos do Jordao, Brazil, 2002), vol. 631, hep-ph/0206179.

Vita

Robert Jason Newby was born on June 1, 1974 in McMinnville, Tennessee. He graduated from Warren County Senior High School, McMinnville, Tennessee, in May 1992. From August 1992 to May 1996, he attended King College, Bristol, Tennessee, to study mathematics and physics. During the summer of 1995 he was first introduced to experimental physics while working for Prof. Alvin Sanders in the Science Alliance Program at the University of Tennessee where he studied high-precision remote phosphor thermometry. He graduated with honors in 1996 with a Bachelor of Science degree majoring in physics and mathematics.

In August 1996, he worked as a systems programmer for Clinical Trial Management Services, Bristol, Tennessee designing statistical analysis software for data collected in clinical trials. In August 1997, he began his graduate studies in physics at the University of Tennessee as a teaching assistant in undergraduate physics and astronomy laboratories.

Mr. Newby pursued doctoral research in experimental high-energy nuclear physics on the PHENIX Experiment at Brookhaven National Laboratory, Upton, New York. Resident on Long Island for almost two years, he assisted in the commissioning of the PHENIX Muon Identifier detector and analyzed J/ψ production in proton+proton and Au+Au collisions at the Relativistic Heavy Ion Collider. In 2003, he received the University of Tennessee Fowler-Marion Outstanding Graduate Student Award for his achievements in the classroom and in research. His thesis adviser was Prof. Soren Sorensen. He received his doctoral degree in December 2003.

In October 2003, he will begin work in the Physics and Advanced Technologies directorate at Lawrence Livermore National Laboratory as a postdoctoral research associate.